Photonic Crystal Optical Tweezers for Live Biological Samples

Peifeng Jing

A dissertation

submitted in partial fulfillment of the

requirements for the degree of

Doctor of Philosophy

University of Washington

2017

Reading Committee:

Lih Y. Lin, Chair

Arka Majumdar

Benjamin S. Freedman

Program Authorized to Offer Degree:

Electrical Engineering

University of Washington

Abstract

Photonic Crystal Optical Tweezers for Live Biological Samples

Peifeng Jing

Chair of the Supervisory Committee
Professor Lih Y. Lin
Department of Electrical Engineering

Optical Tweezers is a valuable and versatile tool in the non-invasive manipulation of micro- and nano-sized particles for biology studies and nanotechnologies. In this dissertation, we propose and demonstrate a two-dimensional photonic crystal enhanced optical tweezers for particles and biological cells with higher trapping efficiency and less photodamage or heat generation. The capabilities of this enhanced optical tweezers include trapping, transporting and patterning latex beads and cells. The trapping efficiency is significantly improved based on the higher gradient of laser intensity distribution. This technology relaxes the requirement on input optical power without additional heat generation, which extends the viability of living cells in the trap. Moreover, we developed a flexible platform using parylene-C integrated with photonic crystal enhanced optical tweezers. This system is utilized for colonizing patterned cells with optimized oxygen plasma treated parylene-C film, as well as measuring the cellular repulsive force between a pair of single cells.

TABLE OF CONTENTS

TABLE OF FIGURES

ACKNOWLEDGEMENTS

I would like to first express my sincere gratitude to my academic advisor, Prof. Lih Lin. The gratitude is not only for her insightful comments and professional guidance on my projects during the past five years but also for her encouragement that gave me the strength to hang on when I meet challenges on the projects. She trains me in every aspect of being a professional scholar and shares her experience to achieve success in academia. This learning process is not only from her words and verbal instructions but her actions and deeds as well. When I look back my Ph.D. time, I attribute my improvement mainly to the guidance and influence of my advisor.

I would like to thank Prof. Suzie Pun and Prof. Benjamin Freedman for the collaboration of biological cells and their advice on the research. My thanks also go to all the former and current members of the Photonics group, Matthew Strathman, Jingda Wu, Erin Sanehira, Ethan Keeler, Chen Zhou, Yu Jin, Yunbo Liu, Conner Ballew, and Yannan Liu for providing a stimulating and fun environment. I am also indebted to Gary W. Liu, Nelly M. Cruz, Ramila E. Gulieva, Angela J. Churchill, Raghava Reddy, and Kosuke Winston for their work in the experiments on biological cells. I want to thank my friends Yaoyu Yang, Xiaobao Xu, Erjin Zheng, Beau Richardson, Monica Espoi for their generous help in experiments. Finally, I would like to thank my parents for all their encouragement and support over the years.

The work covered in this dissertation is supported by the National Science Foundation (NSF) IDBR program and Clean Energy Institute (CEI) at various times.

CHAPTER 1 INTRODUCTION

The photonic crystal (PhC) [1] has become an important structure for manipulating photons and has demonstrated great success and potential for various applications. Much effort has been made to PhC geometry design and fabrication to optimize the photonic band structure for different utilizations, such as light-trapping cavities and resonators [2-4], optical fibers [5] and waveguides [6]. Most of these applications use the photonic bandgap property of PhC and light propagates along the direction of the periodic structures. More recently, researchers have explored normal incident light to the surface of the PhC structure. Theoretical study and numerical simulations have shown that the emission pattern from the PhC surface can be designed [7], and two-dimensional optical feedback has been utilized to engineer PhC structures for compact semiconductor lasers that can generate different beam patterns [8, 9].

Optical tweezers are another significant development in photonics. Since its inception, optical tweezers have proven to be a versatile and powerful tool for biological applications and nanotechnology due to its capability of trapping and positioning micro- and nano-particles with high precision, flexibility and non-invasiveness [10, 11]. Recently, the ability to manipulate photons and optical field through PhC has found its application in optical tweezers. The concentrated optical near-field along a PhC waveguide surface has been shown to be able to trap small particles efficiently [12, 13]. Utilizing the enhanced diffraction pattern from the surface of a one-dimensional photonic crystal (1D PhC) nanostructure, it has also been demonstrated trapping and aligning particles with a broad range of size ranging from 10 μm down to 190 nm with lower optical intensity than

conventional optical tweezers [14]. Trapping of ovarian cancer cell nuclei was achieved with 16 $\mu W/\mu m^2$ intensity, and Listeria cells were trapped and aligned with an optical intensity of 40 $\mu W/\mu m^2$. Trapping particles in various patterns are desirable for the functionality and performance of optical tweezers. The typical approach, the holographic optical tweezers, is using a spatial light modulator to generate the laser patterns [15, 16]. While this method can achieve versatile optical trap patterns, exquisite optical setups and high optical intensities are often required. The latter mainly limits its application in biological studies.

In my Ph.D. research, I proposed to utilize two-dimensional photonic crystal (2D PhC) enhanced optical tweezers to improve the trapping capability of optical tweezers and reduce the photo-damage on biological samples. The PhC nanostructures increase the gradient trapping forces by generating localized light fields above the surface of the structures. The photo-damage can then be reduced by decreasing the laser power while keeping the same trapping capability. Moreover, with less photo-damage on biological samples, we developed a versatile platform integrated with enhanced optical tweezers for manipulating living cells for various aims, such as patterning and culturing cells as well as measuring interactive forces between single cells.

CHAPTER 2 THEORETICAL BACKGROUND

2.1 Force of Optical Tweezers

In the theory of trapping dielectric particle whose diameter is significantly smaller than the wavelength of light, the particle can be treated as a dielectric dipole; Rayleigh scattering and Lorentz force is applied in an inhomogeneous electromagnetic field.

The small micro-spherical particle with refractive index n_a is merged in a medium with the refractive index n_b, and the polarizability of the particle is described as

$$\alpha = 4\pi\varepsilon_0 n_b^2 \left(\frac{m^2-1}{m^2+2}\right) R^3 \tag{2.1}$$

where $m = \frac{n_a}{n_b}$ and R is the radius of the sphere. The particle can be considered as a dielectric dipole, and the Lorentz force on the particle is described as

$$\vec{\boldsymbol{F}} = q\left(\vec{\boldsymbol{E}} + \vec{\boldsymbol{v}}\times\vec{\boldsymbol{B}}\right) = (\vec{\boldsymbol{P}}\cdot\boldsymbol{\nabla})\vec{\boldsymbol{E}} + \frac{\partial\vec{\boldsymbol{P}}}{\partial t}\times\vec{\boldsymbol{B}} \tag{2.2}$$

where $\vec{\boldsymbol{P}} = \vec{\boldsymbol{D}} - \varepsilon_0\vec{\boldsymbol{E}}$ is the induced dielectric polarization density.

By substituting $\vec{\boldsymbol{P}} = \alpha\vec{\boldsymbol{E}}$ and Maxwell's Equations to Eq. (2.2), we can get the time-average Lorentz force on the particle as Eq. (2.3).

$$< \vec{\boldsymbol{F}} >= \frac{1}{2}\alpha\nabla< |\vec{\boldsymbol{E}}|^2 > \tag{2.3}$$

The light beam used in optical tweezers is usually a single mode laser, whose transverse electric field distribution is the Gaussian function described by Eq. (2.4) in the cylindrical coordinates.

$$\vec{\boldsymbol{E}}(r,z) = \vec{\boldsymbol{E}}_0 \frac{w_0}{w(z)} \exp\left(\frac{-r^2}{w(z)^2}\right) \exp\left(-i\left(kz + k\frac{r^2}{2R(z)} - \varphi(z)\right)\right) \tag{2.4}$$

where r is the radial distance from the center axis of the beam, z is the axial distance from the beam's focus, $k = \frac{2\pi}{\lambda}$ is the wave number, $\overrightarrow{\boldsymbol{E}_0} = \vec{\boldsymbol{E}}(0,0)$ is the electric field at the origin, $w(z) = w_0[1 + (\frac{z}{z_R})^2]^{-1/2}$ is the radius at which the field amplitude falls to 1/e of their axial values, $z_R = \frac{\pi w_0^2}{\lambda}$ is the depth of focus, and $w_0 = w(z = 0)$ is the waist size. By substituting Eq. (2.4) into (2.3), the further expressions for the gradient force in Gaussian beam can be obtained as follows

$$\overrightarrow{\boldsymbol{F_r}} = -\hat{\boldsymbol{e}}_r \frac{1}{2}\alpha\left|\vec{\boldsymbol{E}}_0\right|^2 \left(\frac{w_0}{w(z)}\right)^2 \exp\left(-\frac{2r^2}{w^2(z)}\right)\frac{4r}{w^2(z)} \tag{2.5}$$

$$\overrightarrow{\boldsymbol{F_\varphi}} = \boldsymbol{0} \tag{2.6}$$

$$\overrightarrow{\boldsymbol{F_z}} = -\hat{\boldsymbol{e}}_z \frac{1}{2}\alpha\left|\vec{\boldsymbol{E}}_0\right|^2 \left(\frac{w_0}{w(z)}\right)^2 \exp\left(-\frac{2r^2}{w^2(z)}\right)\left[1 + (\frac{z}{z_R})^2\right]^{-2}\frac{2z}{z_R^2}\left(1 - \frac{2r}{w^2(z)}\right) \tag{2.7}$$

If the radial displacement is much less than the beam waist $|\vec{\boldsymbol{r}}| \ll w_0$, the transverse gradient force is approximately proportional to the radial displacement.

The dipole oscillates in an electromagnetic field and radiates secondary or scattering wave in all directions. Therefore, the scattering force including Mie and Rayleigh scattering is also applied to the particle as follow [17].

$$\vec{F}_{scat}(\vec{r}) = \frac{C_{pr} \cdot <\vec{S}(\vec{r},t)>}{\frac{c}{n_b}} \tag{2.8}$$

where, the C_{pr} is the scattering cross section and $<\vec{S}(\vec{r},t)>$ is the time-averaged Poynting vector. For Rayleigh scattering, it is described as [18]

$$\vec{F}_{scat}(\vec{r}) = \hat{z}\frac{n_b}{c}\frac{8}{3}\pi(ka)^4 a^3 \left(\frac{m^2-1}{m^2+2}\right)^2 I(\vec{r}) \tag{2.9}$$

In cases of trapping dielectric particles whose sizes are comparable with the wavelength of the laser (D ~ λ), generalized Lorenz-Mie theory is used to calculate trapping force and scattering force from the electromagnetic field. The general law of forces in electromagnetic fields is based on the conservation law for linear momentum. The Lorentz force is described as

$$\vec{\boldsymbol{F}} = q\left(\vec{\boldsymbol{E}} + \vec{\boldsymbol{v}}\times\vec{\boldsymbol{B}}\right) = \iiint (\rho\vec{\boldsymbol{E}} + \vec{\boldsymbol{j}}\times\vec{\boldsymbol{B}})dV \tag{2.10}$$

This equation for force density $\vec{\boldsymbol{f}}$ can be rewritten by Maxwell stress tensor $\boldsymbol{T}$ and Poynting vector $\vec{\boldsymbol{S}}$

$$\vec{\boldsymbol{f}} = \rho\vec{\boldsymbol{E}} + \vec{\boldsymbol{j}}\times\vec{\boldsymbol{B}} = \nabla\cdot\boldsymbol{T} - \varepsilon_0\mu_0\frac{\partial\vec{\boldsymbol{S}}}{\partial t} \tag{2.11}$$

where

$$T_{ij} = \varepsilon_r\varepsilon_0\vec{E}_i\vec{E}_j + \mu_r\mu_0\vec{H}_i\vec{H}_j - \frac{1}{2}\delta_{ij}\left(\vec{\boldsymbol{E}}^2 + \vec{\boldsymbol{B}}^2\right) \tag{2.12}$$

$$\vec{\boldsymbol{S}} = \vec{\boldsymbol{E}}\times\vec{\boldsymbol{H}} \tag{2.13}$$

The time-averaged force can then be described in a closed surface integral as the following.

$$< \vec{\boldsymbol{F}} >= \iiint < \vec{\boldsymbol{f}} > dV = \oiint \boldsymbol{T} \cdot d\vec{\boldsymbol{S}} \tag{2.14}$$

2.2 Optical Trap Stiffness

2.2.1 Definition of Stiffness

For small displacement with a Gaussian laser beam $|\vec{\boldsymbol{r}}| \ll w_0$, the exponential term approaches to one in the Equation (2.5), and the gradient force turns out to be proportional to the displacement of the particle.

$$F_{grad} = -k \cdot r \tag{2.15}$$

Where k is called the stiffness of the trap and its magnitude is usually piconewtons per micrometer with milliwatts of laser power. Once the stiffness is given, the trapping force applied on the particle can be determined by accurately measuring the position of the particle. Many technologies are developed to detect the situation of particles in real time, including video-based position detection, back-focal plane (BFP) interferometry with quadrant photodiode (QPD) and laser-based position detection with a QPD. [19-22]

2.2.2 Stoke's Law

The most commonly utilized method to measure the trap stiffness is dragging, in which the particle is pulled by the laser with increasing speed until it escapes from the trap at a velocity of v. Therefore, the maximum trapping force could be calibrated by the frictional

viscosity force, acting between the fluid and the particle, and it can be calculated by Stoke's law in Eq. (2.16) with the assumption of laminar flow.

$$F = 6\pi\eta R v \tag{2.16}$$

where η is the dynamic viscosity of the liquid, R is the radius of the spherical object, and v is the speed.

The laminar flow can be identified by Reynolds number that is an important dimensional quality in fluid mechanics. Laminar flow occurs at low Reynolds numbers ($Re \leq 0.1$) which can be calculated by Eq. (2.17).

$$Re = \frac{\rho R v}{\eta} \tag{2.17}$$

where ρ is the density of the fluid. In the experiments with biological cells or small particles whose diameters are less than $20\mu m$, Stoke's law applies if the dragging velocity is no more than $5mm/s$.

2.2.3 Faxen's Law

When trapped spherical particles are close the surface of the chamber and under a low Reynolds number conditions in the fluids, the interactions of the sphere with the boundary layer of water near a surface lead to an increase in the viscosity and Faxen's law is the correction to Stoke's law in such conditions. The formula of hydrodynamic force will become

$$F = \frac{6\pi\eta R v}{1 - \frac{9}{16}\left(\frac{R}{h}\right) + \frac{1}{8}\left(\frac{R}{h}\right)^3 - \frac{45}{256}\left(\frac{R}{h}\right)^4 - \frac{1}{16}\left(\frac{R}{h}\right)^5} \tag{2.18}$$

where η is the dynamic viscosity of the liquid, R is the radius of the spherical object, v is the speed, and h is the distance from the center of the sphere to the surface.

If the sphere touches the surface $h = R$, the forces can be simply calculated by

$$F = 3.08 \times 6\pi\eta R v = 18.48\pi\eta R v \tag{2.19}$$

2.2.4 Equilibrium Theorem

The force can also be measured by the spectrum of the Brownian motion of the trapped particle. The particle in the medium in thermal equilibrium moves randomly within the optical trap known as the Brownian movement. Because of the optical gradient force described in Section 2.1, the particle is confined in the trap region. In thermal equilibrium, the probability density of the particle in the optical trap can be described by Boltzmann statistics,

$$\rho(\vec{\boldsymbol{r}}, \varphi) = C \cdot exp\left(-\frac{U(\vec{\boldsymbol{r}}, \varphi)}{k_B T}\right) \tag{2.20}$$

where k_B is Boltzmann constant, T is the absolute temperature, $U(\vec{\boldsymbol{r}}, \varphi)$ is the potential energy and C is a normalization constant.

The trapping gradient force is described by Eq. (2.5) if a Gaussian beam is used to trap the particle. The force is approximately proportional to the displacement $\vec{\boldsymbol{r}}$ when $|\vec{\boldsymbol{r}}| \ll w_0$, so the potential energy can be considered as a harmonic potential in Eq. (2.18) and the probability density is a Gaussian function. [23]

$$\rho(x, \varphi) = C \cdot exp\left(-\frac{k_x x^2}{2k_B T}\right) = C \cdot exp\left(-\frac{x^2}{2\sigma_x^2}\right) \tag{2.21}$$

Then the stiffness of the trapping force k_x can be calculated by Eq. (2.19) if we know the temperature and the variance of sampled positions.

$$k_x = \frac{k_B T}{\sigma_x^2} \tag{2.22}$$

The stiffness of the trap represents the capability of trapping particles. The stiffness is inversely proportional to the statistical variance of the Gaussian function of the trapping source. Therefore, a more spatially confined electromagnetic wave is more efficient to trap particles.

2.3 Kirchhoff Integral Theorem

The enhancement of the proposed PhC optical tweezers is caused by light scattering and diffraction after being reflected from the PhC. The main contribution to the increased trapping force is primarily from the finite size of the hole. As explained later in Chapter 3, the scattering light computed by Kirchhoff Integral Theorem provides a good estimation to the laser intensity distribution simulated by Finite-Difference Time-Domain method.

The Kirchhoff integral theorem describes the solution of the homogeneous wave equation at an arbitrary point **P** in the field. The solution is integral at all points on an arbitrary closed surface surrounding this point derived from the Green's theorem [24]. Suppose $U(x, y, z)$ is the space-dependent part of a monochromatic scalar wave which follows the Helmholtz equation

$$(\nabla^2 + \boldsymbol{k}^2) \cdot U(x, y, z) = 0 \tag{2.23}$$

If there are two enclosed surfaces S and S' with the amplitude $U(x,y,z)$ and $U'(x,y,z)$ around the point **P**. From Helmholtz equation in Eq. (2.23) and Greens' theorem in Eq. (2.24), we can get the following formula.

$$\oiint_S \left(U\frac{\partial U'}{\partial n} - U'\frac{\partial U}{\partial n}\right)dS = -\iiint_V (U\nabla^2 U' - U'\nabla^2 U)dV = 0 \tag{2.24}$$

If $U' = \frac{e^{iks}}{s}$ and let $s \to 0$ to denote the point **P**, we can get the Kirchhoff's formula

$$U(P) = \frac{1}{4\pi}\oiint_S \left(U\frac{\partial}{\partial n}\left(\frac{e^{iks}}{s}\right) - \frac{e^{iks}}{s}\frac{\partial U}{\partial n}\right)dS \tag{2.25}$$

In the single hole diffraction, the Kirchhoff's formula can be utilized to get the analytical solution

$$U(P) = -\frac{iA}{2\lambda}\iint_S \frac{e^{ik(r+s)}}{rs}[\cos(n,r) - \cos(n,s)]dS \tag{2.26}$$

where n is the normal vector of the hole, r is the vector from the light source to an arbitrary point **Q** on the hole, and s is the vector from the point **Q** to the point **P** where the electromagnetic field will be calculated [24].

For an extended source with the input complex amplitude as $U_0(r) = a(r)e^{-ikr}$ and we have $\frac{\partial U_0}{\partial n} = -ika(r)e^{-ikr}$. Therefore, the complex amplitude at an arbitrary point **P** can be described as

$$U(P) = -\frac{i}{2\lambda}\iint_S a(r)\frac{e^{ik(r+s)}}{s}[\cos(n,r) - \cos(n,s)]dS \tag{2.27}$$

2.4 Double Layer Theory and Zeta Potential

2.4.1 Double Layer Theory

When an object is exposed to a fluid, the structure of the surface will generate two parallel layers of charges which are called double layer. In Gouy-Chapman model, the first layer consists of the ions firmly absorbed on the surface due to chemical interactions, known as surface charge, while the ions in the second layer are diffusing around the surface and the electrical potential decreases exponentially away from the surface.

The electrical potential can be described by Poisson equation and Boltzmann equation.

$$\begin{cases} \nabla^2\psi = -\dfrac{\rho_e}{\varepsilon_r\varepsilon_0} \\ c_\pm = c_0 e^{\mp\frac{e\psi}{k_B T}} \end{cases} \tag{2.28}$$

where, ψ is the electrical potential, ρ_e is the electric charge density, ε_r is the relative permittivity of the solvent, ε_0 is the permittivity of free space, c_0 is the ion concentration on the surface, k_B is Boltzmann constant, and T is the temperature. The ion concentration is expressed by c_+ when the surface charge is negative, and it is written in c_- if the surface is positively charged.

Therefore, the electric charge density can be described as

$$\rho_e = c_0 e \cdot \left[e^{-\frac{e\psi}{k_B T}} - e^{\frac{e\psi}{k_B T}} \right] \tag{2.29}$$

and the Poisson-Boltzmann equation can be rewritten as

$$\nabla^2\psi = \frac{c_0 e}{\varepsilon_r \varepsilon_0}\left[e^{\frac{e\psi}{k_B T}} - e^{-\frac{e\psi}{k_B T}}\right] \tag{2.30}$$

For spherical particles, the Poisson-Boltzmann equation is the following formula in the spherical coordination.

$$\frac{\partial^2\psi}{\partial r^2} + \frac{2}{r}\frac{\partial\psi}{\partial r} = \frac{c_0 e}{\varepsilon_r \varepsilon_0}\left[e^{\frac{e\psi}{k_B T}} - e^{-\frac{e\psi}{k_B T}}\right] \tag{2.31}$$

When the potential is low $e\psi \ll k_B T$, there is the approximation that $sinh\left(\frac{e\psi}{k_B T}\right) \approx \frac{e\psi}{k_B T}$, and the solution of the potential is the following formula [25]

$$\psi_{s,DH}(x) = \psi_0\left(\frac{R}{R+x}\right)e^{-\kappa x} \tag{2.32}$$

where s refers to the sphere, DH refers to the solution derived by Debye and Hückel, R is the radius of the sphere, and $\kappa = \sqrt{\frac{e^2}{\varepsilon_r \varepsilon_0 k_B T}\sum c_i^0 Z_i^2}$ where c_i^0 is the environmental concentration of i-th ion and Z_i^2 is the valency of the i-th ion. The low potential condition implies $\psi \leq 25mV$ at room temperature. [26]

2.4.2 Zeta Potential and Surface Charge Density

Zeta potential, or electrokinetic potential, is the electric potential at the plane which locates between the surface charge and the slipping plane. The slipping plane could move under the influence of tangential stress, and ions beyond this plane can be separated from the surface to the fluid. Therefore, zeta potential is widely used for estimating the degree of the double layer charges. The charge density can be obtained from zeta potential using Grahame equation [26]

$$\sigma = \sqrt{8c_0\epsilon\epsilon_0 k_B T}\sinh\left(\frac{e\psi_0}{2k_B T}\right) \tag{2.33}$$

For low potentials, there is the approximation $\sinh\left(\frac{e\psi_0}{2k_B T}\right) \approx \frac{e\psi_0}{2k_B T}$, and the charge density can be calculated by the following equation

$$\sigma = \frac{\epsilon\epsilon_0\psi_0}{\lambda_D} \tag{2.34}$$

where $\lambda_D = \kappa^{-1} = \sqrt{\frac{\epsilon\epsilon_0 k_B T}{e^2 \sum c_i^0 Z_i^2}}$, known as Debye length. Since it is reciprocal of the exponential factor κ, the Debye length represents how far the electrostatic effects persist in solution.

2.4.3 Double Layer Forces

The immersed particles are charged with a double layer across the fluids. The first layer corresponds to the surface charge, while the second layer, known as the diffuse layer, consists of the opposite charges and loosely adsorbed near the first layer. The electric potential and the ion distribution are similar for identical objects. Therefore, when two identical spheres are close together, the electric potential and the ion distribution within the gap between the sphere generates a repulsive force on both spheres.

The electric potential of each sphere decreases exponentially, and the Debye length λ_D is the decay rate constant, which is usually one of a few tenths of nanometers [27]. Debye-Hückel and Poisson-Boltzmann models describe the interactions between immersed objects in the liquids. The Derjaguin approximation is commonly used to treat spherical objects and estimate forces between colloidal particles if their size is substantially larger

than Debye length. In experiments, optical tweezers have been utilized to directly measure and confirm the exponential decay of the forces [28, 29]. The Yukawa or screened Coulomb potential can be derived from Debye-Hückel approximation

$$U = \frac{Q^2}{4\pi\epsilon\epsilon_0}\left(\frac{e^{\kappa a}}{1+\kappa a}\right)^2 \frac{e^{-\kappa r}}{r} \tag{2.35}$$

where r is the center-to-center distance, Q is the particles charge, and a is the radius of particles. The Q is valid with a large gap between the particles, and it can be considered as the effective charge for highly charged particles. The interacting force is the gradient of the screened potential as shown in Eq. (2.36).

$$F = -\frac{\partial U}{\partial r} = \frac{Q^2}{4\pi\epsilon\epsilon_0}\frac{(1+\kappa r)}{(1+\kappa a)^2}\frac{e^{-\kappa(r-2a)}}{r^2} \tag{2.36}$$

2.5 Some Prior Work

2.5.1 Optical Trapping

Optical tweezers have become a non-invasive and versatile tool in biological study and micro- and nano-scale particle manipulations [18, 30]. The optical tweezers typically use a Gaussian beam laser, which provides an inhomogeneous electromagnetic field that generates Lorentz force and scattering force as mentioned in Section 2.1. The Lorentz force is also known as the gradient force that traps the particle at the center of the Gaussian beam. The conservation of linear momentum is another way to explain and understand the origin of gradient force [16, 31]. As shown in Fig. 2.1, a parallel beam of light with a gradient in intensity incidents on a spherical particle. The refraction trace of

two representative rays is presented in the figure and their linear momentum change after refraction. Therefore, the resultant of all rays pull the sphere towards to region with higher intensity, which is the focus of the Gaussian beam laser.

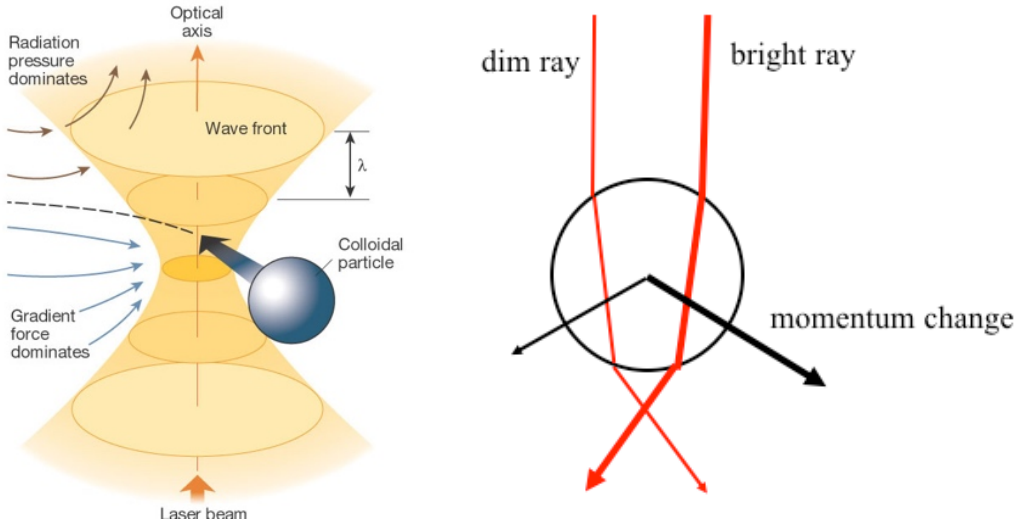

Figure 2.1 Origin of the gradient force and the conservation of linear momentum with Gaussian beam [16]

The typical spatial resolution of optical tweezers is 0.1-2nm, probe size is 0.25-5 μm and force range is 0.1-100 pN [22], which makes optical tweezers very appropriate for the control of micro- and nano-scale particles and molecules. Because of its non-invasiveness, versatility, and high precision, optical tweezers have been used to manipulate atoms [18], large molecules, and small dielectric spheres. In the biological study, optical tweezers are used to the measure the force and displacement resulting from the interactions between live cells [32, 33], DNA [34-36] and proteins [37-39].

However, the optically originated force limits its application in the biological study and nano particle (NP) manipulations due to the relatively small optical force and severe photodamage induced by the intense laser radiation [10, 40]. Therefore, many technologies have emerged to expand the capabilities of optical tweezers by increasing

the trapping efficiency and stiffness, as well as reducing the damage on live cells and biological molecules.

The versatility of optical tweezers can be improved by a spatial light modulator (SLM). The SLM adjusts phase distribution and the wave front of the laser beam with liquid crystals and dynamically generates reconfigurable holographical traps in three dimensions with computer programs. The typical optical setup of the holographic optical tweezers is shown in Fig. 2.2a, reported by Grier. 2003 [16, 41]. The SLM optical tweezers can generate large arrays of optical traps as shown in Fig. 2.2b, and it is also able to adjust the TM_{00} laser to a vortex in Fig. 2.2c. This capability improves the versatility of conventional optical tweezers and allows the optical tweezers to control multiple objects simultaneously.

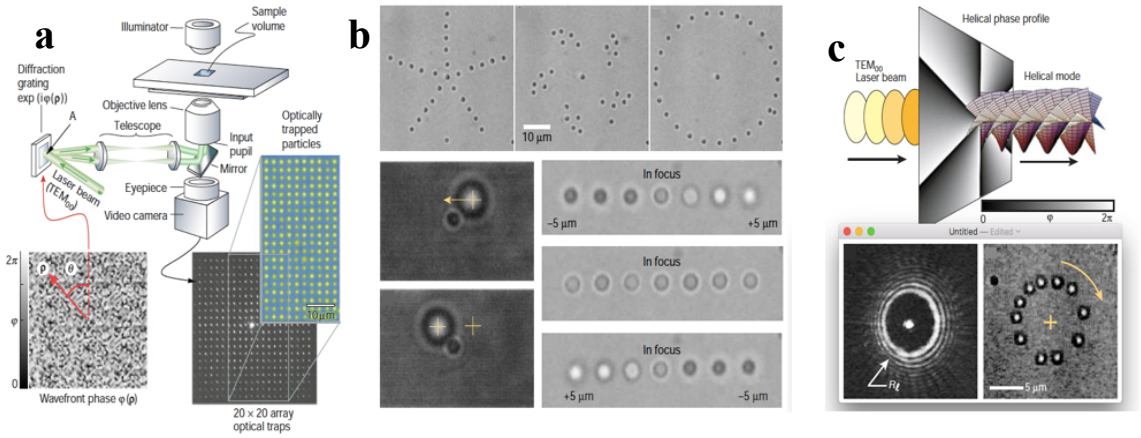

Figure 2.2 holographic optical tweezers [16] (a) optical setup (b) patterned trapping in three-dimension (c) trapping with helical modes

The plasmonics enhanced optical tweezers are developed to provide higher trapping efficiency with localized surface plasmon resonance by nanostructures [42, 43]. Besides, the plasmonic optical tweezers become more versatile by integrating with heat generation

and fluid flow [44-48]. Therefore, the manipulating capability of plasmonic tweezers can be expanded to assemble, pattern, and rotate trapped nanoparticles. Example works of plasmonic optical tweezers from Quidan et al. [42], Steinvurzel et al. [44] and Miao et al. [45, 47, 48] is shown in Fig. 2.3.

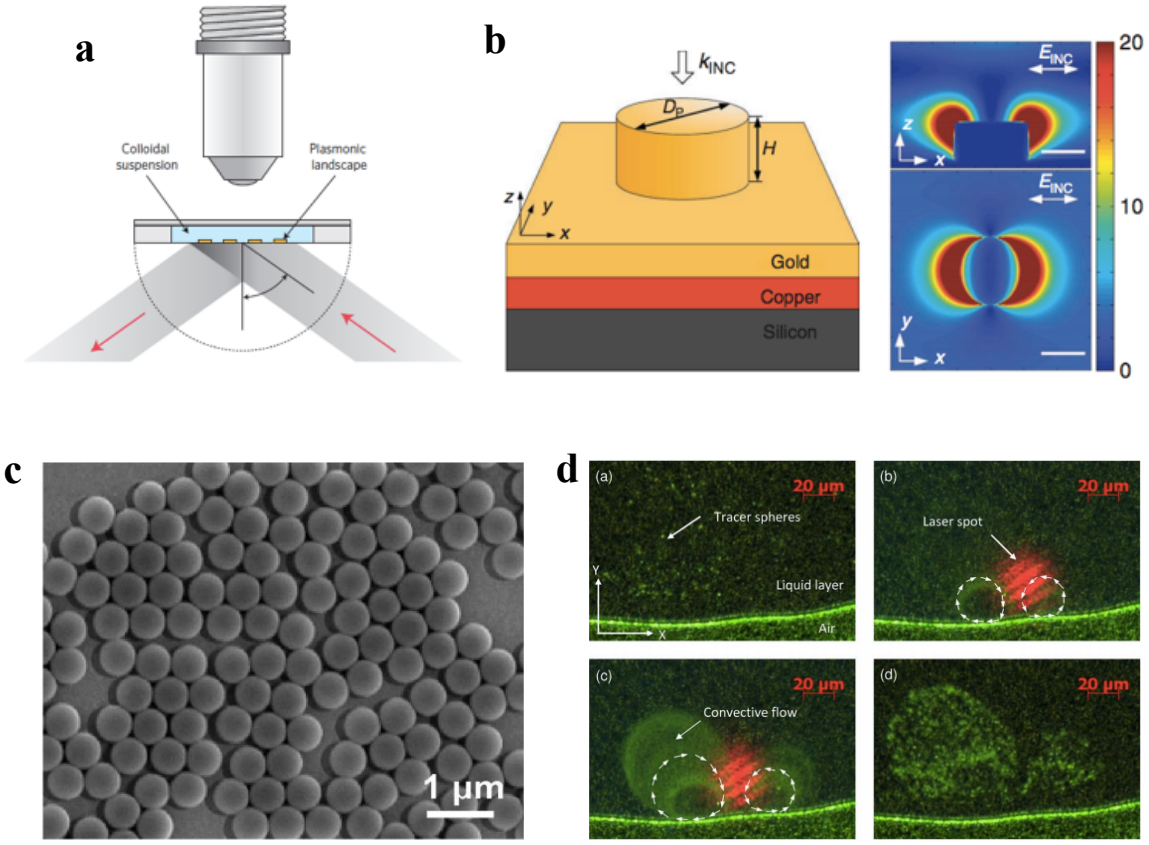

Figure 2.3 (a) optical setup for plasmonic optical tweezers [42] (b) nanostructure and its electric field simulation [44] (c) scanning electron micrograph of random gold nanoparticle array [49] (d) microfluidic convection driven by localized plasmon and visualized the dyed polystyrene tracer [48]

Significant limitations and drawbacks accompany the localized surface plasmon and high efficiency of plasmonic optical tweezers. First, the heat originated from surface plasmon resonance must be carefully considered during the use. Therefore, the nanostructure in plasmonic tweezers must be designed to corporate with the thermal effects on fluid flow.

Secondly, the location of plasmonic enhancement is predetermined by the design and fabrication of the substrate, which loses the versatility and the freedom of movement of conventional optical tweezers. Moreover, the hotspot of the plasmonic enhancement not only improves the trapping efficiency but also increase thermal damage to living cells, which limits its application in biological study.

Compared to plasmonics optical tweezers, PhC resonance is a method that localizes light intensity and increases the trapping efficiency for nanoparticles without generating extra heat. Silicon waveguide with PhC resonator is proposed to trap particles in the near-field of the cavity by the evanescent wave [12, 13]. Fig. 2.4a shows the work from Erickson, D. et al. [12] using PhC waveguide for light trapping. Evanescent wave above 2D PhC, also known as photonic-crystal slab, is also utilized to trap and assemble polystyrene beads. In Povinelli, M. L. et al. work [50], near-infrared laser incident on the two-dimensional slab vertically. The 2D PhC trap photons onto the plate which assembles nanoparticles in the ambient environment [50]. Fig. 2.4b is the schematic diagram of the enhanced optical trapping on 2D PhC. Wilson, B, et al. further demonstrated efficient trapping and alignment of particles and cells utilizing 1D periodic nanostructures and polarized laser [14]. The schematic graph and the numerical simulation of enhanced 1D PhC trapping are shown in Fig. 2.4c.

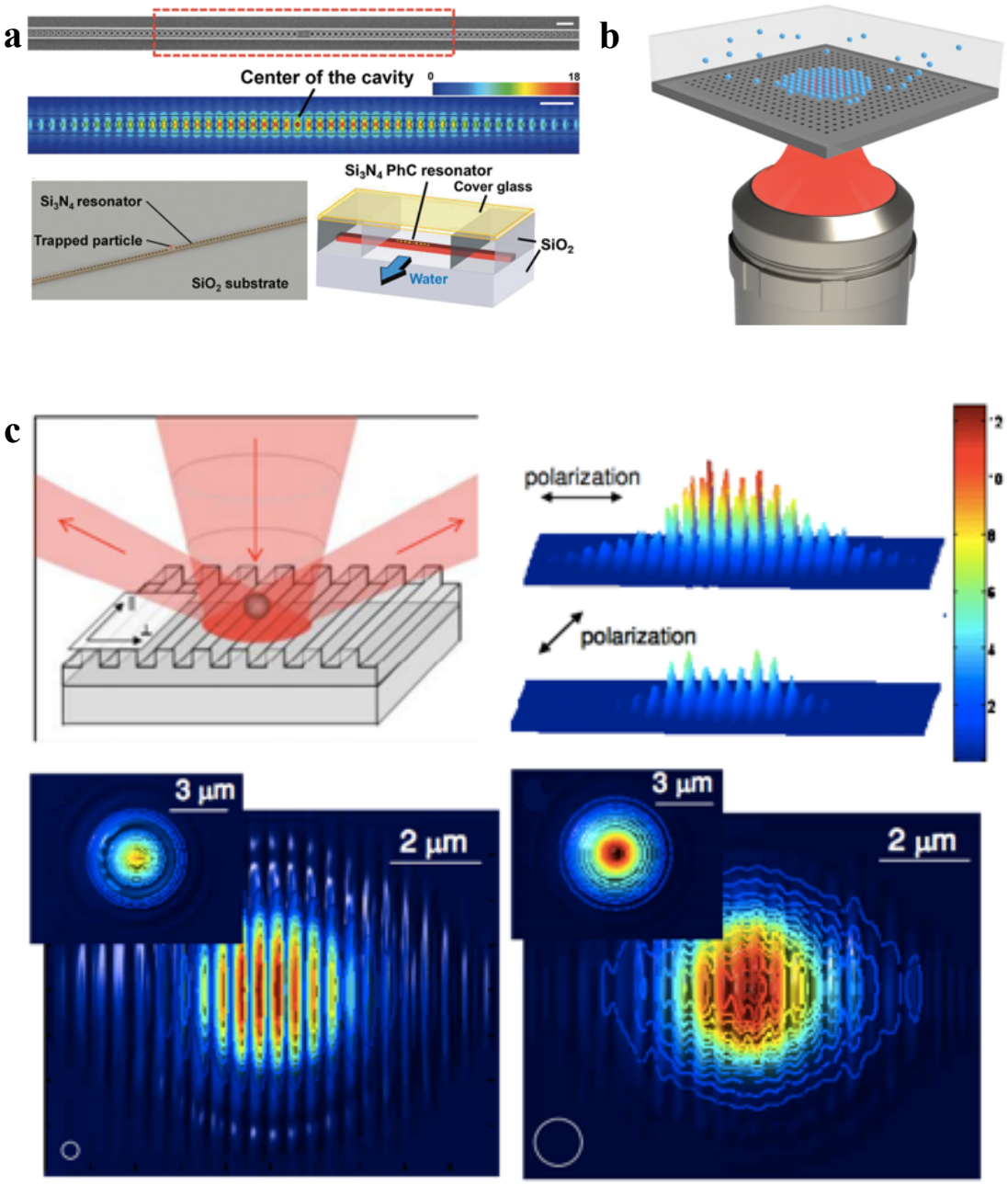

Figure 2.4 (a) PhC waveguide [12] (b) photonic-crystal slab for optical trapping [50] (c) enhanced optical trapping in the near field with 1-D periodic nanostructures and the FDTD simulation [14]

The trapping forces mentioned above is improved on the order of 10-20 times that the gradient force of conventional optical tweezers. The higher trapping efficiency can

significantly reduce the photo-damage. Thus, these methods will help to trap live cells over long periods [51].

To reduce trapping intensity and massively operate trapped particles, optoelectronic tweezers is developed by Wu, M. C. et al. [52] for trapping in large-scale with little photo-damage. As shown in Fig. 2.5a, it uses the light-induced inhomogeneous electric field to provide dielectrophoretic (DEP) force, which reduces trapping intensity and dynamically manipulates particles in a large area [52, 53]. Furthermore, this method has been proved in nanowire fabrication in Fig. 2.5b [54] and live cell manipulation [55, 56].

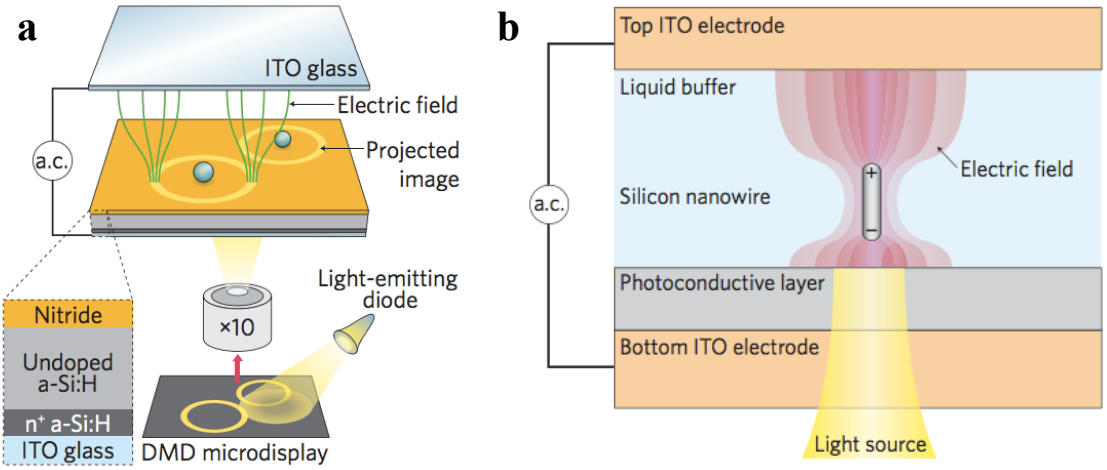

Figure 2.5 (a) optoelectronic tweezers [52] (b) nanowire fabrication with optical trapping [54]

The advantages of OET systems over other optical tweezers systems are prominent. It is a massively parallel manipulation in a large area with the versatility of optical tweezers. Its non-damaging radiation of dielectrophoretic forces are utilized in many applications, includes cell sorting and nanoparticle applications [57, 58]. However, the requirement of non-conducting solution limits its use in biology and biomechanics, because most biological molecules and live cells need to be in their conductive culture media. The

reported conductivity in cell manipulation is 0.1 mS/cm with OET [53, 59], while the conductivity of cell culture medium is usually greater than 1.2×10^4 mS/cm at room temperature [60]. Also, the optoelectronic tweezers operate at RF frequency instead of light frequency, which involves more noise and disturbance from the ambient environment and limits the resolution of trapping [22].

Moreover, all above techniques are not readily compatible with certain technologies including micro-electro-mechanical systems (MEMS), which are utilized to detect and measure various properties of biological samples. For example, MEMS resonators possess extraordinary sensitivity to the mechanical properties of cells and bio-molecules and can resolve their properties [61-67] including mass, density, size, and stiffness with a resonant frequency shift by responding to mass additions or changes in attached bio-samples. In a particularly interesting application, optical trapping could aid these resonant devices [68] in the precise measurement and monitoring of single cells and their physical properties, enabling critical biological studies, including consideration of cell-growth size dependencies or unregulated growth applicable to understanding cancer mechanisms or those of other diseases [69]. This relation between mass and cell growth is a fundamental question for biologists, and high-resolution measurement can have great potential in medicine and drug discovery. Furthermore, with position-fixed cells on the resonator, optical trapping could mitigate drift error and enhance the precision and accuracy of the overall resonator measurements.

Integrating optical trapping with MEMS while maximizing cell vitality presents some unique challenges. OET accomplishes large-scale parallel manipulation with two electrodes to achieve low-intensity optical trapping and avoids the photodamage effect,

but integrating OET fabrication methods with current MEMS resonators is not straightforward. Plasmonic optical tweezers use highly localized light intensity to increase the trapping force; although used to trap living cells, such as yeast cells [70] and *Escherichia coli* (*E. coli*) [51], the significant amount of heat generated by the plasmonic surface prohibits long-term manipulation of living cells. PhC waveguides also highly localize light energy and trap particles by utilizing evanescent waves; however, the waveguide is not versatile for various eukaryotic cells, whose sizes can vary from 3 μm to 10 μm.

2.5.2 Photo-damage on Biological Samples

Optical tweezing is a widely utilized, non-invasive tool for manipulation in biological applications, such as placement, identification, and modification of living cells [16, 71], in addition to nanoparticles and DNA strands [72]. However, photodamage to cells limits measurement duration and its application in the life sciences. To address this shortcoming, methods have been developed for increased trapping efficiency, and thus trapping at a lower-intensity, such as OET [53], plasmonic optical tweezers [42, 70] and PhC waveguides [12].

In considering the applicability of optical trapping in long-term cell manipulation and its suitability for the proposed applications, it is essential to understand how optical energy affects the cell over time. Although researchers have used the three noted methods to manipulate living cells, insufficient viability measurements of living cells have been reported, and there is few exploration on their viability, while existing cell lifetime research for optical traps used only *E. coli* bacteria cells [20, 40, 73, 74]. These investigations focused more on optimizing wavelength to reduce optical damage,

achieving ~10 minute lifetimes at a ~1100 nm wavelength using an objective lens with a high numerical aperture (N.A. = 1.2) and high laser intensity in the specimen plane [40]. The laser wavelength of optical tweezers is optimized for reducing photo-damaging for living cells [20, 40, 73] and the intensity threshold is explored by many researchers [74]. Fig. 2.6a is the work from Neuman, K. C. et al. [40] and it shows the response of sensitivity of cells to the laser wavelength. The sensitivity is the reciprocal of cell lifetime, which indicates the photo-damage rate by the optical tweezers. The optimal wavelength falls at near-infrared, specifically 850nm and greater than 960nm. Fig. 2.6b is viability measurement of plenty of bacteria with holographic optical trapping by Timp, G. et al. [73].

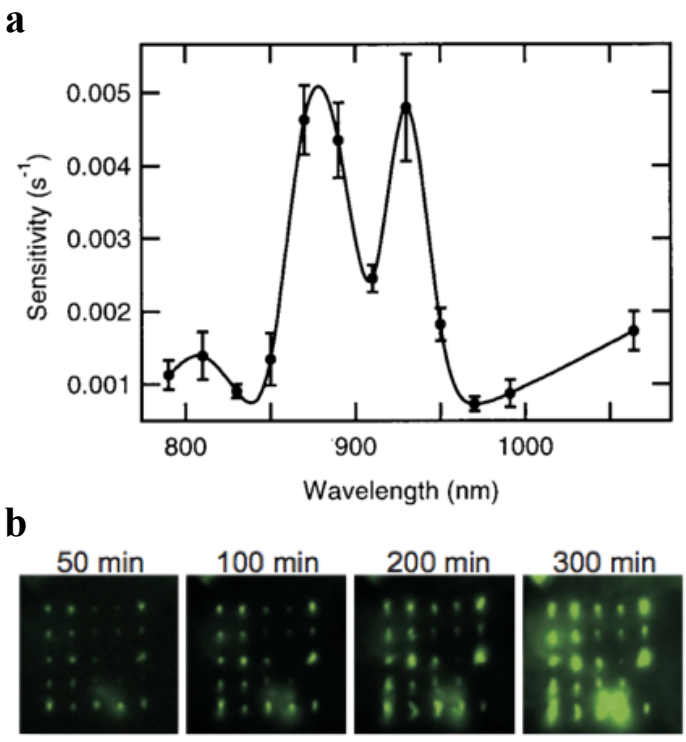

Figure 2.6 (a) cell lifetime characterization regarding laser wavelength [40] (b) bacteria viability characterization with SLM optical tweezers [73]

The linear relation between the sensitivity and the laser intensity has been demonstrated by multiple methods with bacteria including staining with holographic optical tweezers, fluorescence dye and the rotation rate of single bacteria. This linear relation means that the cell damage rate is proportional to the laser intensity, or in another word, to the single photon absorption. Therefore, the thermal damage is thought to be the primary effect in photo-damage [40].

CHAPTER 3 ENHANCED OPTICAL TWEEZERS WITH TWO-DIMENSIONAL PHOTONIC CRYSTALS

We proposed to utilize the localized enhancement trapping originated by diffraction from a two-dimensional photonic crystal (2D PhC). Fig. 3.1 is the schematic drawing of enhanced optical trapping with 2D PhC. The laser vertically incidents on the 2D PhC which consists periodic holes on the substrate. The light is diffracted back into the free space and the trapping spot could be designed above the surface of the substrate with carefully adjusting the sizes and periodicities of the holes.

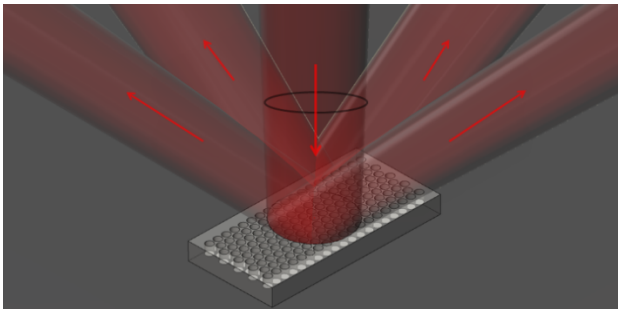

Figure 3.1 The schematic drawing of the proposed patterned optical trapping on a 2D PhC platform

In this chapter, the diffraction analysis will be discussed in Section 3.1 using Fresnel-Kirchhoff diffraction formula and Fourier optics. This analysis will be utilized in the design and simulation of the PhC. It is not straightforward to get analytical solution for the Kirchhoff's diffraction formula and for the gradient force equation. Therefore, the structure of the PhC platform is precisely simulated and optimized with a finite-difference time-domain (FDTD) method in Section 3.2. The trapping experiments are conducted with the designed PhC structures. Section 3.3 describes patterned trapping using all orders of the diffracted light, and Section 3.4 shows the trapping enhancement

by the diffraction of 2D PhC. In Section 3.5, the photodamage caused by the PhC enhanced trapping are characterized with living cells, including mammalian cells and bacteria, and compared with conventional optical tweezers. The results described in this chapter have been published in ACS Photonics [75] and Scientific Reports [76].

3.1 Wave Propagation Theory in a Two-Dimensional Photonic Crystal with Vertically Incident Light

The diffraction from the 2D PhC can be analyzed by Fresnel-Kirchhoff diffraction formula or Huygens-Fresnel's equation. Fig. 3.2 is the comparison between the numerical calculation from Kirchhoff diffraction formula and the FDTD simulation by a Lumerical FDTD solver. The light source is confined by a finite window that originates the diffraction phenomenon. The intensity distribution over the space matches each other, and the diffracted light is focused at $3\mu m$ above the light source.

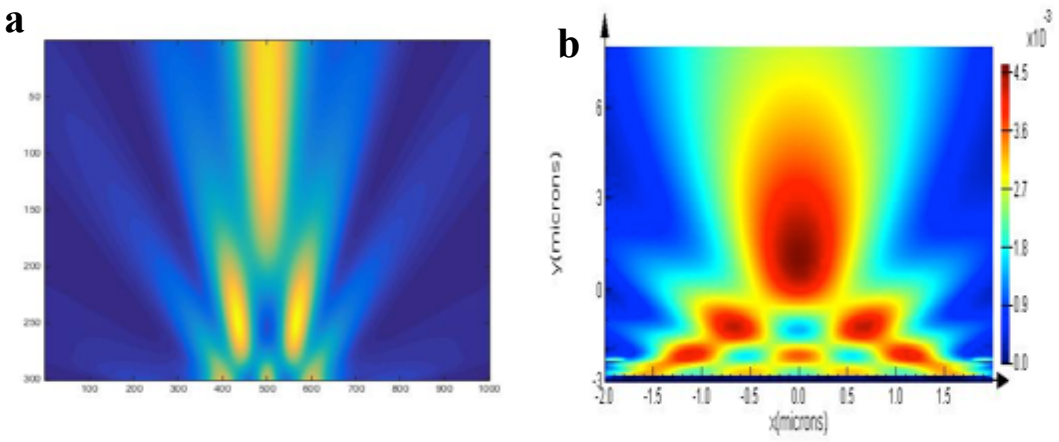

Figure 3.2 Diffraction of from a finite window (a) numerical calculation using Kirchhoff's diffraction formula (b) finite-different time-domain simulation by Lumerical FDTD

The height of the focus determines the trapping position, and it could be controlled by the size and depth of the PhC holes. The light focus is designed above the surface of the substrate with a shallow depth by carefully adjusting the size of the finite window. The height of the focus is estimated by Fourier optics in the spatial frequency domain.

The diffraction of the finite window changes the propagation directions of the input plane waves. When the size of the hole is small compared to the width of the Gaussian laser beam, we can assume a plane wave vertically incident on the circular window and the electric field is given by the following.

$$E(x) = \begin{cases} A & -r < x < r \\ 0 & else \end{cases} \tag{3.1}$$

where A is the amplitude of the input plane wave, and r is the radius of the circular window.

The Fourier transform of the plane wave is

$$E(x) = \int_{-\infty}^{\infty} c(\omega) e^{i\omega x} dx \tag{3.2}$$

$$c(\omega) = \frac{1}{2\pi} \int_{-\infty}^{\infty} E(x) e^{-i\omega x} dx = \frac{A}{\pi} \frac{\sin(\omega r)}{\omega} \tag{3.3}$$

where ω is the spatial frequency, so $\omega = k_x = ksin(\theta)$ and θ is the azimuth angle. Fig. 3.3a shows an example of the amplitude of the light propagating in different directions. To estimate the height of the focus, we could only consider the top-three highest amplitude at ω_0, ω_{-1}, and ω_{+1} The focus position can be estimated by where these three lights intersect. The ω_0 light propagates perpendicularly and $\omega_{\pm 1}$ have the symmetric

azimuth angle. Therefore, these three light rays intersect at the same point above the perpendicularly incident light source, as shown in Fig. 3.3b.

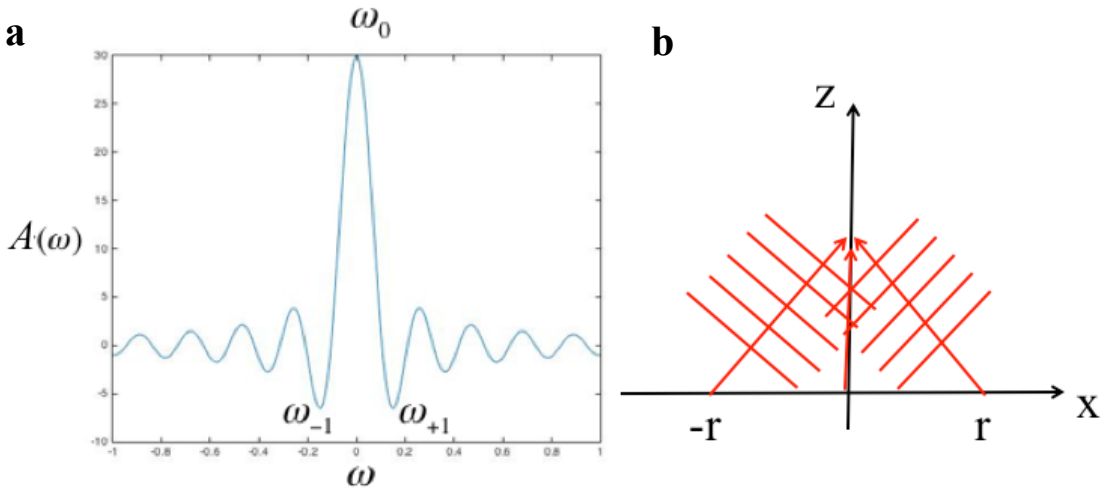

Figure 3.3 (a) Fourier transform of finite plane wave in spatial frequency domain (b) schematic drawing of focus position estimation

The $\omega_{\pm 1}$ can be calculated by Eq. (3.3)

$$|\omega_{\pm 1} \cdot r| = 4.49 \tag{3.4}$$

Because $\omega = ksin(\theta)$ and $|sin(\theta)| \leq 1$, we can get the height of the focus in Eq. (3.5) as well as requirement in Eq. (3.6) to achieve the $\omega_{\pm 1}$ light. If the radius r cannot meet this requirement, we could not get the light propagating in different directions and thus there will be no focus effect outside the substrate.

$$h \approx \frac{r}{\tan(\theta)} \tag{3.5}$$

$$r \geq \frac{4.49}{k} = \frac{4.49\lambda}{2\pi n} \tag{3.6}$$

where k is the wave vector of the light, n is the refractive index and λ is the wavelength. In the following simulation and experiments, we will use $1064\ nm$ wavelength laser. Therefore, the radius of the holes must be greater than $572\ nm$. This estimation of the dimensions of holes and the height of the focus can be used as a start number for the following simulation and optimization process.

3.2 Finite-Difference Time-Domain Simulation

Finite-Difference Time-Domain (FDTD) simulation is a time-domain numerical analysis method for finding approximate solutions of Maxwell's Equations. As shown in Eq. (2.14), it is not straightforward to find analytical solutions for vertical waves modulated by 2D PhC and FDTD technique is more widely used in this case. We performed simulations of the modulated light field produced by a PhC with shallow holes using the FDTD method through the open-source software package MEEP [77].

It is important to note that the center of the diffraction light is an enhanced trapping region. To demonstrate the enhancement effect, FDTD results are represented in Fig. 3.4 on a square lattice PhC with a period of 5.8 μm and 3.6 μm-diameter holes. Various hole depths were simulated, and 500 nm was found to be optimum to avoid confining the optical energy inside the holes. This optimized depth also works well with most of the cells in our experiments. Fig. 3.4a shows the optical energy density distribution of the modulated light field, presented by both vertical and horizontal cross-sections at different heights. The vertical cross-section shows that the modulated light field generates a focused volume for the optical trap located at about 1.67 μm above the surface of the 2D

PhC. The four images on the left side of Fig. 3.4a are horizontal cross-sections at the height of 0.3, 1.7, 3.0 and 4.3 μm above the PhC surface.

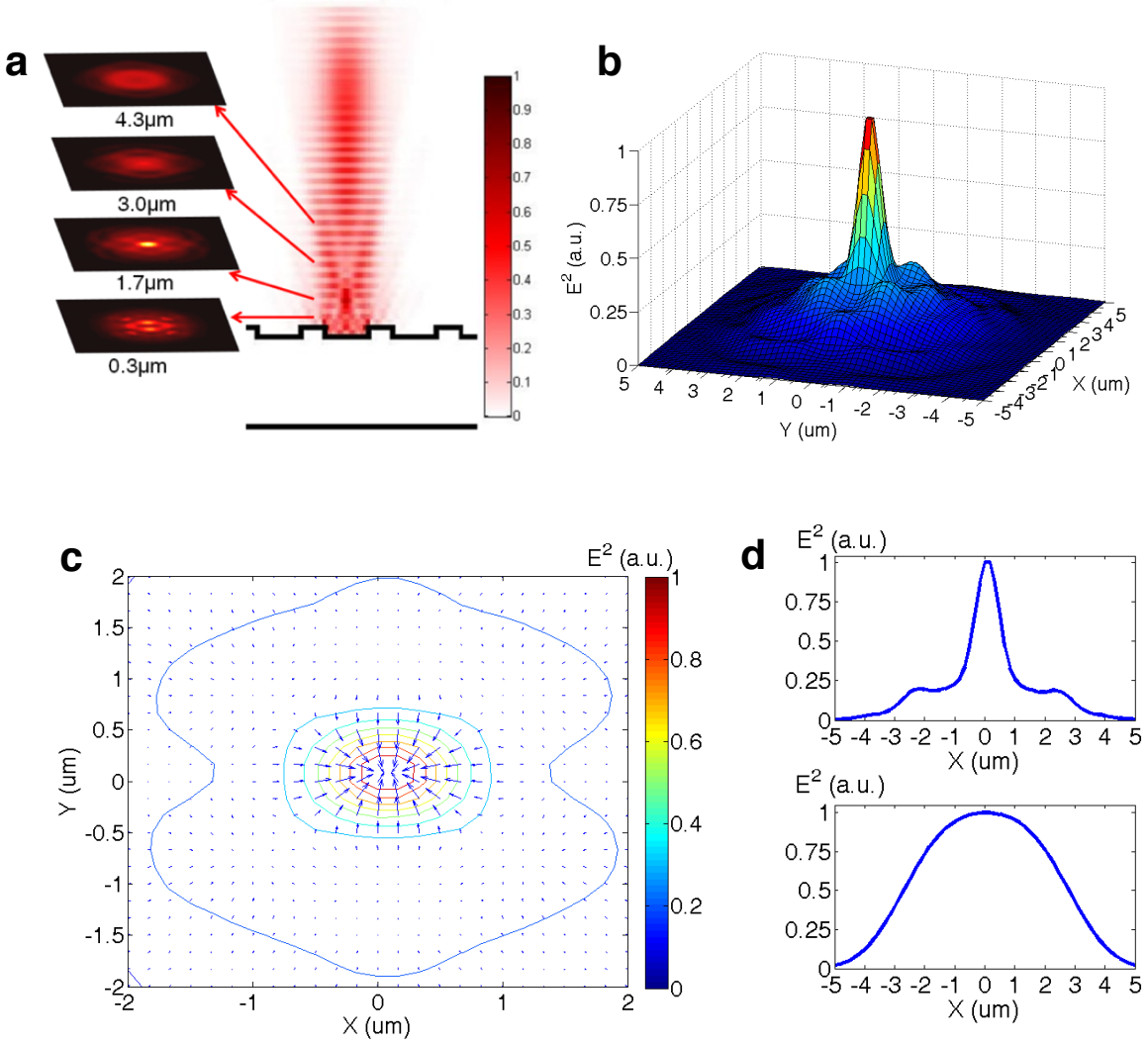

Figure 3.4 FDTD simulation of the laser light field modulated by a 2D PhC, demonstrating enhanced optical trapping through increasing gradient of the intensity distribution. The PhC is a square lattice with a period of 5.8 μm and 3.6 μm-diameter holes. (a) Vertical cross-section of the optical energy density and corresponding horizontal cross-sections at 0.3, 1.7, 3.0 and 4.3 μm above the surface of the 2D PhC. (b) 3D surface plot of the optical intensity at the trap location, ~1.67 μm above the surface of the PhC surface. (c) Contour and gradient of the optical intensity at the trap plane. (d) Comparison of the trap potential between the PhC-modulated light field and the Gaussian profile in traditional laser traps.

Fig. 3.4b shows a three-dimensional shaded surface plot for the horizontal cross-section of the intensity distribution at the trap location. The contour and gradient of the intensity at this height are shown in Fig. 3.4c. The asymmetry of the gradient along the x- and y-axis is caused by the light polarization. Because the trapping force is proportional to the gradient of the light intensity distribution $\left(\vec{F} = \frac{\alpha}{2}\nabla\vec{E}^2\right)$, Fig. 3.4c also indicates that the enhanced trapping potential generated by the PhC-modulated light field. This enhancement is further confirmed by Fig. 3.4d, which shows a comparison between trap potentials (proportional to the intensity distribution) in traditional laser trapping without a PhC and that above the surface of the 2D PhC. The top diagram is the normalized energy density along the x-direction of the PhC-modulated light field, and the bottom graph is the distribution for traditional laser trapping. By increasing the gradient of the intensity distribution, enhanced trapping force is generated above the 2D PhC surface.

Because the incident laser beam is affected by the trapped particle, a comparison of trap enhancement is performed with and without a 2 μm-diameter polystyrene sphere above the PhC. The result in Fig. 3.5 shows that the trapped particle above the surface further focusing of the incident light [78, 79] and therefore enhancing the optical trap.

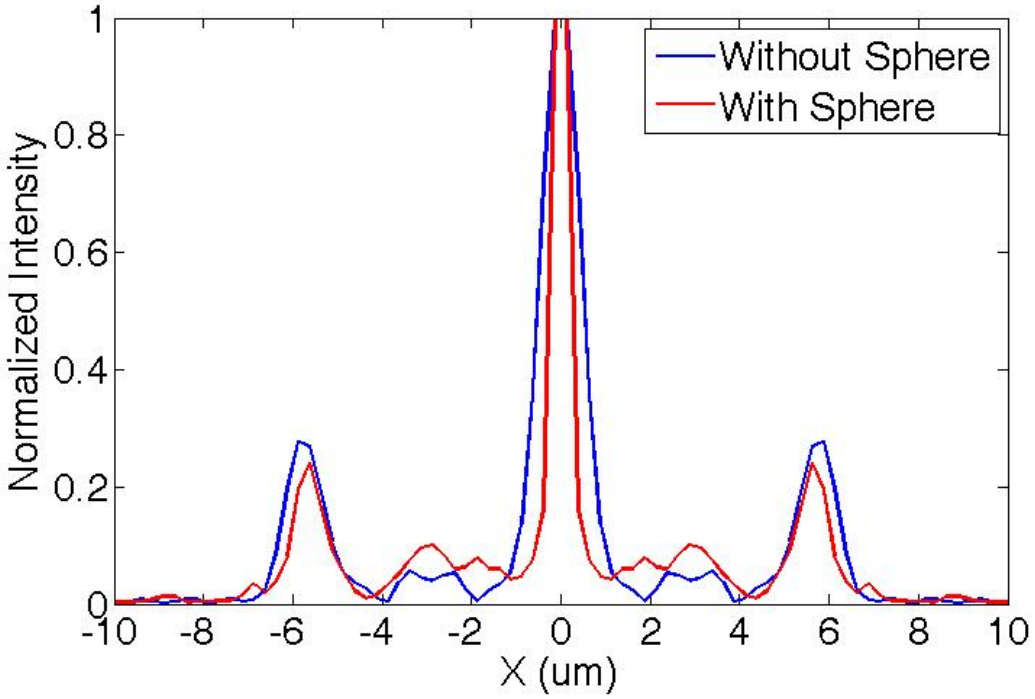

Figure 3.5 FDTD simulation of comparison between reflected intensity profile with and without a 2μm-diameter polystyrene sphere above the PhC

To investigate the possibility of trap enhancement due to the effect of the standing wave caused by interference of the incident and reflected light, a Gaussian pulsed-laser beam is also used as the light source to eliminate interference. The FDTD simulation results in Fig. 3.6 shows a similar light confinement effect, suggesting that the enhancement is mainly caused by the reflected light field modulated by the PhC.

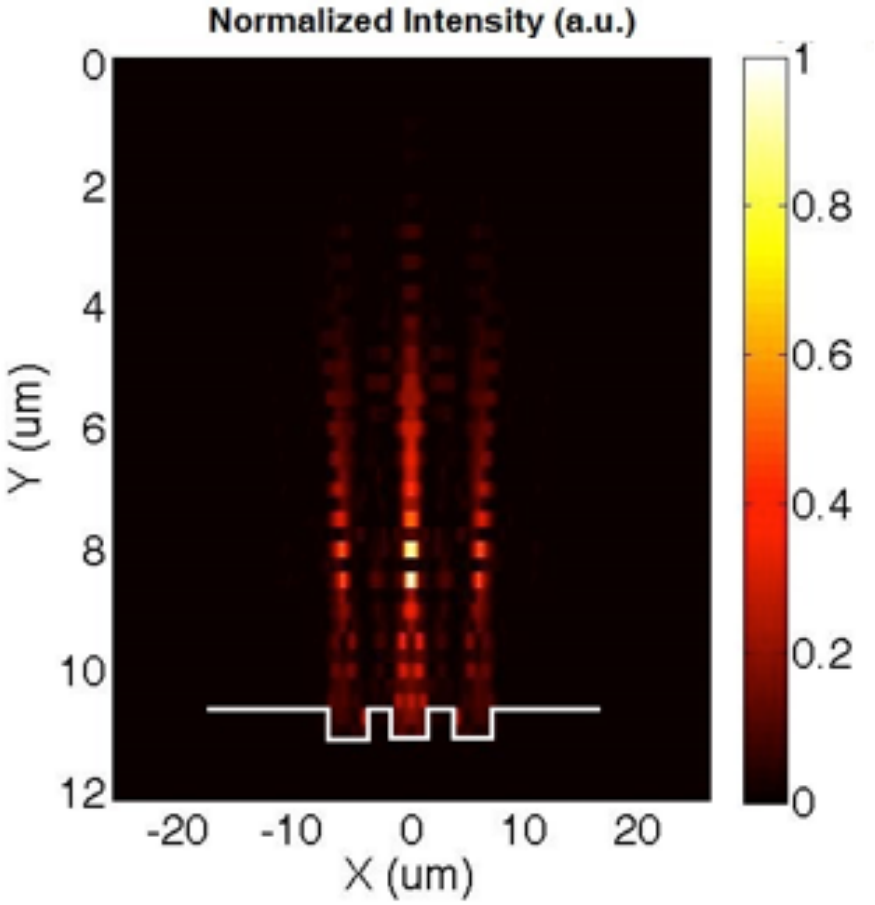

Figure 3.6 FDTD simulation of a 1-μm-pulse-width Gaussian pulsed-laser reflection above a 2D PhC

3.3 Patterned Optical Trapping

The optical setup is shown in Fig. 3.7. A loosely focused laser beam is incident upon the surface of the PhC, producing a 2D diffraction pattern for optical trapping. Infrared light at a wavelength of 1064nm generated by a Nd:YVO_4 laser is used as the light source. It is directed into a Zeiss Axio Imager fluorescence microscope and irradiates normal to the surface of the PhC through a beam splitter and an objective lens. The diameter of laser beam spot is about 53 μm and 25 μm when focused by a 20x objective lens (N.A.=0.22) and 50x objective lens (N.A.=0.55), respectively. The laser power on the PhC surface is

adjustable and is operated at 8.4mW under 20x objective lens and 4.3mW under the 50x objective lens in the experiment, which results in an optical intensity of 3.7μW/μm^2 and 9 μW/μm^2, respectively. The particles used in the trapping experiments are 1μm diameter polystyrene beads and oblong-shaped polystyrene beads with a long diameter ~6.8 μm. Fig. 3.8 shows an optical microscope image of the 2D PhC structure. Although it does not have complete periodically ordered structure as regular PhC, literature has shown that such hyper-uniform PhC structure with a short-range geometric order can still achieve complete photonic bandgaps [80], and it can alleviate the requirement on e-beam lithography significantly.

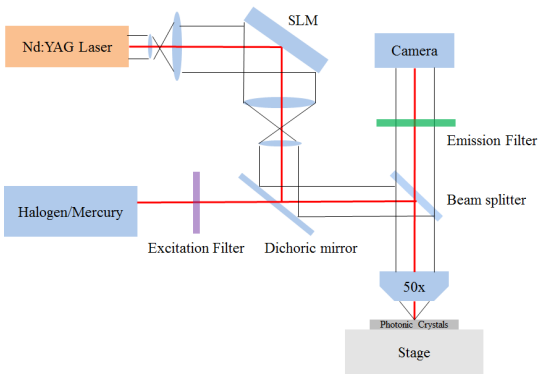

Figure 3.7 Schematic diagram of the optical system for the PhC optical trapping experiments

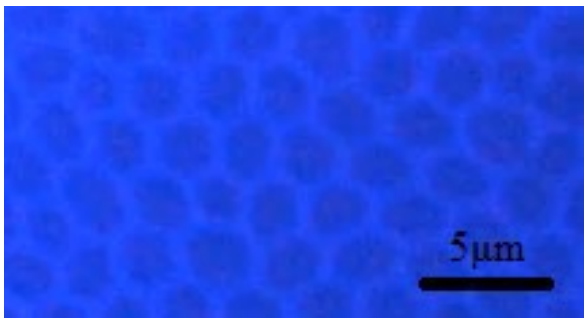

Figure 3.8 A top-view optical image of the 2D PhC used for patterned optical trapping

3.3.1 Patterned Diffraction

The method entails designing the PhC structure to modulate the incident optical field and to create efficient optical traps. The configuration of the optical traps is generated by light modulation and therefore depends on the dimensions of the 2D PhC. If the depth of the holes in the PhC is much greater than the hole-diameter, most of the energy is confined inside of the features of the PhC, and the particles are trapped by evanescent waves [13,

50, 81]. However, if the holes are shallow, most of the modulated light is scattered back into free space and generates an efficient trap positioned above the surface of the 2D PhC. MEEP FDTD solver is used for modeling the diffraction patterns from the 2D PC and compare it with experimental results in Fig. 3.9.

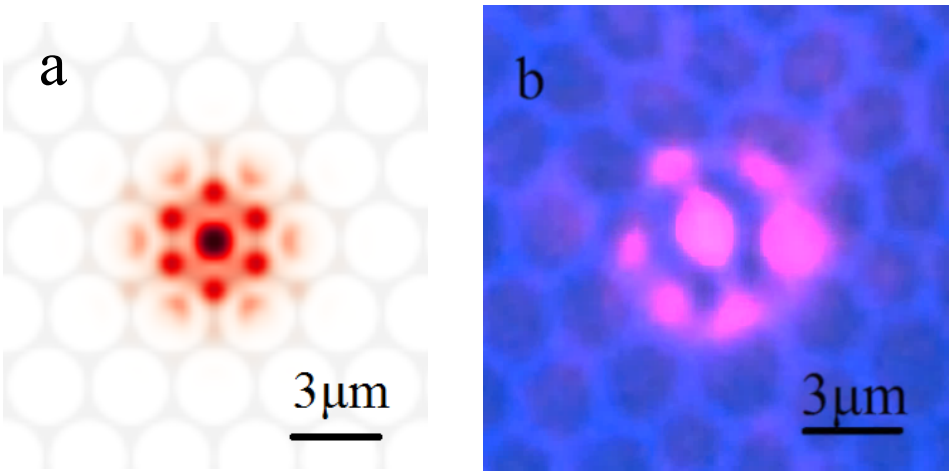

Figure 3.9 (a) FDTD simulation using MEEP. The dimension of a single cell in the PhC is 2.9 μm and each hole is cylindrical in shape. The background shows the 2D PhC. The incident light is set as a Gaussian laser beam with 1064 nm wavelength and the beam profile is assumed to be similar to what is observed in this experiment, covering three holes. (b) Light intensity distribution above the surface of the 2D PhC under a 50x objectives lens, showing 2D diffraction by the periodic structure of the PhC.

The comparison between simulation and experimental results can support the conclusion that the trapping pattern is determined by the structure of the 2D PhC. In the modeling, the size of the single cell in the PhC is set as what is used in the experiment (2.9 μm), and the Gaussian beam laser profile covers three holes. A typical regular hexagonal PhC structure is assumed for the modeling. The images of diffracted light intensity distributions and trapping results are recorded by a CCD camera connected to the microscope. Fig. 3.9b shows the experiment result of the diffracted beam profile under the 50x objective lens. Although the PhC platform is a hyper-uniform PhC structure [50]

with a short-range order as shown in the background of Fig. 3.9b, the simulation result (Fig. 3.9a) and experiment result (Fig. 3.9b) match each other reasonably well.

To demonstrate the determinant role of PhC in creating trapping patterns and specifically the flexibility of pattern control, we generated different trapping patterns with the same PhC. The diffraction and trapping patterns in Fig. 3.10 are produced by focusing the laser spot in the center of a hole and at the intersection of three holes. In Fig. 3.10a and 3.10b, the laser spot is set in the center of a hole which generates a diffraction pattern consisting of a more intense center and six weaker outer spots. The center pattern traps three beads and the outer spots each trap one bead except the spot on the left which catches two beads simultaneously. The locations of the outer beads are not the same as the diffraction pattern, which may be attributed to the utilization of the hyper-uniform PhC that does not have the same structure as the regular periodic hexagonal structure used in the simulation. The divergence of the diffracted beams also affects the location of the trapping beads. The laser spot is then moved to the intersection of three holes, which produces a hexagon diffraction pattern with a center maximum and three prominent outer spots. Fig. 3.10c shows the FDTD modeling result and Fig. 3.10d shows the patterned trapping of the micro-beads which agree with the modeling result well. More complex trap arrays and reconfigurability can be achieved by incorporating a SLM or polarization control in the optical system. Here we demonstrate one way to reconfigure the trap pattern using polarization control dynamically. The 1μm polystyrene beads are first trapped by a linearly polarized laser beam above the surface of the 2D PhC, as shown in Fig. 3.10e. When the polarization is rotated 40 degrees, the trap pattern is rotated accordingly (Fig. 3.10f). The scale of the pattern is enlarged slightly during the process, which may be

caused by the different periodicity of holes in various directions and the semi-random distribution of holes.

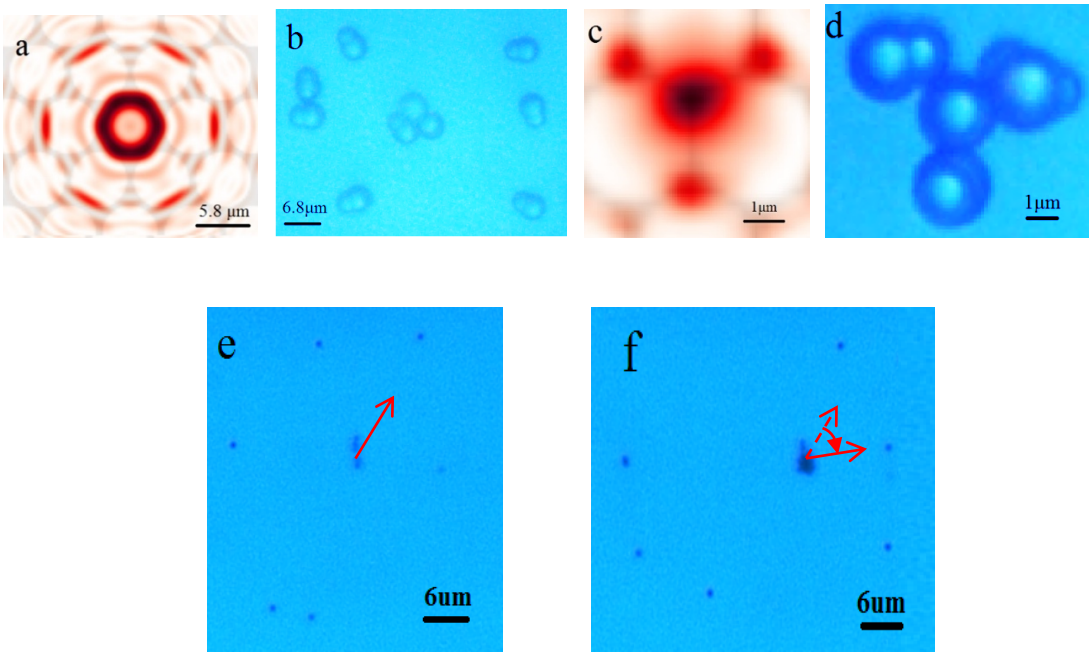

Figure 3.10 (a) FDTD modeling result with the focused laser spot in the center of a hole, generating a hexagon diffraction pattern. The unit cell size of the 2D PhC is 5.8 μm, which is what is used in this experiment. (b) The patterned optical trapping experimental results of micro-beads corresponding to the conditions in Fig. 3.10a, except a hyper-uniform PhC with a short-range order is used instead of the regular hexagonal structure assumed in the simulation. (c) FDTD modeling result with the focused laser spot at the intersection of three holes, generating a hexagonal diffraction pattern. (d) The optical trapping experimental results corresponding to the conditions in Fig. 3.10c. (e) The trap pattern of 1μm beads generated using a laser beam polarized linearly along the direction indicated by the red arrow. (f) The trap pattern of 1μm beads after the laser polarization is rotated 40 degrees.

3.3.2 Trapping Efficiency of the Patterns

To characterize the trapping efficiency, the stiffness and minimum trapping intensity are measured using polystyrene beads of sizes ranging from 200 nm to 1 μm as the trapped particles. Histograms of the displacement of 1 μm beads trapped at the center of the diffraction pattern are shown in Fig. 3.11a and 3.11b. The results are nearly Gaussian

profile, allowing calculation of the stiffness by the equipartition method. The minimum incident optical intensity to maintain the static trapping is shown in Fig. 3.11c. Two sets of data are shown here. The upper one (represented by the circular data points) shows the measured minimum intensity for trapping the beads in the whole diffraction pattern. The intensity is then reduced, and the beads at the outer part of the pattern start to escape due to Brownian motion. As the intensity is further reduced, the beads at the center of the pattern begin to escape too. The lower curve (represented by the square data points) shows the minimum intensity to maintain a stable center trap. The trapping intensity ranges from <1 $\mu W/\mu m^2$ for 1 μm beads to ~16 $\mu W/\mu m^2$ for 100 nm beads for the lower curve, and ~6 $\mu W/\mu m^2$ for 1 μm beads to ~30 $\mu W/\mu m^2$ for 450 nm beads for the upper curve. These are significantly lower than optical intensities used for trapping micron-size particles in conventional optical tweezers (~ 1mW/ μm^2) [52]. It is also lower than the results reported in Ref. [14] which used a 633 nm laser and a 1D PC structure.

The trap stiffness can be obtained by characterizing histograms of displacements under a particular incident optical intensity. For this measurement, it is kept at $3.5\ \mu W/\mu m^2$ under 20x objective lens. The results are shown in Fig. 3.11d. We then increase the power to ~17 $\mu W/\mu m^2$ to have a more stable trapping. For 1μm polystyrene beads, the trap stiffness is raised to $0.36\ pN/\mu m$ in X direction and $0.179\ pN/\mu m$ in Y direction. When the same input laser power is focused by a 50x objective lens, the trap stiffness is $0.387\ pN/\mu m$ in X direction and $0.281\ pN/\mu m$ in Y direction. This result shows that a loosely focused laser beam can achieve almost the same stiffness as a tightly focused beam. Fig. 3.11d also shows a linear relation between particle size (in log scale) and the stiffness calculated by the equipartition method. Currently, there is a glass spacer of 0.18

mm thickness between the particles and the PhC substrate. The stiffness is expected to be further improved by trapping particles closer to the surface of the 2D PhC.

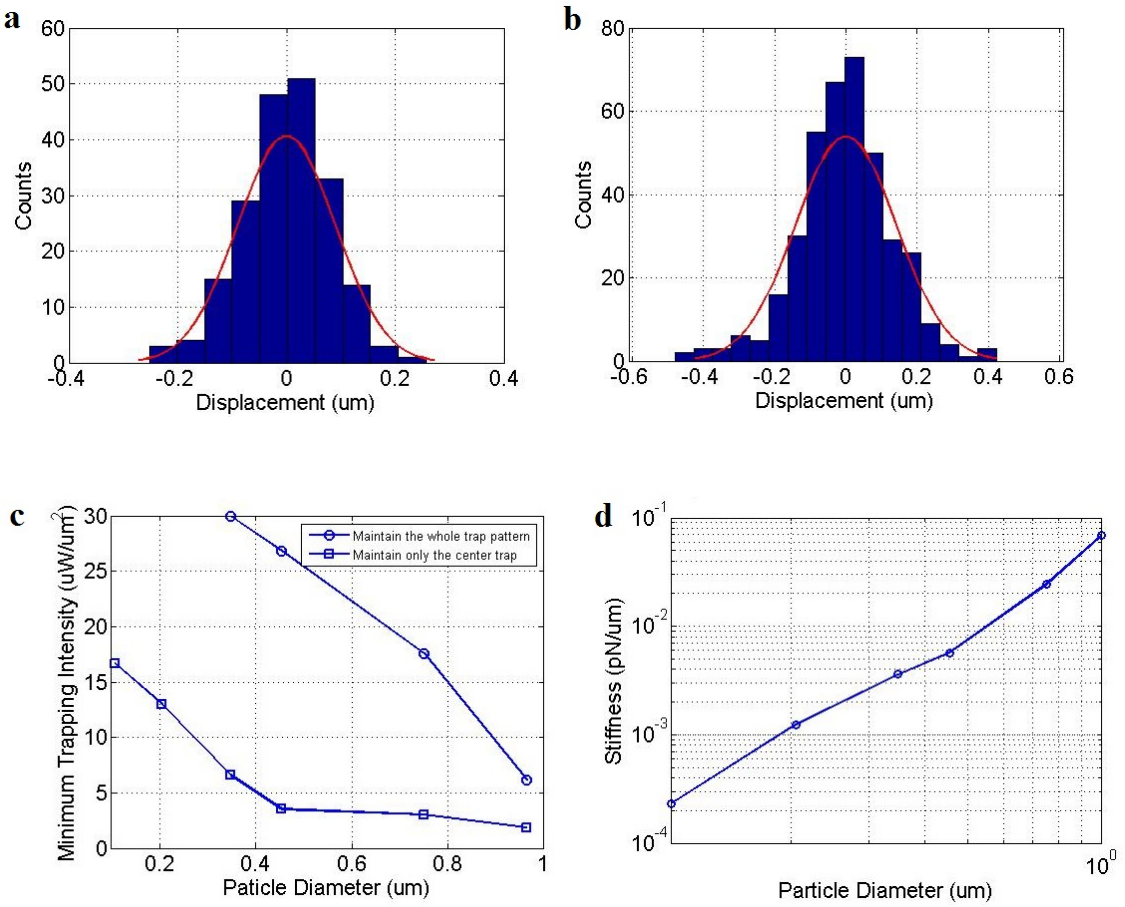

Figure 3.11 Histogram of displacement of trapped 1 μm polystyrene beads (a) in X direction (b) in Y direction (c) and (d) Minimum trapping intensity and trap stiffness in X direction measured with an input intensity of 3.5 $\mu W/\mu m^2$ for polystyrene beads of various sizes under the 20x objective lens.

The scale of trapping pattern is determined by the structure of 2D PhC regardless of the size of loosely focused beam spots. To investigate the effect of the beam spot size on the patterned optical trapping result, we performed the trapping experiments on the same 2D PhC platform with the laser beam focused by the 20x and 50x objective lenses. The results are shown in Fig. 3.12a and 3.12c, respectively. Fig. 3.12b shows the enlargement

of Fig. 3.12a to the same scale as Fig. 3.12c for comparison. The trapped bead patterns appear to be similar in both cases with the same scale even though the incident laser beam sizes are different. The size of the unit cell is 2.9 μm for the 2D PhC structure used in these experiments, which is half of the 2D PhC unit cell size used in the experiments generating the results shown in Fig. 3.8. This results in higher divergence of diffracted beams and therefore wider separations between the trapped beads. Also, compared to Fig. 3.12b, one trapping point is missing from the lower-left corner in both Fig. 3.12b and 3.12c. This may be caused by the semi-random distribution of the holes and that a different platform with a different unit cell size and somewhat different PhC structure is used.

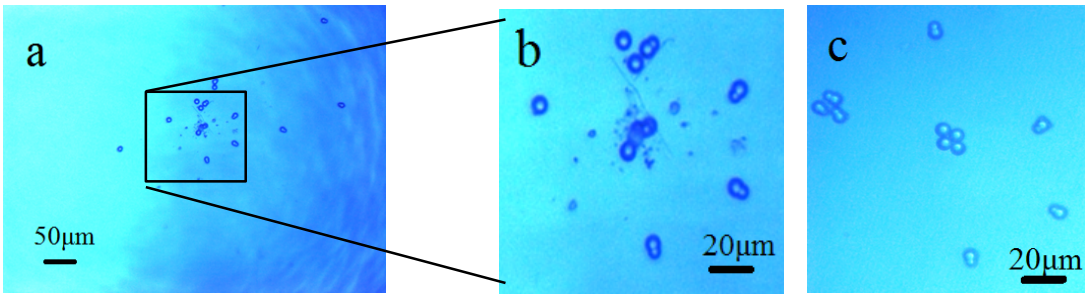

Figure 3.12 (a) Patterned trapping of micro-beads under 20x objective lenses and- (b) enlargement of the center optical trap area. (c) The same trapping experiment but under 50x objective and therefore smaller focused laser spot size. The result shows similar trapped bead pattern to that shown in (b).

Overall the experimental results support the observation that the optical trap pattern is determined by the structure of the 2D PhC and how it interacts with the incident laser beam; various patterns with different scales and shapes can be achieved by designing these parameters.

3.4 Enhanced Optical Trapping

The utility of the proposed method was first verified using eukaryotic yeast cells, which are typically 3-4 μm in diameter. The Nd:YVO_4 1064 nm continuous wave (CW) laser is first used to trap cells with a 50X objective lens (N.A. = 0.55). The details of the optical setup are the same as Fig. 3.7. Fig. 3.13a shows an optical microscope image of the 2D PhC structure and the snapshots in Fig. 3.13b show dynamic trapping and dragging of a yeast cell along the 2D PhC surface. A 1.2 μm layer of parylene-C was deposited on top of the PhC platform to create a thin, transparent polymer film that protects and better planarizes the PhC surface.

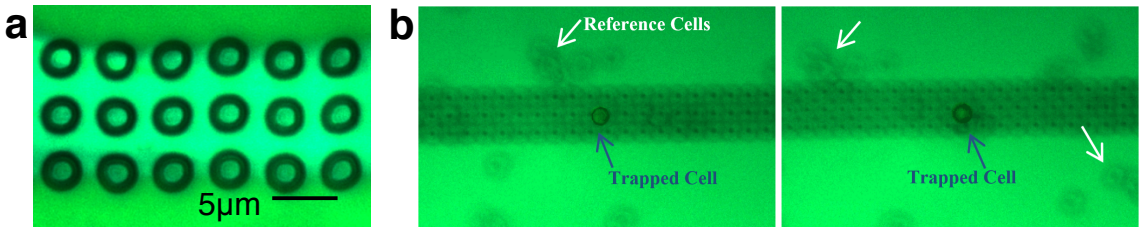

Figure 3.13 (a) An optical microscope image of the 2D PhC. (b) Images of yeast cells being trapped (left) and dragged (right) on the surface of the 2D PhC.

To characterize the trapping efficiency, we measured the stiffness and minimum trapping intensity by trapping polystyrene beads of sizes ranging from 0.2 - 1 μm. Stiffness is defined and measured by Eq. (2.15) and (2.22). The minimum trapping intensity is measured under microscope. The intensity is the average intensity determined by dividing the optical power under the microscope objective lens by the area of the Gaussian beam. The beam radius w is directly measured under microscope by the full width at half maximum (FWHM) and computed by $w = \frac{FWHM}{\sqrt{2ln2}}$. A single particle is trapped at higher power, and the power is reduced until the particle escapes from the trap. The lowest

power and intensity are then recorded as the minimum trapping power and intensity. Fig. 3.14a shows the relative frequency histogram of the Brownian motion of a trapped 750 nm polystyrene bead under 5.8 $\mu W/\mu m^2$ laser intensity with (red) and without (blue) the 2D PhC platform. The beads are more firmly trapped above the 2D PhC platform, and their motion distribution is narrower than the distribution without the 2D PhC. These findings are consistent with the FDTD simulation results. The histograms follow Gaussian distributions, allowing calculation of the stiffness by the equipartition method [12]. The trap stiffness is obtained by characterizing the displacement histogram under a specific incident optical intensity. The stiffnesses were 0.156 pN/μm with PhC and 0.030 pN/μm without PhC. Fig. 3.14b shows the minimum trapping intensity required to confine the beads and the stiffness measurement for various sized polystyrene beads. Two sets of data are shown: the measured minimum intensity for trapping polystyrene beads with sizes ranging from 0.2-1 μm; the trap stiffness measured at an intensity of 0.35 $mW/\mu m^2$ (minimum intensity to trap the 0.2 μm beads) above the surface of the 2D PhC for the polystyrene beads (red curve). The polystyrene beads were initially trapped with higher intensity above the center of a hole in the 2D PhC. The intensity was then decreased, and the minimum trapping intensity value was recorded when the trap released the beads. The minimum trapping intensity in Fig. 3.14b is significantly lower than with conventional optical tweezers, which typically requires ~1 $mW/\mu m^2$ [53].

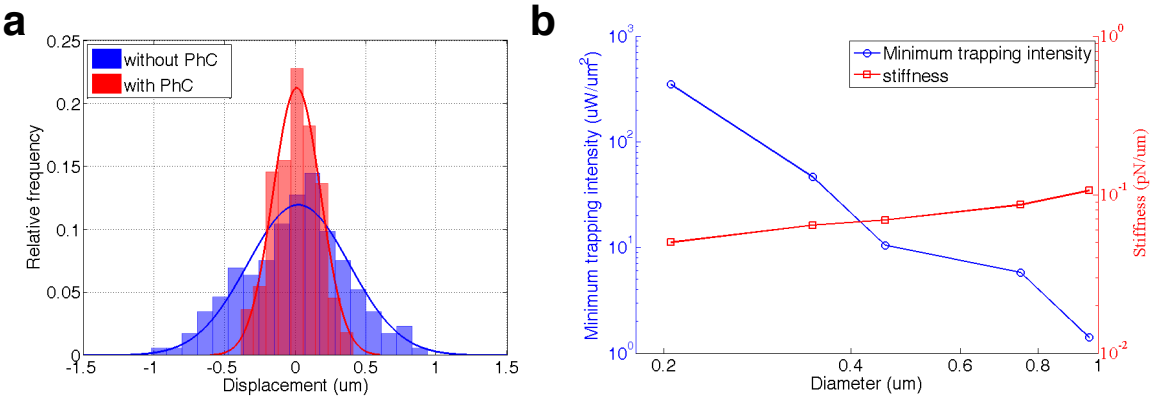

Figure 3.14 Optical trapping efficiency characterizations. (a) Relative frequency histograms of random movement for trapping 750 nm polystyrene beads at a 5.8 μW/μm^2 laser intensity with (red) and without (blue) the 2D PhC platform. The stiffness is 0.156 pN/μm and 0.030 pN/μm, respectively. (b) Minimum trapping intensity (blue) and stiffness (red) for different sizes of polystyrene beads at the laser intensity of 0.35 mW/μm^2.

3.5 Cell Viability Characterization

Optical trapping has become a widely utilized, non-invasive tool for manipulation, while photodamage to cells limits the measurement duration and its application in the life sciences. In considering the applicability of optical trapping in long-term cell manipulation and its suitability for the proposed applications, it is essential to understand how optical energy affects the cell over time. Although researchers have used the previously noted methods to manipulate living cells, insufficient viability measurements of living cells have been reported, while existing cell lifetime research for optical traps used only Escherichia coli (*E. coli*) bacteria cells [20, 40, 73, 74]. These investigations focused more on optimizing wavelength to reduce optical damage, achieving ~10 minute lifetimes at a ~1100 nm wavelength using an objective lens with a high numerical aperture (N.A. = 1.2) and high laser intensity in the specimen plane [40]. Therefore, experimental research in this area on eukaryotic cells with optical tweezers is not entirely

explored. Moreover, even though laser wavelength can be optimized, the photodamage is still a severe limit for the long-term biological study of living cells.

In our experiments, a simple optical setup was used to guide a loosely focused laser beam onto the surface of a 2D PhC, which then modulates the profile of the laser beam and generates a confined trapping area above the surface of the 2D PhC. The prolonged cell viability (~30 min) is achieved, confirming that the 2D PhC uses less power while sustaining the same cell trapping force. A higher trap stiffness can also be demonstrated by trapping polystyrene beads and *E. coli* cells, and these experimental findings were consistent with FDTD simulation results in Section 3.2. The highly localized intensity in the method has been a general concern for the viability of cells, and this interest extends to plasmonic and PhC waveguide trapping methods. However, it is experimentally verified that the viability is largely determined by overall intensity, rather than localized intensity.

Although reports have proposed a linear relationship between *E. coli* viability and laser power [73], a systematic characterization of eukaryotic cell viability under optical trapping has not yet been performed. The viability of live NIH/3T3 mammalian fibroblast, yeast, and *E. coli* cells are measured under optical trapping, and it shows that optical trapping with 2D PhC provides higher manipulating capability on live cells. In the viability measurement, cells are suspended in medium containing propidium iodide (PI) (PBS+1% BSA+2 μg/mL PI). PI is a commonly used cytofluorometric indicator to identify apoptotic and necrotic cells. As PI is cell membrane-impermeable, this dye is excluded from live cells. However, during cellular apoptosis or necrosis, the cell membrane loses its selectivity, and PI can permeate the cell and intercalate between DNA

bases. PI binding induces an emission spectrum shift from 535 nm to 617 nm and enhances PI fluorescence 20- to 30-fold [82]. Therefore, apoptotic and necrotic cells may be identified by PI (red) staining. A single-blind method is employed to evaluate cell viability. One scientist set the laser power while another researcher, blinded to the power value, observed and recorded the cell lifetime. The 1064 nm near-infrared CW laser was used to trap cells under a 50× objective lens, and a mercury lamp was used to excite the PI dye during the experiments. Fig. 3.15a shows the time-dependent morphology of a trapped NIH/3T3 cell under 36.0 $\mu W/\mu m^2$ laser intensity. The cell maintained its morphology for more than 30 min before blebbing, as seen by the protrusion from the main cell body. Blebbing of mammalian cells in damaged cells correlates with cells death from either apoptosis or necrosis [83], and was used as a preliminary indication of cell death. Fig. 3.15b shows the measurement results of NIH/3T3 cell lifetime versus PI staining. The time until blebbing (blue curve) and when the cell stained positive for PI (red curve) was observed at each of the laser intensities. As shown in Fig. 3.15b, blebbing had occurred before the cell stained positive for PI, indicating that the PI dye may be constrained by diffusion into the cell and bind with the DNA; therefore, in these experiments, PI staining was not an immediate indicator of cell necrosis. As evident from the trends in Fig. 3.15b, the time interval between blebbing and PI staining was not constant and was dependent on the optical power.

Sensitivity is used as another parameter to quantify photodamage of trapped cells under the optical trap and is defined as the reciprocal of the cell lifetime [40]. Fig. 3.15c shows the sensitivity of mammalian cells based on the measurement results in Fig. 3.15b. The sensitivities using both cell blebbing and PI staining lifetimes exhibit an approximately

linear relationship with the laser intensity, which is consistent with the results reported by Neuman et al. using *E. coli* cells [40]. We also performed the same characterization with *E. coli* cells, and the results are shown in Fig. 4.1d. The sensitivity flattens at low laser intensity and approaches 20 minutes in the lifetime, which matches the replication time of *E. coli* cells.

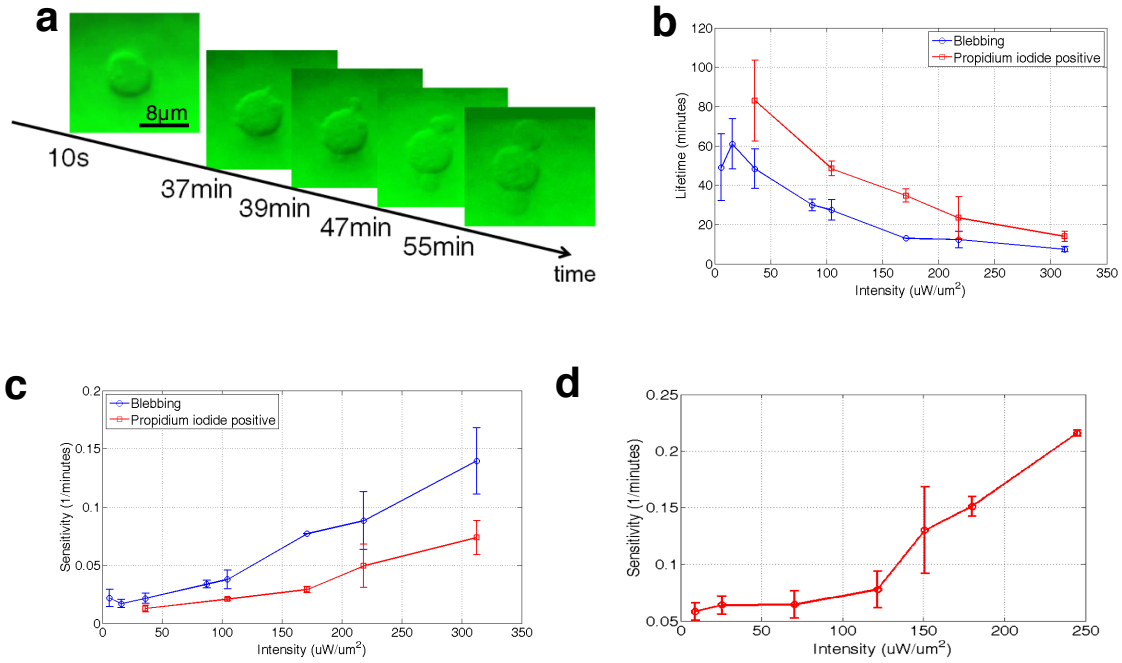

Figure 3.15 Cell viability characterizations. (a) Status of NIH/3T3 mammalian cells under 36.0 μW/μm2 illumination. The cell began blebbing after 30 minutes. (b) Lifetime measurements of the NIH/3T3 cells. The blue and red curves represent the times until blebbing and PI staining occurred, respectively. (c) The sensitivity of mammalian cells, defined as 1/min of the lifetimes reported in (b). (d) The sensitivity of E. coli cells in the PhC optical tweezers. The sensitivity is defined as the reciprocal of the lifetime.

One question in enhanced optical trapping through highly-localized optical fields is whether the effect of photodamage depends on the localized intensity even if the overall power is lower than the conventional optical tweezers. To answer this question, we performed viability measurements of the trapped cell versus incident optical intensity with and without the PhC platform. Fig. 3.16 compares the lifetime and sensitivity of

yeast cells under both trapping methods. The blue curves represent trapping with traditional optical tweezers (without PhC), and the red curves represent trapping on the 2D PhC platform. The two curves are very similar, suggesting that the localized high-intensity light above the surface of the 2D PhC does not compromise cell viability.

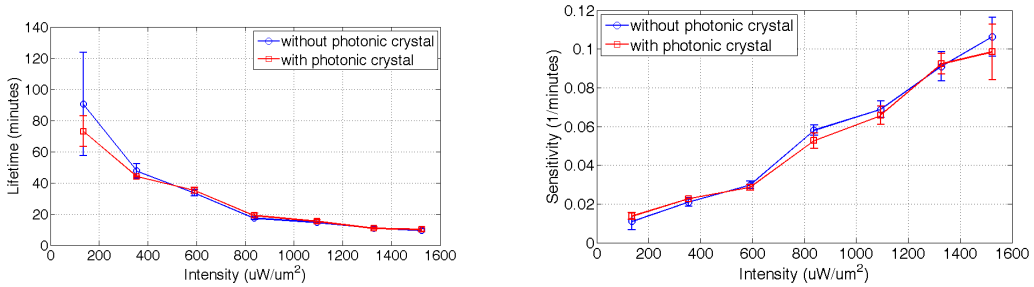

Figure 3.16 Effect of highly localized optical fields on cell viability. (a) Lifetime versus optical intensity for trapping yeast cells with and without the 2D PhC platform. (b) The corresponding cell sensitivity to light intensity. The results show that the cell viability is primarily determined by the overall optical intensity, not the localized intensity.

One advantage of the proposed method over plasmonic optical tweezers is that the locations of the optical traps are not at predetermined "hot spot". As the incident beam moves, the trapped particle moves with the beam as shown in Fig. 3.13b. To further demonstrate this versatility and the potential of parallel manipulation over a broad area on the 2D PhC platform, the objective lens is changed to 20X (N.A. = 0.22), optical trapping is performed, and the trap stiffness is measured on the 2D PhC. Fig. 3.17a shows the relative frequency histogram of Brownian motion for trapped 964 nm-diameter polystyrene beads, and Fig. 3.17b shows the relative frequency histogram of movement for trapped *E. coli* bacteria. The same measurements were performed using the 50X objective lens, and the results were compared. The trap stiffness appears to be unaffected by the objective lens magnification, indicating that particles can be trapped with loosely

focused light under a larger field of view of the microscope. As an example, Fig. 3.17c demonstrates parallel manipulation of yeast cells using a SLM.

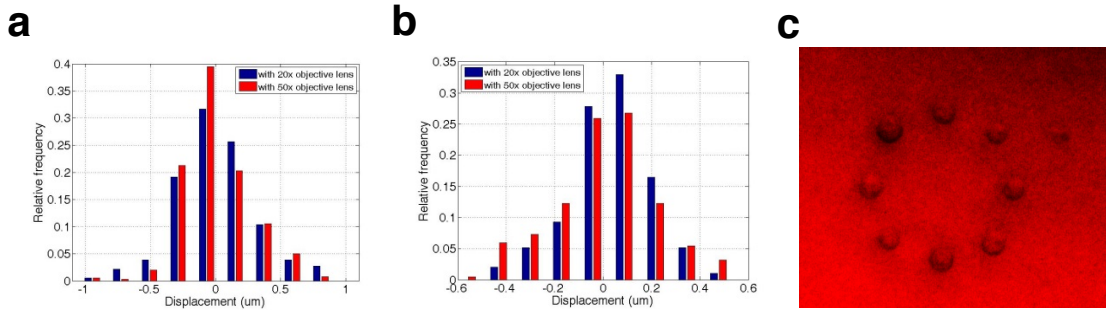

Figure 3.17 (a) Histogram of displacement for trapped 964 nm polystyrene beads under 20X and 50X objective lenses with a 28 $\mu W/\mu m^2$ laser intensity, with stiffnesses of 0.04 pN/μm and 0.06 pN/μm, respectively. (b) Histogram of displacement for trapped E. coli under 20X and 50X objective lenses with a 28 $\mu W/\mu m^2$ laser intensity, with stiffnesses of 0.09 pN/μm and 0.15 pN/μm, respectively. (c) An example of optical trapping with yeast cells using a pre-programmed SLM.

CHAPTER 4 PHOTONIC CRYSTAL ENHANCED OPTICAL TWEEZERS SYSTEM FOR STEM CELL PATTERNING

4.1 Motivation

Cell manipulation is one of the most important applications of optical tweezers. Because of the small trapping force with high resolution, optical tweezers become a popular noninvasive tool to characterize forces and probe the viscoelastic properties of cells, DNAs and proteins [16, 71, 72, 84, 85]. In addition, optical tweezers enable cellular spatial patterning at the single-cell level, which is postulated as important factors in tissue development, and micropatterns of human pluripotent stem cells (hPSCs) are developed for controlling colony geometries and for providing a quantitative assay for studying cellular signaling in early development of tissues [86, 87]. However, only micro-geometric confinement is explored with culturing thousands of cells randomly in a micro-sized well. It cannot avoid randomness in the number of cells and spacing among cells in a colony, which leaves uncertainty to study cellular signaling during differentiation. Furthermore, the cells are limited in their growth area by borders of the micro-patterned extracellular matrix, which can restrict normal growth and differentiation. Therefore, a cell manipulation tool is needed, which can achieve better control and positioning of single cells.

We have reached high trapping efficiency with PhC enhanced optical tweezers as described in Chapter 3. It inherits the versatility from conventional optical tweezers and improves the trapping force without compromising cell viability. Therefore, we will apply this technology to manipulate and to pattern hPSCs.

hPSCs are sensitive cells and require specific culturing conditions. Successful cell culturing and differentiation requires the cells to adhere to the substrate, while optical manipulation requires the opposite. Therefore, we use polystyrene and parylene-C to achieve a cell patterning procedure compatible with cell culture.

4.2 Cell Passage

In experimental preparation, hPSCs are cultured in an incubator with 5% CO_2 at 37°C before detached and separated by Versene or Accutase solution for 10 min at 37°C. Accutase is an active enzyme that dissolves almost all proteins on the plasma membrane and separates colonies into individual cells. Versene, on the other hand, is much milder than Accutase so that passaged cells are further filtered with a $40\mu m$ filter to remove large cell clusters. Part of the cells are re-plated for future experiments, and other individual cells are suspended in the buffer solution, which consists of mTeSR media, 1:1000 Rho-associated kinase (ROCK) Inhibitor and 1:100 HEPES. Cells are stored in ice and brought to the optical tweezers setup, and they will be resuspended in fresh buffer solution right before the experiment. The ROCK Inhibitor could enhance the survival of human pluripotent stem cells and diminish dissociation-induced apoptosis during the trapping experiment [88]. HEPES buffer solution has a superior buffering capacity in the pH range 7.2-7.4 and does not require a controlled gaseous atmosphere, so an addition of HEPES is used to keep the pH value in the trapping experiment [89].

4.3 Post-Coated Geltrex Method

Stem cells need an extracellular component to adhere to the bottom for culturing, and we choose commercialized Geltrex as the extracellular matrix. Although hPSCs typically grow and colonize on Geltrex coated surfaces, these surfaces are too sticky for the cells to be moved freely by optical forces. Consequently, the high optical intensity is needed which causes serious photodamage to the trapped cells. Therefore, we developed a method to overcome this challenge.

We first examined the necessity of tissue-culture (TC) treated surface and Geltrex for successful hPSC colonization. Fig. 4.1 shows cell culturing results on non-TC and TC Petri dishes after four days. For the non-TC Petri dishes (Fig. 4.1a), hPSCs can only be cultured on the pre-coated Geltrex surfaces. Adding Geltrex to the petri dish after placing the hPSCs did not result in colony formation. For the TC Petri dishes (Fig. 4.1b), either pre-coating the surfaces with Geltrex or adding it after placing the hPSCs resulted in successful cell differentiation and colony formation. The results show that pre-coating Geltrex is a prerequisite for the non-TC Petri dishes, but TC Petri dishes provide another option to culture the cells with post-adding Geltrex. Since the TC-treated surface is less sticky than a surface coated with Geltrex, a TC treated surface with Geltrex added after optical manipulation offers a more viable environment to pattern the hPSCs by allowing lower laser intensities and therefore less photodamage to cells under optical trapping.

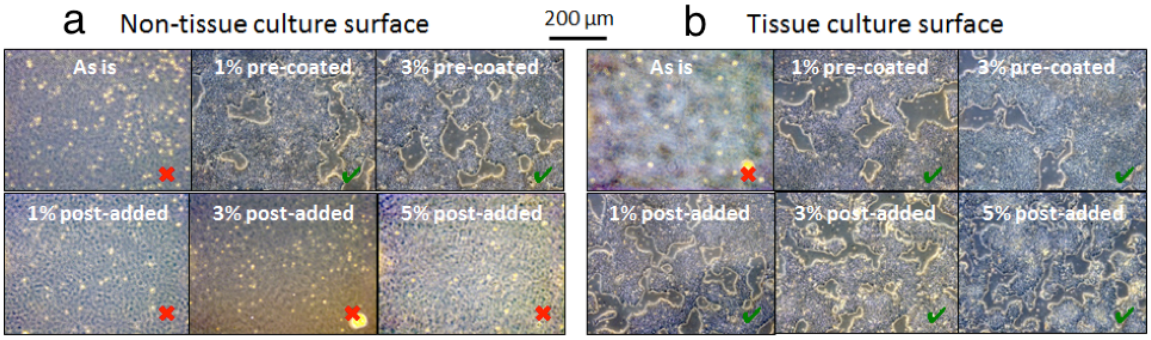

Figure 4.1. hPSC differentiation and colony formations under various conditions. (a) On non-tissue culture surfaces. (b) On tissue culture surfaces. For each case, the conditions are: as is (uncoated); pre-coating with 1% and 3% Geltrex before placing the hPSCs; adding 1%, 3% and 5% Geltrex after placing the hPSCs. On non-tissue culture surfaces, pre-coating with Geltrex is required for successful cell differentiation and colony formations, but this prevents moving the cells with optical tweezers freely. On tissue culture surfaces, either pre-coating or adding Geltrex after placing the cells can result in successful colony formations.

4.4 Materials for Tissue Culture Surface

4.4.1 Polystyrene

The surface for cell culture has evolved in the past 100 years from glass to plastic. The most of the currently commercialized vessels are manufactured from polystyrene because it is easy to mold. Also, polystyrene has high optical clarity, and it can be sterilized by irradiation to match different requirements. The freshly molded polystyrene vessels need to be treated with oxidation processes and the hydroxyl groups generated on the surface could promote cell culture [90] so that the surface becomes hydrophilic and allows cells to better attach to the surface. Therefore, polystyrene is now the most standard and commonly commercialized products for tissue-culturing Petri dishes, and the first experiment we describe in Section 4.5 is the cell patterning on commercial polystyrene Petri dish surface.

4.4.2 Parylene-C with Oxygen Plasma Treatment

Parylene-C is an alternative material for tissue-culture surface, and the oxygen plasma treated parylene-C surface has been demonstrated biological compatible [91]. The $2\mu m$-thick parylene-C coated substrate with oxygen plasma treatment is utilized to explore the hydrophobicity of the substrate that works best in the trapping experiment.

The parylene is a hydrophobic film which could reduce cell adsorption on the surface and is suitable for cell manipulation by optical tweezers. However, the possibility of cell colonization decreases once the surface becomes hydrophobic due to the poor adhesion to the surfaces. With oxygen plasma treatment, the parylene becomes hydrophilic and better for cell attachment. The parylene films were evaporated on a silicon chip and underwent oxygen plasma treatment for 30 seconds with different power. In the hydrophilicity measurement for various oxygen plasma treated surface, a goniometer system is utilized to detect the contact angle of water automatically. The contact angles in Fig. 4.2a decrease along with higher plasma power from 0W to 100W. Fig. 4.2b shows the relation between contact angle and the power of the oxygen plasma. The parylene surfaces are very hydrophobic with plasma power less than 20W, and the hydrophilicity has a huge variance after the treatment due to the low plasma power and short treatment time. When the power of the plasma exceeds 20W, the surface hydrophilicity becomes less sensitive to the plasma power and the surface becomes hydrophilic which is suitable for cell colonization.

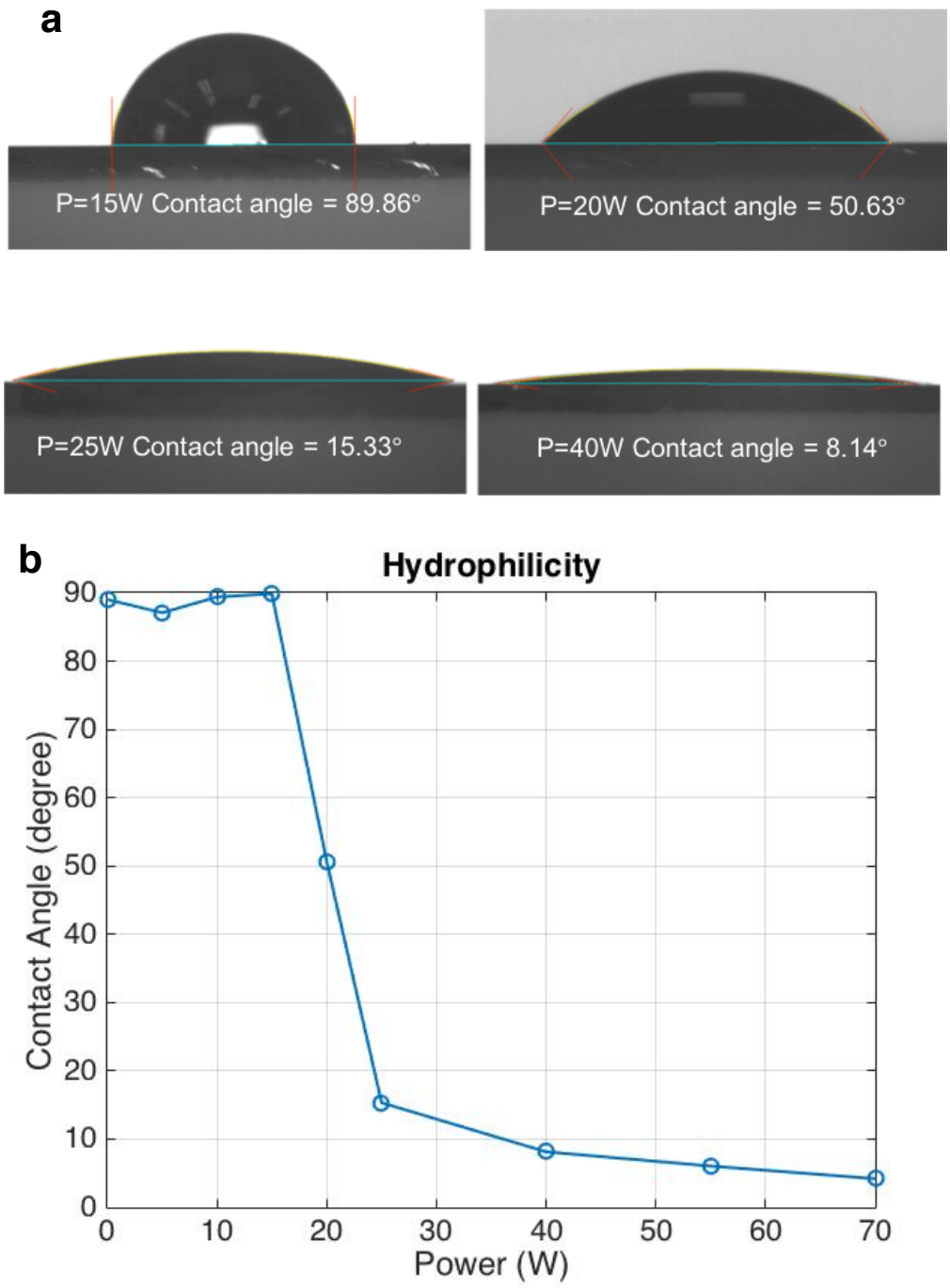

Figure 4.2 Contact angle with different oxygen plasma treatment after 30 seconds. (a) diagrams of contact angle measurements by the goniometer. (b) the contact angle for various plasma power. The parylene-C without oxygen plasma has 90º contact angle with water. Once the oxygen plasma power exceeds 15W 30 seconds, the contact angle begins to decrease which refers to a higher hydrophilicity. The hydrophilicity of the surface becomes less sensitive to the plasma power when it is greater than 40W.

Cells were plated on glass chips coated with treated parylene layer and were cultured for a few days using post-coated Geltrex methods. In Fig. 4.3, it shows cell culture results with 15W, 20W, 30W, 45W, 55W, and 70W plasma power on different days. On the first day of cell culture in Fig. 4.3a, all surfaces have cells attached on, but the surface underwent 15W plasma treatment supports fewer cells than others. Fig. 4.3b is the cell culture results on the third day and cells have formed colonies on all surfaces except for the 15W plasma treated surface. The cell colonies grow at different rates on the following days, and the surfaces with higher plasma power treatment have higher growth rate. Fig. 4.3c is the culturing results on the sixth day. The surface with 15W plasma treatment has no colony, while the colonies on the 70W plasma treated surface are almost confluent.

The cultured cells are further passaged with Accutase on the seventh day and counted by CASY Cell Counter (OMNI Life Science). The average cell density on glass chips is calculated, as shown in Fig. 4.3d. Each of the power consists of only two data point (n=2) and the large error in high plasma power is caused by this small number of datasets. In general, the average cell density increases on the parylene films with higher plasma power, which refers to a better biocompatible surface for cell culture. Therefore, the higher oxygen plasma power in the treatment provides the better surface that cells can survive and colonize on, and the 20W can be thought as the threshold to culture stem cells. To reduce the photodamage to cells during manipulation, we will use the 20W oxygen plasma treated parylene-C film in the later experiments.

a

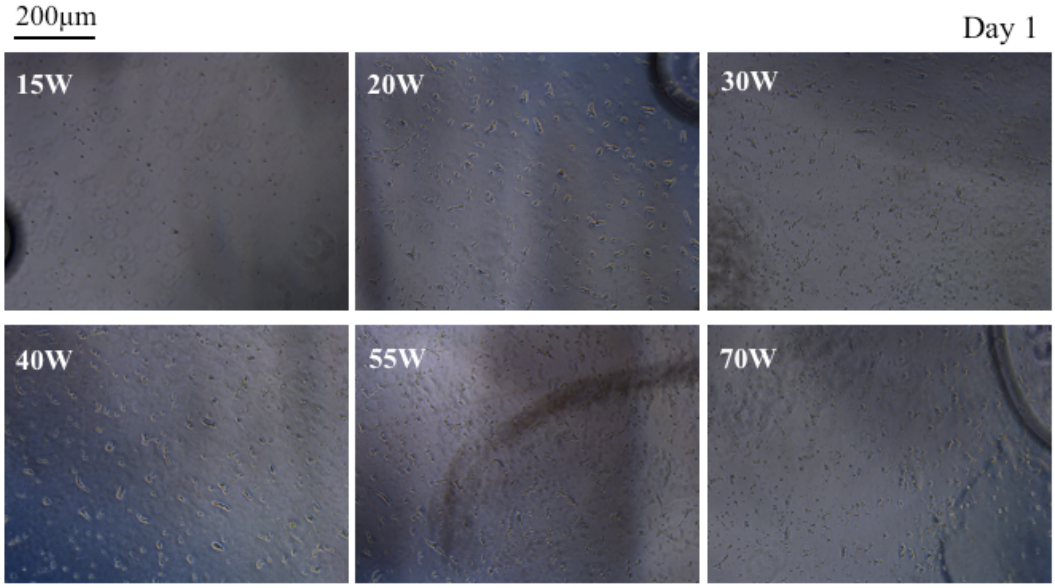
200μm
Day 1
15W
20W
30W
40W
55W
70W

b

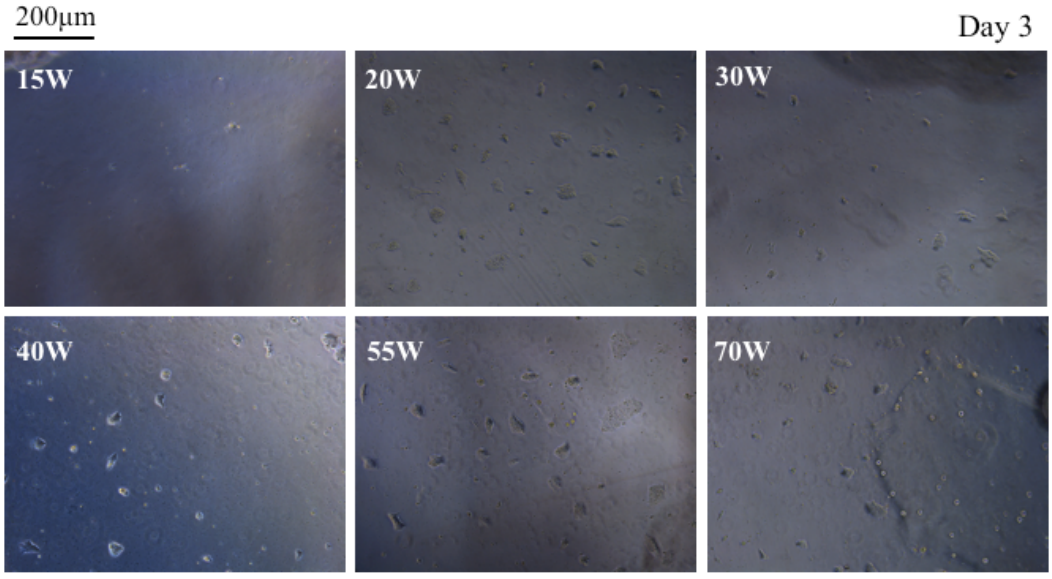
200μm
Day 3
15W
20W
30W
40W
55W
70W

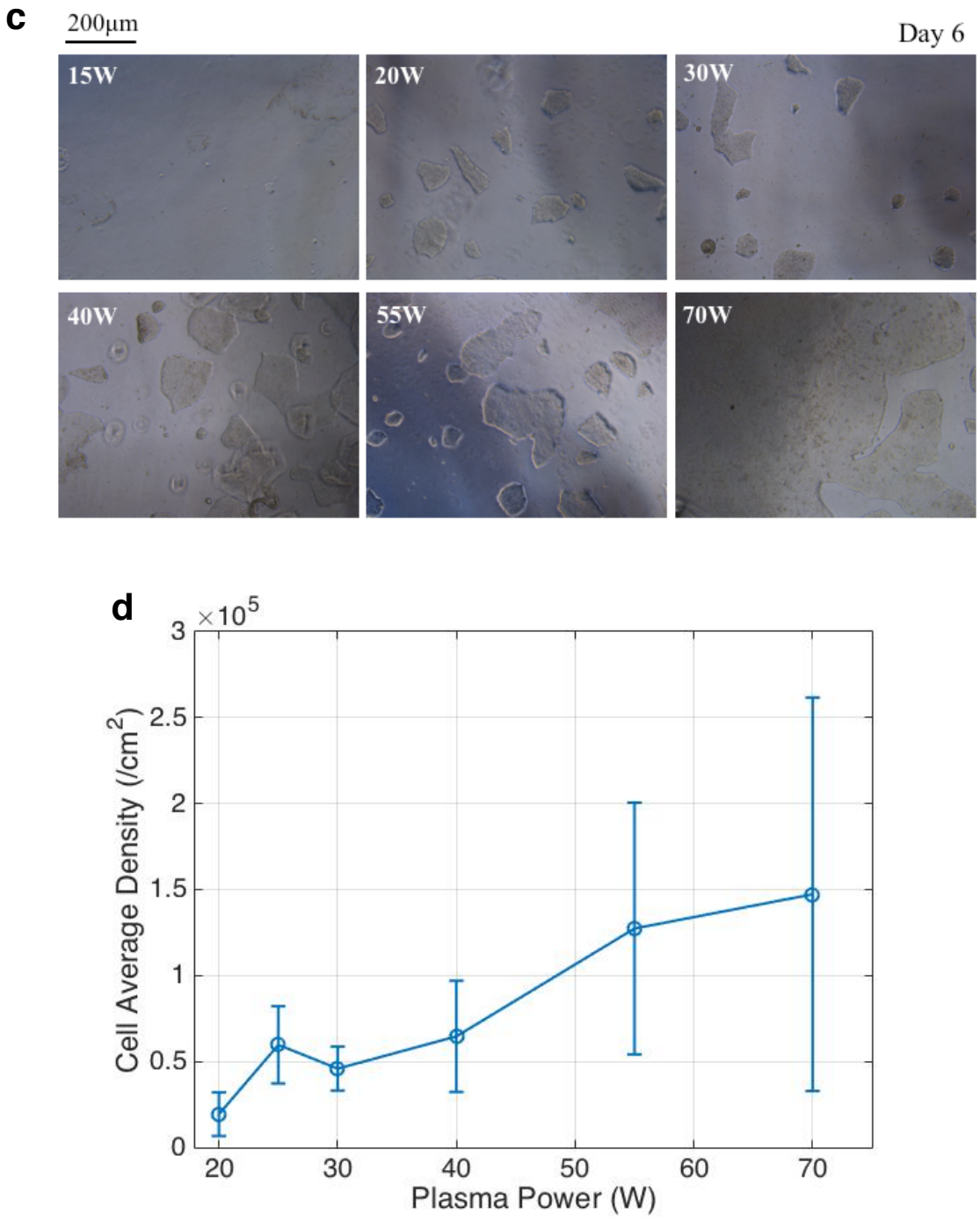

Figure 4.3 hPSC growth on the oxygen plasma treated parylene surface in a few days. The plasma time is 30 seconds. (a) after one day (b) after three days (c) after six days (d) cell count with CASY cell counter on the seventh day. There are more cells on the more hydrophilic surface and power above 20W is good enough for cell colonization. Therefore, the 20W plasma treatment is the threshold to colonize cells.

4.5 Cell Patterning

4.5.1 Experimental Setup

The experiment setup is shown in Fig. 4.4 which is utilized for optical manipulation and patterning of hPSCs. The culture plate is placed on a thermal-electric heater for cell attachment after optical manipulation. A SLM is inserted in the optical path to modulate a 1064 nm Nd:YVO_4 laser. The laser is directed to a 20x/50x (N.A.=0.22/0.55) objective lens through a dichroic filter and a beam splitter and focused on the sample.

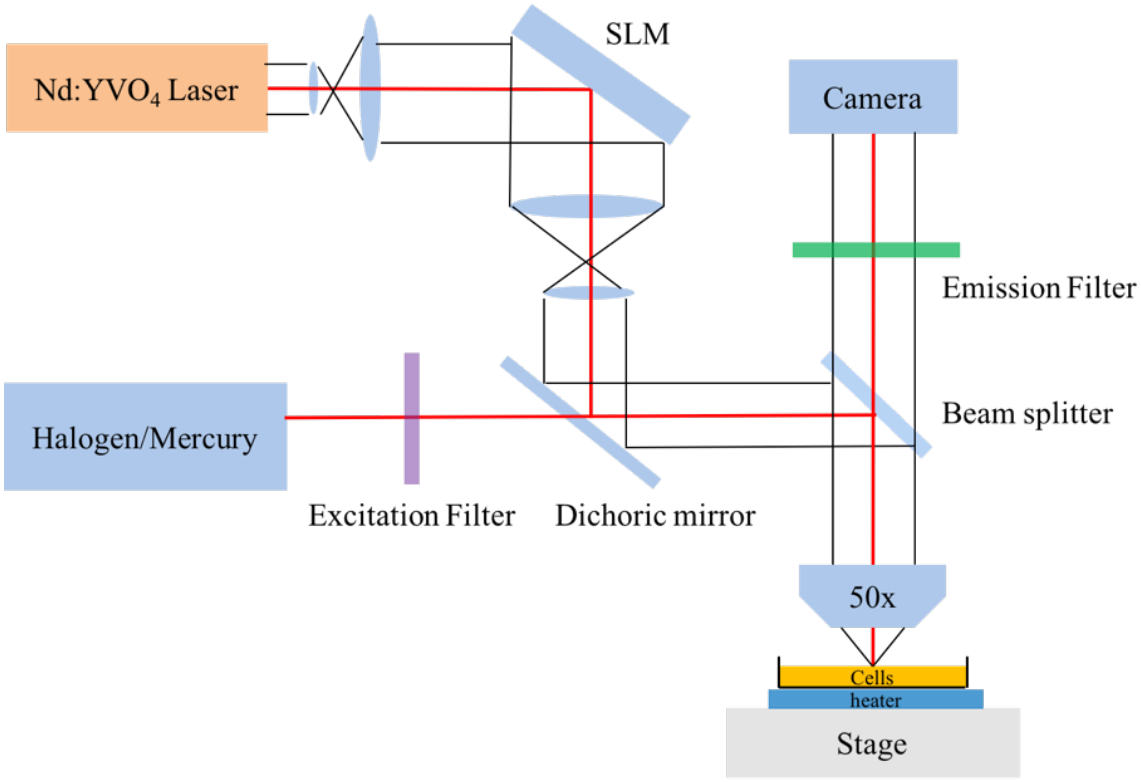

Figure 4.4 Schematic drawing of the experimental setup for optical manipulation of hPSCs

During the optical manipulation experiments, stem cells are kept in a mixture of 3mL culturing media mTeSR^{TM}1, 1:1000 Rock inhibitor and 1:100 HEPES buffer in the 60mm sterilized Petri dish. The experiments are operated outside the incubator and the HEPES

buffer is used to control pH-value of the media. The Geltrex will be added to the medium after cell patterning, and the electric heater plate under the Petri dish will be powered up. The electric heater is utilized to heat the medium up to 37 ºC to help cells attach to the bottom surface and spread out. The Petri dish will be moved to the incubator for cell culture when cells have firmly adhered to the surface.

4.5.2 Patterning hPSCs on Polystyrene

The patterning experiments are first conducted on the commercialized tissue-culture Petri dish as shown in Fig. 4.5. Cells are movable with low laser intensity at the beginning of the experiments. However, they grow junctions onto the tissue-culture surface and become adhesive after ten minutes, so it is only possible to make simple patterns with a few cells. Therefore, the polystyrene is still not ideal for post-coated Geltrex for manipulating stem cells, and an alternative material is necessary to be explored for the TC surface.

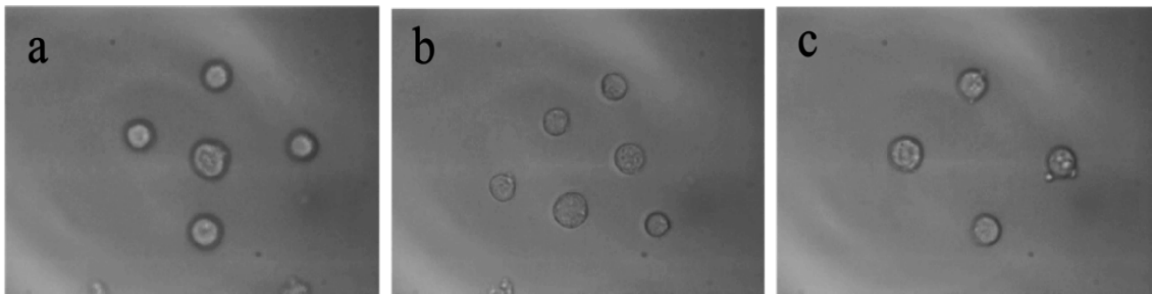

Figure 4.5 patterning individual hPSCs on a TC-treated plate at room temperature (a) cross (b) triangle (c) diamond patterns

4.5.3 Patterning hPSCs on Parylene-C

Since parylene-C with 20W oxygen plasma for 30 seconds provides the optimal platform to manipulate and culture stem cells with post-coated Geltrex, larger patterns are made on

the parylene film as shown in Fig. 4.6. The oxygen plasma treated parylene film allows a longer time to form stable cell junctions and provides longer time to manipulate cells with weak optical forces. Fig. 4.6a is a letter "R" pattern on the photonic crystal consisting of eight stem cells. All these cells adhere to the surface after adding Geltrex. Fig. 4.6b shows a cluster of more cells. They are all dragged to this field of view by the optical tweezers with low intensity before they get stuck to the film. Geltrex is added and mixed with the culture media after optical manipulation, and the Petri dish under the microscope is heated up to 37 ºC by the thermoelectric heater so that cells could bind to the parylene-C film and the extracellular matrix. Cells in Fig. 4.6c are initially patterned in a key shape on the 2D PhC. After 35 minutes heating at 37 ºC, some cells begin to spread out on the parylene-C film, which refers to cell attachment to the surface [90]. The firm cell-surface attachment allows moving the Petri dish to the incubator without destroying patterns for further cell culture. During the 35 minutes heating, cells may migrate and move to other places before spread out. For example, in the right image of Fig. 4.6c, the cell that is the tooth of the key does not spread out until moving out of the PhC region, and the two cells on the top and the bottom of the ring also migrate to places where are closer to other cells before spreading out. Fig. 4.6d is another pattern made above the PhC region, which have less cell moving during the 35 minutes heating after adding Geltrex. Cells also begin to spread out at 37 ºC, and this pattern has less cell migration and the pattern keeps the same shape.

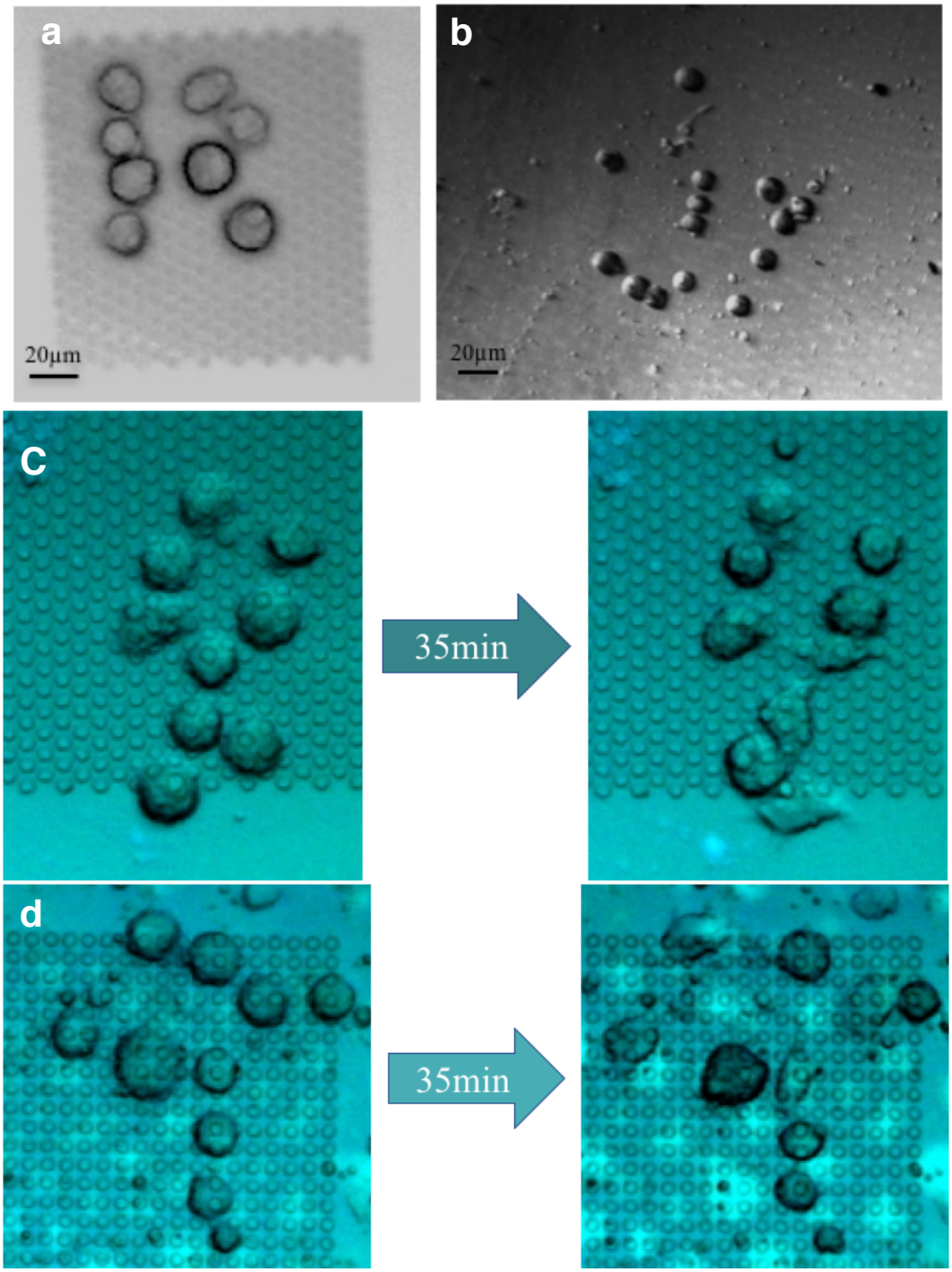

Figure 4.6 Larger patterns of hPSCs on parylene-C film (a) the letter "R" pattern in PhC region (b) large cluster of cells consisting of 15 cells (c) a key shape pattern in PhC region (left) and cell spreading after 35 minutes culturing after adding Geltrex (right) (d) a "π" shape pattern consisting of ten cells (left) and cell spreading after 35 minutes culturing after mixing Geltrex (right)

CHAPTER 5 CELLULAR REPULSIVE FORCE MEASUREMENT WITH OPTICAL TWEEZERS

5.1 Motivation

The human urinary system consists of kidneys, ureters, urinary bladder, and urethra, which produces urine and operating urinary filtration. The nephrons, as subunits of the kidney, has a fixed number and the reduction in nephron number causes a decrease in glomerular filtration and chronic kidney disease, which is affecting two million people worldwide. The limited availability and efficacy are prompting interest in new therapeutic strategies with the goal of generating new kidney tissues for transplantation [92-95].

Podocytes are cells wrapping around capillaries of the glomerulus in the kidneys. The foot processes of the podocytes are linked together by a specialized junction, or slit diaphragms, around the glomerular capillaries, which helps filter the small molecules such as water and salts in the blood [96-98]. Destruction of these slit diaphragms structures can result in defective urine production [99-101]. Podocalyxin (PODXL) is thought to play an essential role in the formation and maintenance of the foot processes, and its absence fails glomerular filtration. The structure of PODXL is shown in Fig. 5.1 [102]. PODXL is highly negatively charged, and the neutralization of its charge will destruct the foot process architecture and the slit diaphragms.

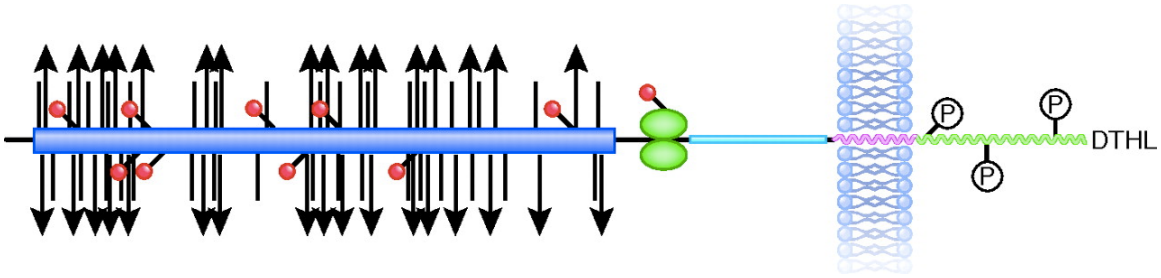

Figure 5.1 structure of podocalyxin. The dark vertical lines are O-glycosylated and the triangles at the end of the dark lines are sialylated. The purple rod is extracellular mucin domain with N-glycosylation as red circles. It is connected to the green intracellular domain, putative phosphorylation sites, and a C-terminal DTHL sequence for interaction with PDZ domains [102].

Human pluripotent stem cells (hPSCs) are providing a renewable source of diverse cells and tissues for laboratory studies and regeneration [103, 104]. hPSCs include both embryonic stem cells derived from embryos and induced pluripotent stem cells reprogrammed from adult cells. Recently, people are generating kidney tissues from hPSCs which provide new resources for modeling human kidney disease and regeneration [105-107]. Gene-edited hPSCs lacking PODXL (PODXL$^{-/-}$) have defective junctions and podocyte adhesion, providing the first evidence that hPSC-podocytes have potential to model disease [107]. However, quantitative comparison of hPSC-podocytes should be performed with PODXL$^{-/-}$ mutants and disease model.

There are many technologies developed to measure attachment forces or adhesion forces of cells, including atomic force microscope (AFM), magnetic tweezers, culture force monitor (CFM), optical tweezers and so on [32, 108-113]. These methods are used to characterize single ligand-receptor systems through their energy landscape and kinetic parameters. Micropipette techniques were used to test adhesion of reconstituted model systems such as giant vesicles; together with microplates, they were used to study the

mechanical and adhesive properties of single cells on substrates or to study cell-cell adhesion in the single-cell and single-molecular level.

Cell junctions are widely known as the structure within the tissue of multicellular organisms and the multiprotein complexes are formed between adjacent cells or between the cell and the extracellular matrix. The junction formation between cells depends on the interaction process before cell adhesion. Therefore, the cell interacting forces before cell adhesion is more significant in junction formation and their relevance to the molecular mechanism are not yet clear.

The hydrophobic surface property of parylene-C provides a frictionless platform integrated with optical tweezers to manipulate adherent cell, such as hPSCs, and directly gauge the biomechanics of cells at the single-cell level. We proposed and demonstrated a method to measure the interaction between a pair of cells before their attachment with this platform. Specifically speaking, this system is utilized to performed the experiments on hPSC-podocytes, including cells with PODXL and the PODXL$^{-/-}$ mutant cells. This method demonstrates the functionality of PODXL and measured repulsive forces between cells before their adhesion. Furthermore, it reveals the relevance between the forces and the gaps between cells.

5.2 Experimental Setup

The experimental setup is like the one in Section 4.5.1 with the same buffer solution. To maintain the PODXL protein on the plasma membranes, Versene is used to passage hPSCs. In the force measuring procedures, two spherical cells are suspended in a plastic sterilized Petri dish, which is coated with a parylene-C film without any oxygen plasma

treatment. The parylene-C film reduces the protein adsorption and cell adhesion due to its hydrophilic property. Although cells sink to the bottom surface quickly, the friction force is less than 0.3pN, which is only 5% of the trapping force and could be ignorable in the calculation of repulsive forces. The Petri dish is placed under the objective lens, and a pair of cells are moved close together within a distance about 3 μm by the optical tweezers. Before the laser is turned on, the position of the laser center is placed in the middle of cells. The trapping force, the repelling forces, and the spacing between the two cells can be measured when the laser is turned on. The statistical measurement is performed to characterize the force distribution and the relation between gaps and forces using this method.

5.3 Repulsive Force Between Cells

The boundary of stem cells is identified using fluorescent dye staining shown in Fig. 5.2. hPSCs are passaged with Versene, and individual cells are achieved with a 40μm filter. The cells are then suspended in the mTeSR media in a 15mL Falcon tube with 1:1000 ROCK Inhibitor, 1:100 HEPES buffer and 2% Calcium, AM cell-permeant (CAM) dye at the room temperature. The CAM dye penetrates the cytoplasm of cells and emits fluorescence due to the metabolism inside the cells. After 30 minutes staining, cells are centrifuged at 1000 rpm/s for 4 minutes. The buffer is then aspirated from the 15mL, and the cell pellet remains in the tube. Stem cells are resuspended in 1mL fresh mTeSR media with 1:1000 ROCK Inhibitor, 1:100 HEPES buffer, but without the fluorescent CAM dye. The last image in Fig. 5.2 is a stem cell under the microscope on the left and the fluorescence image with mercury lamp illumination on the right. The region of

fluorescent dye is the same as the size of the cell under the microscope, which demonstrates that the plasma membranes define the boundary of cells and there is no substance around the membrane in the experiment.

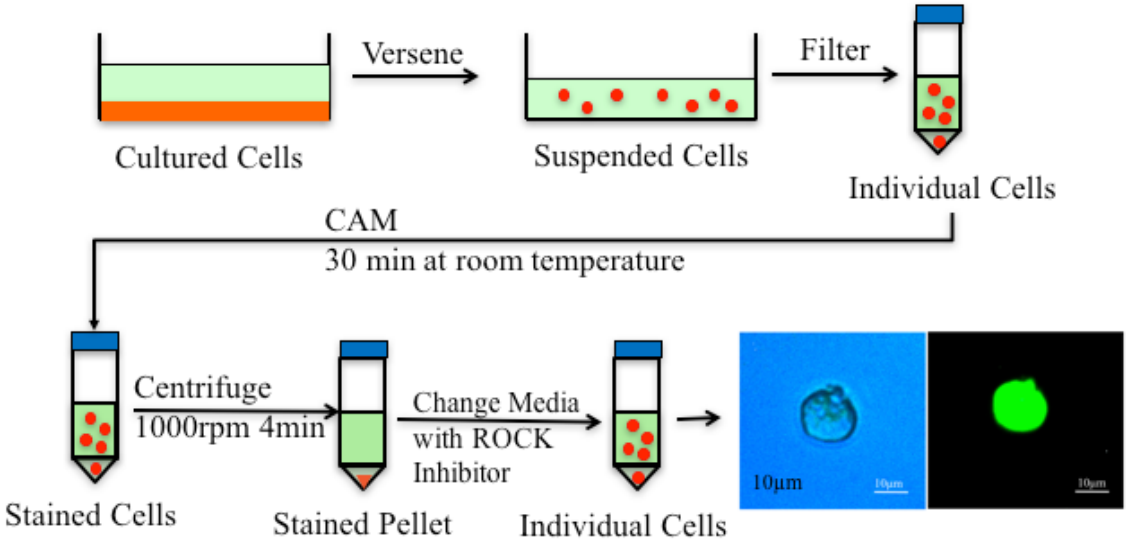

Figure 5.2 Procedures to stain hPSCs with Calcium, AM (CAM) dye. Cells are passaged with Versene and filtered with 40μm filter. Cells are then mixed with CAM dye at room temperature for 30 minutes and resuspended in the culture media with ROCK Inhibitor and HEPES. The final images show the microscopy image of a single stem cell (left) and fluorescence image of the stem cell under mercury lamp illumination (right), which shows no stained substance around cell membranes and its boundary can be defined as the enclosed dark line in the regular microscopy image

The forces between individual suspended cells are first characterized with wild type hPSC-podocyte cells. Fig. 5.3a is the schematic diagram of the setup. Two single cells are suspended and dragged close to each other. The laser is then placed in the middle of the cells before it is turned on. After the laser is on, both of the cells are attracted to the center of the laser while they also repel each other. The repelling force prevents cells getting in touch, and the cells will finally move to equilibrium positions and the distance between two cells can be measured. The repelling force is calculated by the trapping

force at the corresponding distance between the laser and the cell because of the equilibrium condition. Fig. 5.3b shows the gap change between cells with different laser intensity illumination. The laser power is initially low as $83\mu W/\mu m^2$ and the separation between cells becomes narrower after laser intensity is increased to $223\mu W/\mu m^2$. When the laser is changed to low laser power again, the two cells push each other away and return to a larger gap.

In Fig. 5.3c, cells are stained with fluorescent CAM dye, and a pair of cells are trapped in the same way as described in Fig. 5.3a. Besides the green fluorescence light inside the cell plasma membranes, there is dim green evanescent light outside the membranes, and the illumination decays very fast. This phenomenon is also examined by attracting two cells together in the same way as in Fig. 5.3a. Most of the cells form a gap when they are getting close, but there are pairs of cells which will get in touch with each other regardless the evanescent light, which indicates that the green light outside cell membranes are the scattering light in the buffer solution, and there is no stainable substance around the cells. The formation of the gap under optical trapping and the automatic separation after turning off the laser prove the existence of the repelling force between the stem cells.

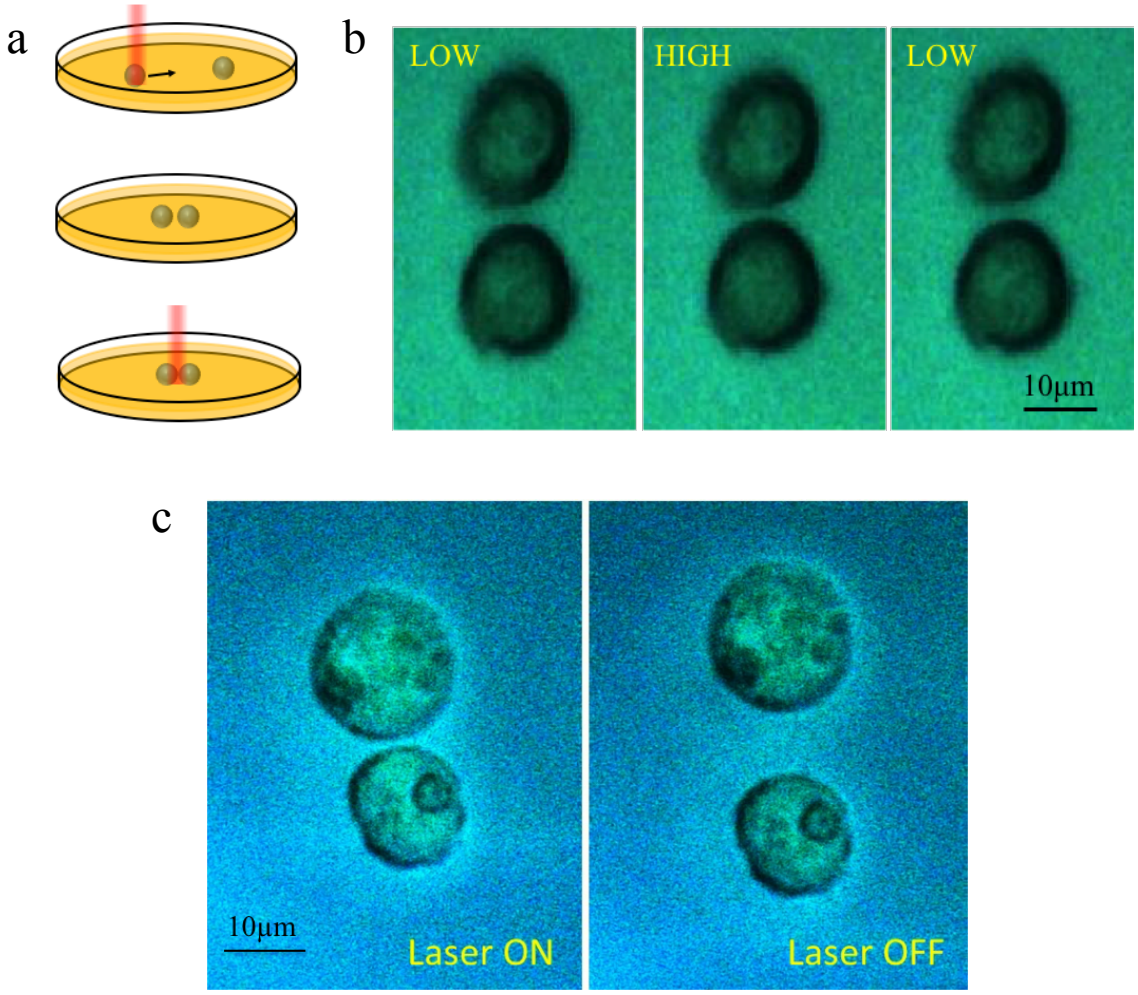

Figure 5.3 (a) schematic diagram of cell repelling force measurement (b) the gap between cells with and without the laser in the middle. The gap gets smaller when the laser intensity is as high as $223\mu W/\mu m^2$, and when the laser intensity is low $83\mu W/\mu m^2$, cells push each other away and then have a larger separation. (c) gap comparison after cell staining. The pair of cells has a gap when the laser is placed in the middle of the cells, and they push each other away automatically after the laser is turned off.

5.4 Trapping Force Calibration

The trapping force is characterized using Faxen's law described in Chapter 2, and the setup is shown in Fig. 5.4a. Before turned on, the laser is placed close to a single cell (~$3\mu m$) that is suspended in the buffer. The laser is turned on and attracts the cell to the center of the beam. With a high-speed camera, the position of the cell can be tracked by

post-image processing and tracking algorithms. The trapping forces can be calibrated by the velocity and the acceleration of the cell.

$$F = \frac{6\pi\eta R v}{1 - \frac{9}{16}\left(\frac{R}{h}\right) + \frac{1}{8}\left(\frac{R}{h}\right)^3 - \frac{45}{256}\left(\frac{R}{h}\right)^4 - \frac{1}{16}\left(\frac{R}{h}\right)^5} + \frac{4}{3}\pi R^3 \rho a \tag{5.1}$$

where η is the viscosity of the media, R is the radius of the cell, ρ is the cell density, v is the velocity, h is the distance from the center of the cell to the surface and a is the acceleration of the cell movement.

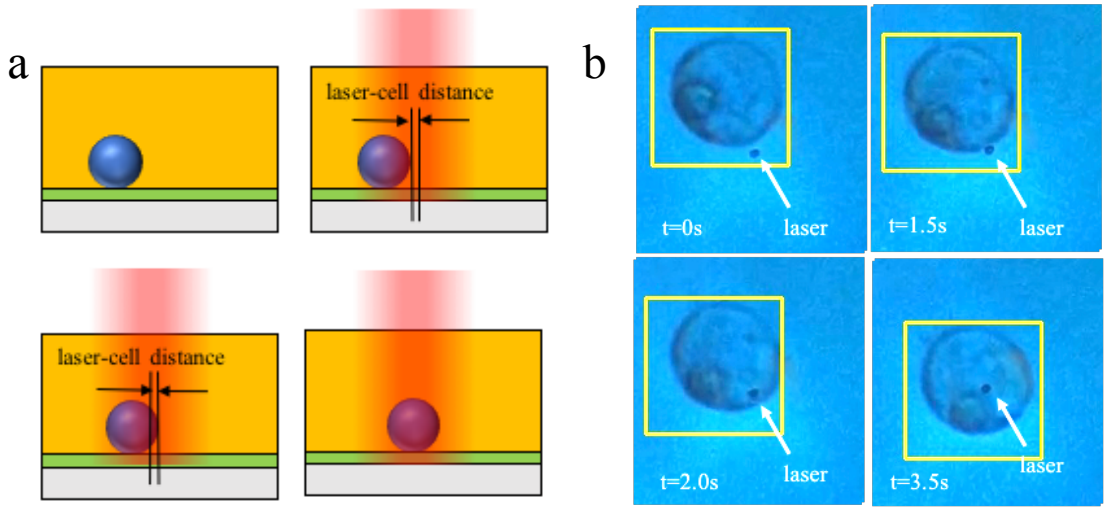

Figure 5.4 (a) schematic diagram of trapping force calibration (b) video sequence of trapping force calibration. The dark point at the center of each image is the laser. The laser is initially placed close to the cell, and the cell will be attracted to the center of the laser. The yellow box is automatically generated by mean-shift algorithm and is utilized to track the position of the moving cell in each video frame

Some frames in the calibration video are shown in sequence in Fig. 5.4b. The dark point at the center of each frame is the center of the laser. The cell is tracked automatically by post processing utilizing the mean-shift algorithm [114]. A yellow box is generated by

the algorithm and follows the cell in each video frame. The position of the cell is calculated by the center of the yellow window.

The position of the cell is shown in Fig. 5.5a and Fig. 5.5b. X is the direction where the cell is moving towards, and it is calculated and determined by the Principle Component Analysis (PCA). Y is the direction which is orthogonal to the moving direction, so the cell moves randomly in the Y direction as shown in Fig. 5.5b. Therefore, the velocity and acceleration are calculated from the X direction shown in Fig. 5.5c. Through the calculation, the second term in Eq. (5.1) is about six orders less than the first term, which matches the assumption of Faxen's law and demonstrates that the viscosity force dominates in this trapping force calibration. The red lines in Fig. 5.5 a-c are moving average smoothing based on the measured data, which indicates the trends of the positions and velocity.

Fig. 5.5d shows the calibrated force regarding the distance between the laser center and the front edge of the cell with $1.037 mW/\mu m^2$ laser intensity. The laser-cell distance in Fig. 5.5d is measured from the center of the laser to the front edge of the cell (Fig. 5.4a). When the cell is outside the trap, the laser-cell distance is labeled as a negative value, and the distance becomes positive after it is attracted into the trap. Before the cell enters the trap, the trapping force increases linearly with the distance and reaches the maximum trapping force when its front-edge just passes the laser center. The forces decrease once the cell enters the trap, and it becomes zero when the cell is placed at the center of the laser. The maximum force in this calibration is about 6 pN.

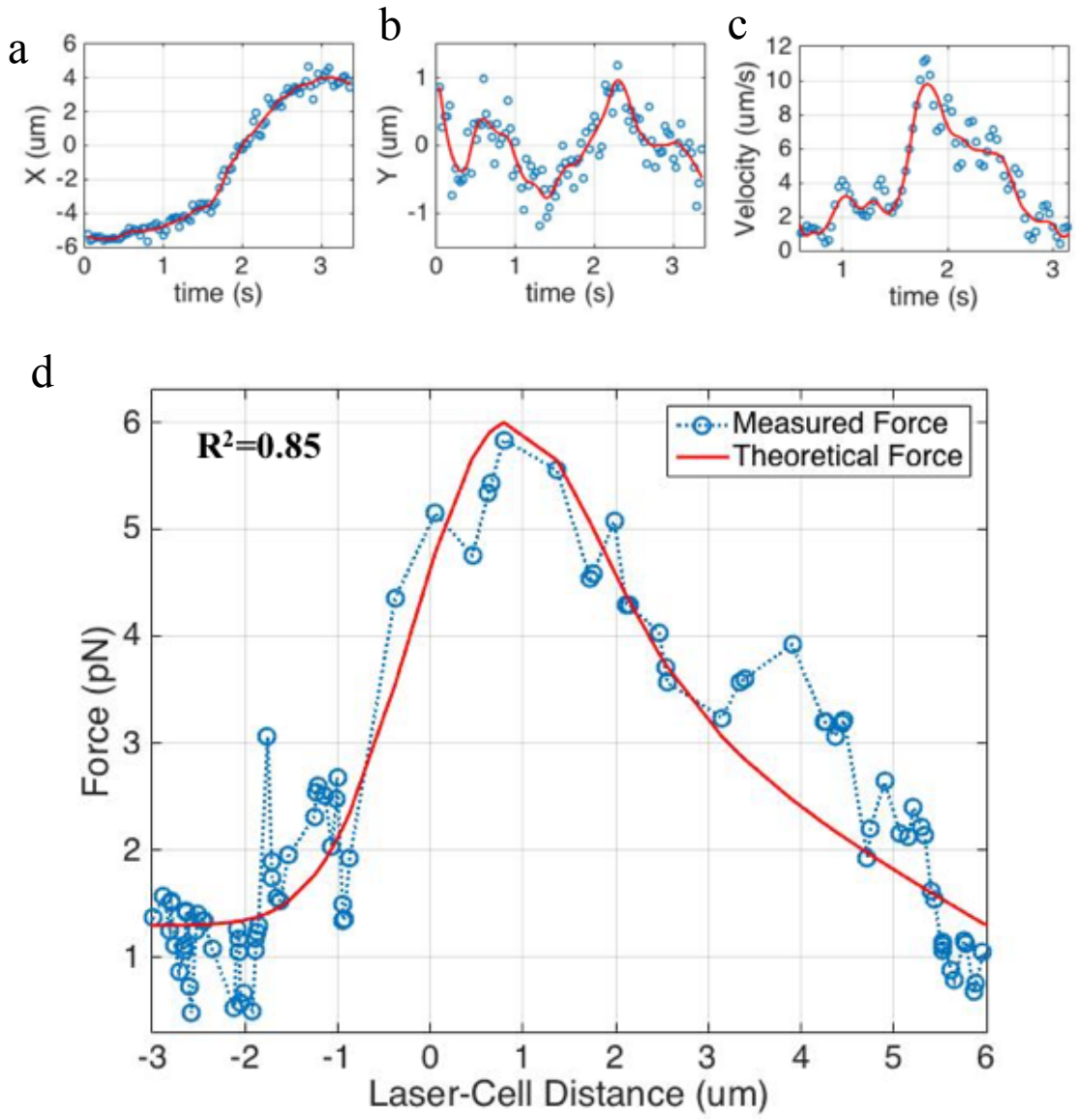

Figure 5.5 (a) X position of the cell. It is the direction along which the cell is attracted (b) Y position of the cell, which is orthogonal to the moving direction (c) velocity of the cell calculated for the X direction (d) trapping forces regarding the distance between the center of the laser and the front edge of the cell with $1.037 mW/\mu m^2$ laser intensity. The viscosity force in this calibration method dominates, and it is calculated by Faxen's law.

The red line in Fig. 5.5d is the theoretical trapping force computed with an optical tweezers computational toolbox [115]. This toolkit uses generalized Lorentz-Mie theory, and it provides accurate computation results for at most $11\mu m$ spherical particles in

Gaussian beam trapping. Therefore, the diameter of the particle is set to be $11\mu m$, the laser wavelength is 1064nm, and the refractive indices of the medium and the cell are 1.33 and 1.37. The measured force and computational force are fitted using linear regression, and the coefficient of determination R-square is 0.85.

5.5 Force Characterization between Pairs of Cells

The repulsive forces of the hPSCs with PODXL on the plasma membrane is characterized and shown in Fig. 5.6. The same pair of cells with different laser intensity is utilized to identify the relationship between gaps and repelling forces. The separations between cells are first measured, and the repulsive forces are calculated by the calibrated trapping force in Section 5.4. The blue circles in Fig. 5.6 are the measured gaps, and the forces are calculated by the methods described in Section 5.4. The red line in Fig. 5.6 is the linear fitting curve whose R-square value is 0.92. The relation between gaps and forces can be thought as linear in the range of $0.5\mu m$ - $2\mu m$ gap. The amplitude of the repelling forces is from 0.3pN – 3.6pN.

Moreover, the dotted gray lines in the plot are trapping forces with different laser intensity. The pair of cells will be attracted closer when the trapping force is higher than the repelling force. If the two cells are too close, on the other hand, the repelling force becomes greater than the trapping force and cells will get separated. Therefore, the equilibrium position of cells is at the intersection of the repelling force line and trapping force line with a given laser intensity, and the intersection represents the corresponding gap.

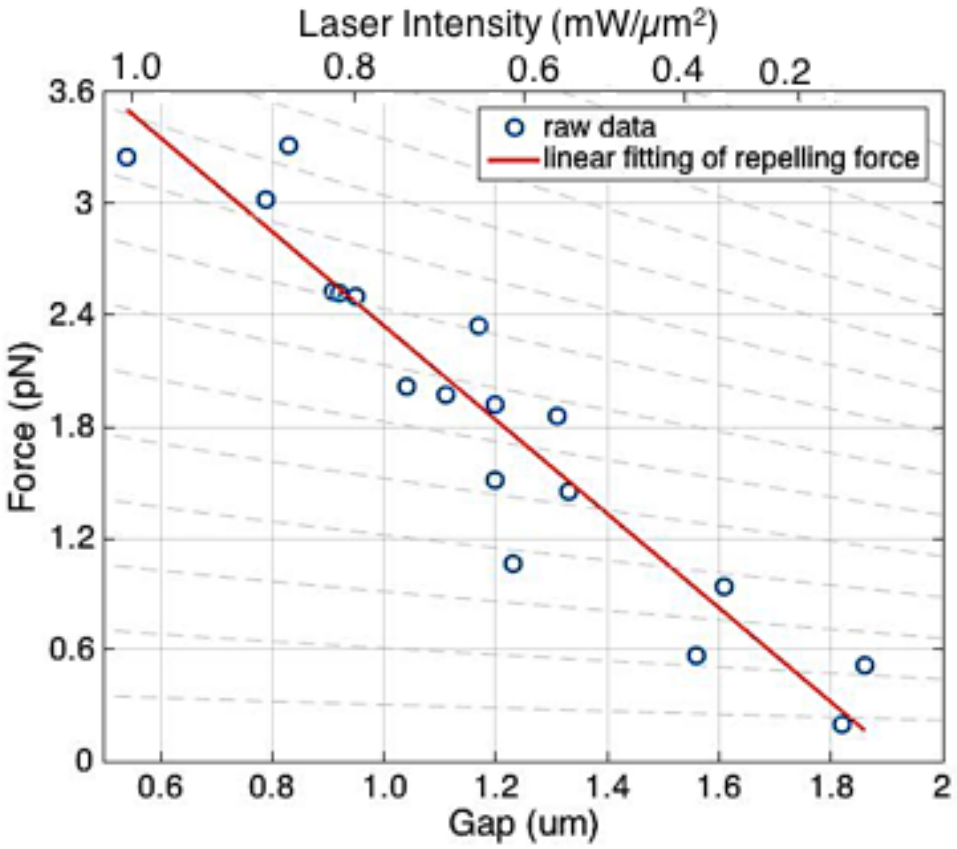

Figure 5.6 the relationship between repelling force and the separation between PODXL hPSCs. The blue circles are the measured data using different laser intensity on the same pairs of cells; the red curve is the fitting curve for the repelling force. The tilted dotted lines are laser trapping forces with different laser intensities. For example, given the laser intensity as 0.67 $mW/\mu m^2$, the intersection is the equilibrium position where the gap is 1.15 μm.

The laser intensity bar on the top of the plot provides a convenient way to find the expected gap. As shown in the plot, the higher laser intensity will make a smaller gap, because the higher intensity provides a greater trapping force, which is compensated by stronger repulsive force at equilibrium condition so that the separation between cells will be smaller. Once the laser power is given, the corresponding gap on the bottom bar is the expected gap. For example, the expected gap with 0.67 $mW/\mu m^2$ laser is 1.15 μm.

5.6 Force Distribution

Cells are not synchronized during their culturing the growth because they are in different states of the cell cycle. Therefore, the repelling forces and gaps vary among the various pairs of cells, even though they are from the same cell line and under the same laser intensity. In the characterization of the distribution of the cell interactions, the gaps and repelling forces are measured under the same laser intensity using the experimental procedures described in section 5.5. The distribution of the normalized forces is then characterized by more than fifty pairs of cells for the PODXL hPSCs. Fig. 5.7a and Fig. 5.7b shows the gap and force distribution under $0.67 mW/\mu m^2$ laser intensity. The intersection in Fig. 5.6 locates in the range of the peak bar in Fig. 5.7a.

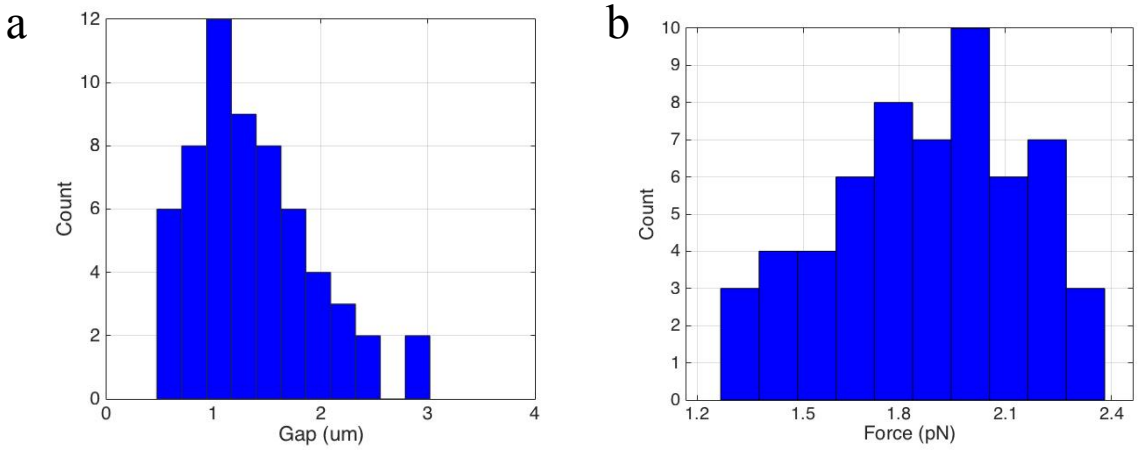

Figure 5.7 histograms of (a) gap (b) repelling force of stem cells. The intersection in Fig. 5.7 locates in the range of the peak bar in (a).

The red line in Fig. 5.6 could also change for different cell lines. The slope and position of the repulsive force define different gaps for these cells lines. The cells are more repulsive to each other if they have a larger gap in the same trapping intensity. In other

words, the intersection in Fig. 5.6 moves to the right with the same trapping force if the cell line is more repulsive. We measure two more hPSC cell lines with 0.373 $mW/\mu m^2$ laser intensity. One of them is the regular type of hPSCs, and the other cell line is the mutant hPSCs. The mutant cell line forms loosely connected tissue in the tissue culturing and formation of colonies, which indicates mutant cells have a higher repulsive effect. The gap and force distributions of the wild type cells are shown in Fig. 5.8a and Fig. 5.8b. The mutant cell line has larger gap and smaller measured forces under the same laser intensity in Fig. 5.8c and Fig. 5.8d, which shows a stronger repulsive effect and supports the tissue culturing results.

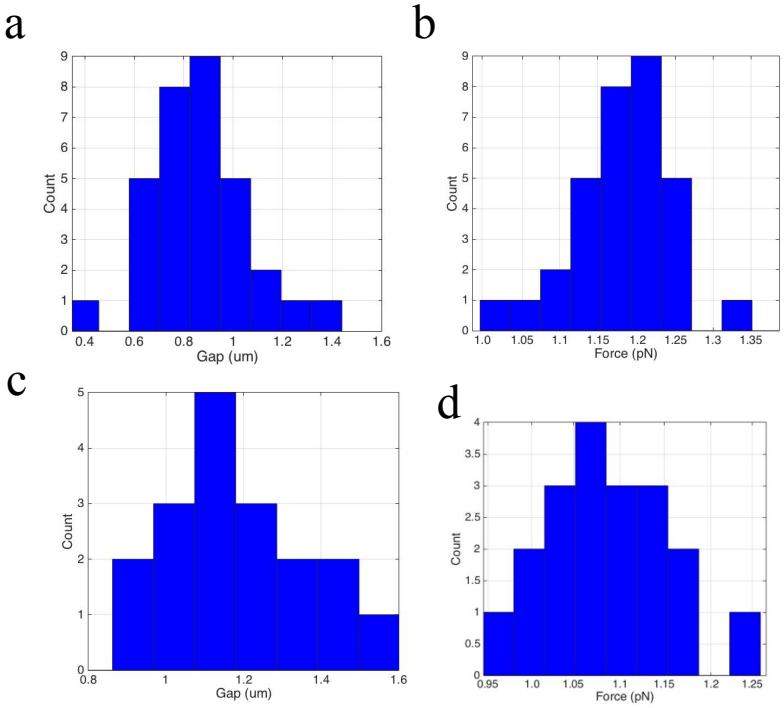

Figure 5.8 (a) gap (b) force distribution of wild type hPSCs with 0.373 $mW/\mu m^2$ laser trapping (c) gap (d) force distribution of cell line mutant hPSCs with 0.373 $mW/\mu m^2$ laser trapping

5.7 Change of Gaps during the Experiment

Besides the variety of cell spacing due to the asynchronization effect, separations also dynamically evolve because the measurement is conducted at the room temperature with limited control of pH value and humidity. The gap change over time is explored with the statistical data of one cell line presenting in Fig. 5.9. There are 58 data points from experiments on four different days, labeled with different colors. The time starts at the beginning of the experiments in each day, and the gaps are measured over time. The red line is the smoothed curve using moving average filter, and the black dotted line is the extension of the red line which represents the trend of the gaps before decreasing. It is shown that the average gap keeps the same in the first 40 minutes of the experiment and then begins to decrease linearly. The linear decreasing of gaps is caused by the change of pH-value and the death of cells. Although 1:100 HEPES is mixed with the buffer solution to keep the pH range at 7.2-7.4, the HEPES will be used up over time and the pH value of the media begin to change, which affects the double layer on the plasma membrane and the electrostatic forces between cells. Since cells are placed at room temperature without the control of humidity and pH, the plasma membrane and the proteins on the membrane will alter when cells are dying. Therefore, the measured gaps are only measured in the first 30-40 minutes before the change of experimental condition in the cell culture media.

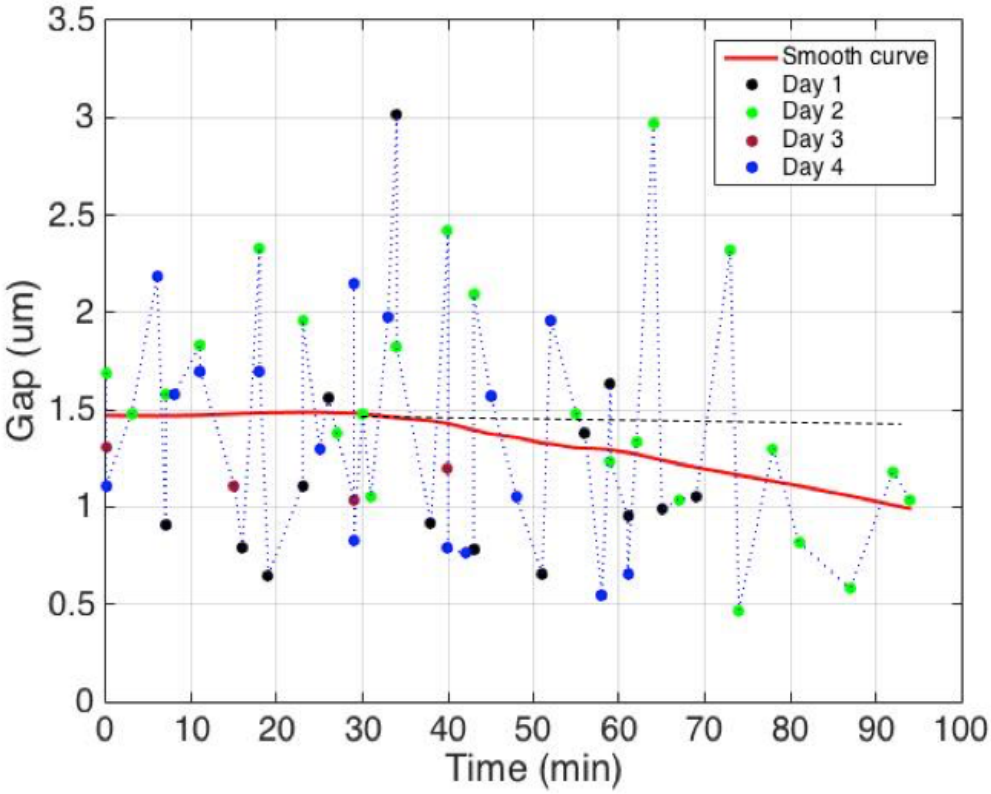

Figure 5.9 Dynamic change of gaps. The data are collected on four different days labeled with different colors and the time starts at zero in each day. The red line is the smooth curve using moving average filter that represents the trend of gaps over time. The gap keeps the same in the first 40 minutes before decreasing.

5.8 Comparison of Cell Lines

PODXL proteins is hypothesized to affect the gap between cells during formation of tissues. We experimented with wild type and mutant type hPSCs. The wild type cells are those containing PODXL on the plasma membranes, while the mutant type cells are gene-edited *PODXL*$^{-/-}$ hPSCs. Each of the types has three cell lines that underwent different pathways. We conducted gap measurements on the wild type and mutant type cells and demonstrated that PODXL proteins plays a significant role in podocyte's foot processes by increasing the repelling forces between cells. The comparison result is

shown in Fig. 5.10. The measurement using the same laser intensity 0.67 $mW/\mu m^2$ and the gaps of mutant cells (PODXL$^{-/-}$) are only about half of the separations of wild type cells (Control). The p-value calculated by two-sample students' t-test is only 2.13×10^{-10} between these two groups, which shows a significant difference between the control and mutant cells. This result supports the hypothesis that the PODXL protein on plasma membrane directly affects the junctional organization of podocytes by changing their surface adhesion.

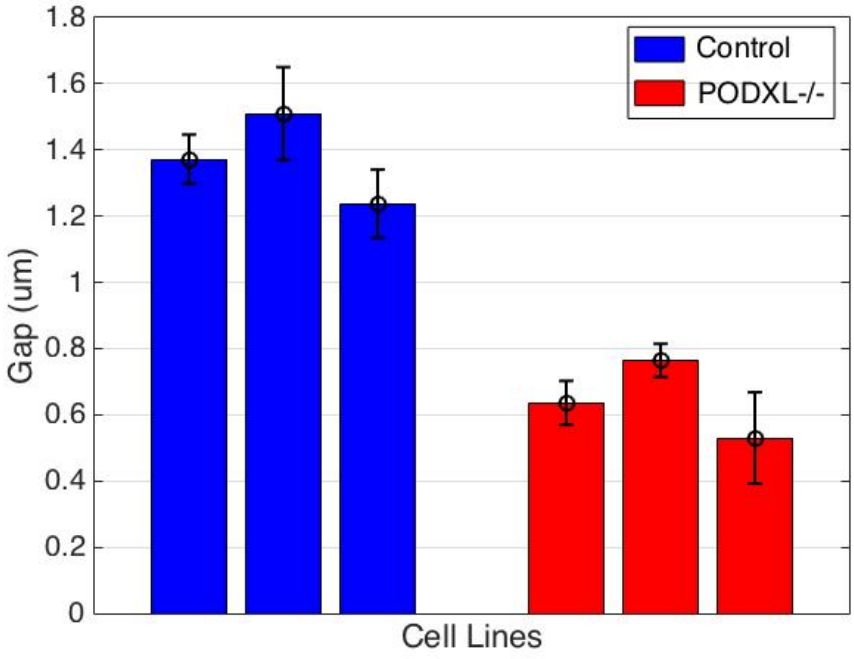

Figure 5.10 Gaps between pair of cells with standard error (black) for the cell with PODXL (blue) and lacking PODXL (red) on plasma membranes. Each group contains three cell lines with different pathway.

CHAPTER 6 CONCLUSION

In this dissertation, we have proposed and demonstrated 2D PhC enhanced optical tweezers, and its applications in the manipulation of biological cells and reducing photo-damage on live cells. The primary advantage of this method is its simplicity in fabrication and versatility in efficient trapping. The first part introduces the background of optical tweezers and state of the art technologies. These technologies improve the versatility of conventional optical tweezers, such as SLM and OET, or the trapping efficiency, such as plasmonics and PhC resonators. However, these technologies are not compatible with cell manipulation in their culture medium or limited by the fixed nanostructure and photodamage.

In Chapter 3 the optical force induced by diffraction in the far-field from the PhC structure is studied. Theoretical analysis and FDTD simulation show that such force can be used for enhancing optical trapping force and generate reconfigurable trapped pattern as well. Later we demonstrate the trapping efficiency in the experiments that particles can be trapped in the higher order of the diffraction patterns, although the trapping stiffness in the higher order diffraction is much less than the central trap. The central trap is an enhanced trapping. If the size of holes is designed in a certain range, the diffraction light will make a focus above the substrate which provides a more concentrated focus of light. This localized intensity distribution can be utilized to generate a higher trapping efficiency, resulting in an enhancement factor ~10. Moreover, the cell viability is characterized with bacteria and mammalian cells in the diffraction enhanced optical tweezers. The lifetime and sensitivity of cells are demonstrated to be the same under

conventional and enhanced optical tweezers with the same laser power. Since the sensitivity of cells is proportional to the laser power and the thermal generation is thought to be the primary factor of photo-damage, the photodamage can be reduced by decreasing the laser power while keeping the same trapping efficiency by the PhC enhanced optical tweezers.

In Chapter 4, a PhC enhanced optical tweezers system is developed for cell patterning and continue culturing cells after manipulation. To achieve this goal, we explored the biocompatible materials, such as polystyrene and parylene-C, for low-intensity optical manipulation. Although polystyrene is the most commonly used material in cell culture, only small patterns can be created due to cell-surface adhesion. Parylene-C with oxygen plasma treatment is an alternative material whose hydrophilicity can be controlled by plasma power, and the optimal oxygen plasma power is investigated for both optical manipulation and cell culture. Some patterning and culturing results are shown in the later part of this chapter. This system would promote the study of cell spatial patterning and differentiation in the early stage of tissue development at single-cell level.

In Chapter 5 we use optical tweezers to measure the repulsive forces between hPSC-podocyte and the mutant type and characterize the functionality of PODXL. PODXL is thought to be negatively charged and plays an essential role in the formation of foot processes. The hydrophobic surface is utilized in the experiment to minimize the cell adsorption and frictions and HEPES is added to the buffer to maintain the pH-value for cell viability. Experimental results show that the wild type podocytes hold a larger gap than the mutant type with the same trapping condition, which demonstrates the functionality of PODXL in producing and maintaining the slit diaphragms.

The research work in this dissertation demonstrates that PhC enhanced optical tweezers is a versatile tool to achieve manipulations for live cells with less photo-damage on the trapped cells. The simplicity in fabrication and flexibility through laser beam control is promising for a broad range of applications in micro-fluids and biological studies.

BIBILIOGRAPHY

1. Yablonovitch, E. and T.J. Gmitter, *Photonic band structure: The face-centered-cubic case.* Phys Rev Lett, 1989. **63**(18): p. 1950-1953.
2. Akahane, Y., et al., *High-Q photonic nanocavity in a two-dimensional photonic crystal.* Nature, 2003. **425**(6961): p. 944-7.
3. Majumdar, A., et al., *Electrical control of silicon photonic crystal cavity by graphene.* Nano Lett, 2013. **13**(2): p. 515-8.
4. Foresi, J.S., et al., *Photonic-bandgap microcavities in optical waveguides.* Nature, 1997. **390**(6656): p. 143-145.
5. Russell, P., *Photonic crystal fibers.* Science, 2003. **299**(5605): p. 358-362.
6. Mekis, A., et al., *High transmission through sharp bends in photonic crystal waveguides.* Physical Review Letters, 1996. **77**(18): p. 3787-3790.
7. Sakai, K., E. Miyai, and S. Noda, *Coupled-Wave Theory for Square-Lattice Photonic Crystal Lasers With TE Polarization.* Ieee Journal of Quantum Electronics, 2010. **46**(5): p. 788-795.
8. Miyai, E., et al., *Photonics: Lasers producing tailored beams.* Nature, 2006. **441**(7096): p. 946-946.
9. Liang, Y., et al., *Three-dimensional coupled-wave analysis for triangular-lattice photonic-crystal surface-emitting lasers with transverse-electric polarization.* Optics Express, 2013. **21**(1): p. 565-580.
10. Ashkin, A., J.M. Dziedzic, and T. Yamane, *Optical Trapping and Manipulation of Single Cells Using Infrared-Laser Beams.* Nature, 1987. **330**(6150): p. 769-771.
11. Ashkin, A. and J.M. Dziedzic, *Optical Trapping and Manipulation of Viruses and Bacteria.* Science, 1987. **235**(4795): p. 1517-1520.
12. Mandal, S., X. Serey, and D. Erickson, *Nanomanipulation Using Silicon Photonic Crystal Resonators.* Nano Letters, 2010. **10**(1): p. 99-104.
13. Chen, Y.F., et al., *Controlled Photonic Manipulation of Proteins and Other Nanomaterials.* Nano Letters, 2012. **12**(3): p. 1633-1637.
14. Wilson, B.K., et al., *Nanostructure-enhanced laser tweezers for efficient trapping and alignment of particles.* Optics Express, 2010. **18**(15): p. 16005-16013.
15. Prentice, P.A., et al., *Manipulation and filtration of low index particles with holographic Laguerre-Gaussian optical trap arrays.* Optics Express, 2004. **12**(4): p. 593-600.
16. Grier, D.G., *A revolution in optical manipulation.* Nature, 2003. **424**(6950): p. 810-816.
17. Harada, Y. and T. Asakura, *Radiation forces on a dielectric sphere in the Rayleigh scattering regime.* Optics Communications, 1996. **124**(5-6): p. 529-541.
18. Ashkin, A., et al., *Observation of a Single-Beam Gradient Force Optical Trap for Dielectric Particles.* Optics Letters, 1986. **11**(5): p. 288-290.
19. Zhang, H. and K.K. Liu, *Optical tweezers for single cells.* J R Soc Interface, 2008. **5**(24): p. 671-90.
20. Neuman, K.C. and S.M. Block, *Optical trapping.* Review of Scientific Instruments, 2004. **75**(9): p. 2787-2809.
21. Keen, S., et al., *Comparison of a high-speed camera and a quadrant detector for measuring displacements in optical tweezers.* Journal of Optics A: Pure and Applied Optics, 2007. **9**(8): p. S264-S266.
22. Neuman, K.C. and A. Nagy, *Single-molecule force spectroscopy: optical tweezers, magnetic tweezers and atomic force microscopy.* Nature Methods, 2008. **5**(6): p. 491-505.
23. Serey, X., et al., *DNA Transport and Delivery in Thermal Gradients near Optofluidic Resonators.* Physical Review Letters, 2012. **108**(4).

24. Born, M. and E. Wolf, *Principles of optics : electromagnetic theory of propagation, interference and diffraction of light*. 7th expanded ed. 1999, Cambridge ; New York: Cambridge University Press. xxxiii, 952 p.
25. Tuinier, R., *Approximate solutions to the Poisson–Boltzmann equation in spherical and cylindrical geometry.* J. Colloid Interface Sci., 2003. **258**(1): p. 45-49.
26. Butt, H.J., K. Graf, and M. Kappi, *Physics and Chemistry of Interfaces*. 2004: Wiley-VCH Verlag GmbH & Co. KGaA.
27. Russel, W.B., D.A. Saville, and W.R. Schowalter, *Colloidal dispersions*. Cambridge monographs on mechanics and applied mathematics. 1989, Cambridge ; New York: Cambridge University Press. xvii, 525 p., 1 leaf of plates.
28. Dobnikar, J., et al., *Three-body interactions in colloidal systems.* Physical Review E, 2004. **69**(3).
29. Gutsche, C., et al., *Forces between single pairs of charged colloids in aqueous salt solutions.* Physical Review E, 2007. **76**(3).
30. Ashkin, A., *Trapping of Atoms by Resonance Radiation Pressure.* Physical Review Letters, 1978. **40**(12): p. 729-732.
31. Block, S.M., *Making Light Work with Optical Tweezers.* Nature, 1992. **360**(6403): p. 493-495.
32. Litvinov, R.I., et al., *Binding strength and activation state of single fibrinogen-integrin pairs on living cells.* Proc Natl Acad Sci U S A, 2002. **99**(11): p. 7426-31.
33. Mammen, M., et al., *Optically controlled collisions of biological objects to evaluate potent polyvalent inhibitors of virus-cell adhesion.* Chemistry & Biology, 1996. **3**(9): p. 757-763.
34. Wang, M.D., et al., *Force and velocity measured for single molecules of RNA polymerase.* Science, 1998. **282**(5390): p. 902-907.
35. Herbert, K.M., et al., *Sequence-resolved detection of pausing by single RNA polymerase molecules.* Cell, 2006. **125**(6): p. 1083-94.
36. Neuman, K.C., et al., *Ubiquitous transcriptional pausing is independent of RNA polymerase backtracking.* Cell, 2003. **115**(4): p. 437-447.
37. Svoboda, K. and S.M. Block, *Force and Velocity Measured for Single Kinesin Molecules.* Cell, 1994. **77**(5): p. 773-784.
38. Block, S.M., L.S.B. Goldstein, and B.J. Schnapp, *Bead Movement by Single Kinesin Molecules Studied with Optical Tweezers.* Nature, 1990. **348**(6299): p. 348-352.
39. Svoboda, K., et al., *Direct Observation of Kinesin Stepping by Optical Trapping Interferometry.* Nature, 1993. **365**(6448): p. 721-727.
40. Neuman, K.C., et al., *Characterization of photodamage to Escherichia coli in optical traps.* Biophysical Journal, 1999. **77**(5): p. 2856-2863.
41. Curtis, J.E., B.A. Koss, and D.G. Grier, *Dynamic holographic optical tweezers.* Optics Communications, 2002. **207**(1-6): p. 169-175.
42. Juan, M.L., M. Righini, and R. Quidant, *Plasmon nano-optical tweezers.* Nature Photonics, 2011. **5**(6): p. 349-356.
43. Grigorenko, A.N., et al., *Nanometric optical tweezers based on nanostructured substrates.* Nature Photonics, 2008. **2**(6): p. 365-370.
44. Wang, K., et al., *Trapping and rotating nanoparticles using a plasmonic nano-tweezer with an integrated heat sink.* Nature Communications, 2011. **2**.
45. Miao, X.Y., et al., *Optical manipulation of micron/submicron sized particles and biomolecules through plasmonics.* Optics Express, 2008. **16**(18): p. 13517-13525.
46. Miao, X.Y. and L.Y. Lin, *Large dielectrophoresis force and torque induced by localized surface plasmon resonance of Au nanoparticle array.* Optics Letters, 2007. **32**(3): p. 295-297.

47. Miao, X. and Y.L. Lin. *New opto-plasmonic tweezers for manipulation and rotation of biological cells - design and fabrication*. in *Annual International Conference of the IEEE Engineering in Medicine and Biology Society*. 2006.
48. Miao, X.Y., B.K. Wilson, and L.Y. Lin, *Localized surface plasmon assisted microfluidic mixing.* Applied Physics Letters, 2008. **92**(12).
49. Miao, X.Y., et al., *Trapping and Rotation of Nanowires Assisted by Surface Plasmons.* Ieee Journal of Selected Topics in Quantum Electronics, 2009. **15**(5): p. 1515-1520.
50. Jaquay, E., et al., *Light-Assisted, Templated Self-Assembly Using a Photonic-Crystal Slab.* Nano Letters, 2013. **13**(5): p. 2290-2294.
51. Righini, M., et al., *Nano-optical Trapping of Rayleigh Particles and Escherichia coli Bacteria with Resonant Optical Antennas.* Nano Letters, 2009. **9**(10): p. 3387-3391.
52. Wu, M.C., *Optoelectronic tweezers.* Nature Photonics, 2011. **5**(6): p. 322-324.
53. Chiou, P.Y., A.T. Ohta, and M.C. Wu, *Massively parallel manipulation of single cells and microparticles using optical images.* Nature, 2005. **436**(7049): p. 370-372.
54. Yan, R.X., D. Gargas, and P.D. Yang, *Nanowire photonics.* Nature Photonics, 2009. **3**(10): p. 569-576.
55. Ohta, A.T., et al., *Dynamic cell and microparticle control via optoelectronic tweezers.* Journal of Microelectromechanical Systems, 2007. **16**(3): p. 491-499.
56. Ohta, A.T., et al., *Optically controlled cell discrimination and trapping using optoelectronic tweezers.* Ieee Journal of Selected Topics in Quantum Electronics, 2007. **13**(2): p. 235-243.
57. Jamshidi, A., et al., *Study of the dipole-dipole interaction between metallic nanowires trapped using optoelectronic tweezers (OET)*, in *Conference on Lasers and Electro-Optics*. 2008.
58. Jamshidi, A., et al., *Dynamic manipulation and separation of individual semiconducting and metallic nanowires.* Nature Photonics, 2008. **2**(2): p. 85-89.
59. Huang, K.W., et al., *Optoelectronic tweezers integrated with lensfree holographic microscopy for wide-field interactive cell and particle manipulation on a chip.* Lab Chip, 2013. **13**(12): p. 2278-84.
60. Pavlin, M., et al., *Effect of cell electroporation on the conductivity of a cell suspension.* Biophysical Journal, 2005. **88**(6): p. 4378-4390.
61. Burg, T.P., et al., *Weighing of biomolecules, single cells and single nanoparticles in fluid.* Nature, 2007. **446**(7139): p. 1066-1069.
62. Gupta, A., D. Akin, and R. Bashir, *Detection of bacterial cells and antibodies using surface micromachined thin silicon cantilever resonators.* Journal of Vacuum Science & Technology B, 2004. **22**(6): p. 2785-2791.
63. Park, K., et al., *'Living cantilever arrays' for characterization of mass of single live cells in fluids.* Lab on a Chip, 2008. **8**(7): p. 1034-1041.
64. Godin, M., et al., *Measuring the mass, density, and size of particles and cells using a suspended microchannel resonator.* Applied Physics Letters, 2007. **91**(12).
65. Park, K., et al., *Measurement of adherent cell mass and growth.* Proceedings of the National Academy of Sciences of the United States of America, 2010. **107**(48): p. 20691-20696.
66. Lee, J., et al., *Suspended microchannel resonators with piezoresistive sensors.* Lab on a Chip, 2011. **11**(4): p. 645-651.
67. Weng, Y.C., et al., *Mass sensors with mechanical traps for weighing single cells in different fluids.* Lab on a Chip, 2011. **11**(24): p. 4174-4180.
68. Keeler, E.G., et al., *MEMS resonator and photonic Crystal integration for enhanced cellular mass sensing*, in *Optics in the Life Sciences*. 2015, OSA: Vancouver, Canada.
69. Popescu, G., et al., *New technologies for measuring single cell mass.* Lab on a Chip, 2014. **14**(4): p. 646-652.

70. Huang, L., S.J. Maerkl, and O.J.F. Martin, *Integration of plasmonic trapping in a microfluidic environment.* Optics Express, 2009. **17**(8): p. 6018-6024.
71. Xie, C.G., et al., *Real-time Raman spectroscopy of optically trapped living cells and organelles.* Optics Express, 2004. **12**(25): p. 6208-6214.
72. Bustamante, C., Z. Bryant, and S.B. Smith, *Ten years of tension: single-molecule DNA mechanics.* Nature, 2003. **421**(6921): p. 423-427.
73. Mirsaidov, U., et al., *Optimal optical trap for bacterial viability.* Physical Review E, 2008. **78**(2).
74. Ericsson, M., et al., *Sorting out bacterial viability with optical tweezers.* Journal of Bacteriology, 2000. **182**(19): p. 5551-5555.
75. Jing, P.F., J.D. Wu, and L.Y. Lin, *Patterned Optical Trapping with Two-Dimensional Photonic Crystals.* Acs Photonics, 2014. **1**(5): p. 398-402.
76. Jing, P.F., et al., *Photonic Crystal Optical Tweezers with High Efficiency for Live Biological Samples and Viability Characterization.* Scientific Reports, 2016. **6**.
77. Oskooi, A.F., et al., *MEEP: A flexible free-software package for electromagnetic simulations by the FDTD method.* Computer Physics Communications, 2010. **181**(3): p. 687-702.
78. Wang, Z.B., et al., *Optical virtual imaging at 50 nm lateral resolution with a white-light nanoscope.* Nature Communications, 2011. **2**.
79. Chen, Z.G., A. Taflove, and V. Backman, *Photonic nanojet enhancement of backscattering of light by nanoparticles: a potential novel visible-light ultramicroscopy technique.* Optics Express, 2004. **12**(7): p. 1214-1220.
80. Florescu, M., S. Torquato, and P.J. Steinhardt, *Designer disordered materials with large, complete photonic band gaps.* Proceedings of the National Academy of Sciences of the United States of America, 2009. **106**(49): p. 20658-20663.
81. Milord, L., et al., *Engineering of slow Bloch modes for optical trapping.* Applied Physics Letters, 2015. **106**(12).
82. Krishan, A., *Rapid Flow Cytofluorometric Analysis of Mammalian-Cell Cycle by Propidium Iodide Staining.* Journal of Cell Biology, 1975. **66**(1): p. 188-193.
83. Coleman, M.L., et al., *Membrane blebbing during apoptosis results from caspase-mediated activation of ROCK I.* Nature Cell Biology, 2001. **3**(4): p. 339-345.
84. Jarzynski, C., *SINGLE-MOLECULE EXPERIMENTS Out of equilibrium.* Nature Physics, 2011. **7**(8): p. 591-592.
85. Shields, C.W., C.D. Reyes, and G.P. Lopez, *Microfluidic cell sorting: a review of the advances in the separation of cells from debulking to rare cell isolation.* Lab on a Chip, 2015. **15**(5): p. 1230-1249.
86. Warmflash, A., et al., *A method to recapitulate early embryonic spatial patterning in human embryonic stem cells.* Nature Methods, 2014. **11**(8): p. 847-854.
87. Ma, Z., et al., *Self-organizing human cardiac microchambers mediated by geometric confinement.* Nature Communications, 2015. **6**.
88. Watanabe, K., et al., *A ROCK inhibitor permits survival of dissociated human embryonic stem cells.* Nat Biotechnol, 2007. **25**(6): p. 681-6.
89. Good, N.E., et al., *Hydrogen ion buffers for biological research.* Biochemistry, 1966. **5**(2): p. 467-77.
90. Curtis, A.S., et al., *Adhesion of cells to polystyrene surfaces.* J Cell Biol, 1983. **97**(5 Pt 1): p. 1500-6.
91. Chang, T.Y., et al., *Cell and protein compatibility of parylene-C surfaces.* Langmuir, 2007. **23**(23): p. 11718-25.
92. Dekel, B., et al., *Human and porcine early kidney precursors as a new source for transplantation.* Nat Med, 2003. **9**(1): p. 53-60.

93. Xinaris, C., et al., *In vivo maturation of functional renal organoids formed from embryonic cell suspensions.* J Am Soc Nephrol, 2012. **23**(11): p. 1857-68.
94. Unbekandt, M. and J.A. Davies, *Dissociation of embryonic kidneys followed by reaggregation allows the formation of renal tissues.* Kidney Int, 2010. **77**(5): p. 407-16.
95. Rogers, S.A., et al., *Transplantation of developing metanephroi into adult rats.* Kidney Int, 1998. **54**(1): p. 27-37.
96. Reeves, W., J.P. Caulfield, and M.G. Farquhar, *Differentiation of epithelial foot processes and filtration slits: sequential appearance of occluding junctions, epithelial polyanion, and slit membranes in developing glomeruli.* Lab Invest, 1978. **39**(2): p. 90-100.
97. Hartleben, B., et al., *Neph-Nephrin proteins bind the Par3-Par6-atypical protein kinase C (aPKC) complex to regulate podocyte cell polarity.* J Biol Chem, 2008. **283**(34): p. 23033-8.
98. Reiser, J., et al., *The glomerular slit diaphragm is a modified adherens junction.* J Am Soc Nephrol, 2000. **11**(1): p. 1-8.
99. Doyonnas, R., et al., *Anuria, omphalocele, and perinatal lethality in mice lacking the CD34-related protein podocalyxin.* J Exp Med, 2001. **194**(1): p. 13-27.
100. Kestila, M., et al., *Positionally cloned gene for a novel glomerular protein--nephrin--is mutated in congenital nephrotic syndrome.* Mol Cell, 1998. **1**(4): p. 575-82.
101. Boute, N., et al., *NPHS2, encoding the glomerular protein podocin, is mutated in autosomal recessive steroid-resistant nephrotic syndrome.* Nat Genet, 2000. **24**(4): p. 349-54.
102. Nielsen, J.S. and K.M. McNagny, *The Role of Podocalyxin in Health and Disease.* Journal of the American Society of Nephrology, 2009. **20**(8): p. 1669-1676.
103. Thomson, J.A., et al., *Embryonic stem cell lines derived from human blastocysts.* Science, 1998. **282**(5391): p. 1145-7.
104. Takahashi, K., et al., *Induction of pluripotent stem cells from adult human fibroblasts by defined factors.* Cell, 2007. **131**(5): p. 861-72.
105. Taguchi, A., et al., *Redefining the in vivo origin of metanephric nephron progenitors enables generation of complex kidney structures from pluripotent stem cells.* Cell Stem Cell, 2014. **14**(1): p. 53-67.
106. Takasato, M., et al., *Kidney organoids from human iPS cells contain multiple lineages and model human nephrogenesis.* Nature, 2015. **526**(7574): p. 564-8.
107. Freedman, B.S., et al., *Modelling kidney disease with CRISPR-mutant kidney organoids derived from human pluripotent epiblast spheroids.* Nat Commun, 2015. **6**: p. 8715.
108. Prass, M., et al., *Direct measurement of the lamellipodial protrusive force in a migrating cell.* J Cell Biol, 2006. **174**(6): p. 767-72.
109. Gosse, C. and V. Croquette, *Magnetic tweezers: micromanipulation and force measurement at the molecular level.* Biophys J, 2002. **82**(6): p. 3314-29.
110. Eastwood, M., D.A. McGrouther, and R.A. Brown, *A culture force monitor for measurement of contraction forces generated in human dermal fibroblast cultures: evidence for cell-matrix mechanical signalling.* Biochim Biophys Acta, 1994. **1201**(2): p. 186-92.
111. Helenius, J., et al., *Single-cell force spectroscopy.* J Cell Sci, 2008. **121**(11): p. 1785-91.
112. Puech, P.H., et al., *A new technical approach to quantify cell-cell adhesion forces by AFM.* Ultramicroscopy, 2006. **106**(8-9): p. 637-44.
113. Thoumine, O., et al., *Short-term binding of fibroblasts to fibronectin: optical tweezers experiments and probabilistic analysis.* Eur Biophys J, 2000. **29**(6): p. 398-408.
114. Cheng, Y., *Mean shift, mode seeking, and clustering.* IEEE Transactions on Pattern Analysis and Machine Intelligence, 1995. **17**(8): p. 790 - 799.

115. Nieminen, T.A., et al., *Optical tweezers computational toolbox.* Journal of Optics a-Pure and Applied Optics, 2007. **9**(8): p. S196-S203.

APPENDIX

Photonic Crystal Diffraction Matlab Code

This code program consists of the main program "Main.m" and a function file named "propagation1d.m" to calculate the 2D intensity distribution with a give initial electric field. The diffraction is computed using Kirchhoff's Diffraction Theorem in the "propagation1d.m" function. Finally, the program will generate a 2D image to display the intensity distribution. The default initial electric filed is a finites sized window and it can be modified in the main program.

Main.m

```
% Main program
% calculate 2D light diffraction above a hole of a photonic crystal
% the light source could modulated by the initial electri field
clear;clc;clf;close all;

radius = 1.8e-6;  % radius is 1.5um
z = linspace(0.5e-6, 5e-6, 3e2);  % height is 0.5-2um
lambda = 1.064e-6;   % wavelength is 1064nm
k = 2 * pi /  lambda;
s = linspace(-5e-6,5e-6,1e3);  % source area
x = linspace(-5e-6,5e-6,1e3);   % detection area
n0 = 3.6;
n1 = 1;

% INITIALIZE ELECTRIC FIELD HERE %
fprintf('Calculating initial electric fields ... ');
E0 = zeros(1, length(s));
indx = find(abs(s) <= radius);
E0(indx) = 1;
fprintf('Complete.\n');
% INITIALIZE ELECTRIC FIELD END %

figure;
plot(s,abs(E0).^2);
title('Initial 1D Electric Field')
fprintf('Calculating propagation ... ');
E = propagation1d(lambda, E0, s, z, x);
```

```
I = abs(E).^2;
fprintf('Complete.\n');
% plot image of intensity
figure;
imagesc(x,z,I);
colormap hot;
title('propagation1d');
xlabel('x (m)');
ylabel('z (m)');
% normalize the highest intensity for each height and plot
figure;
normalI = I;
origin = normalI(1,:) * ones(size(normalI,2),1);
for m = 1 : length(z)
   temp = normalI(m,:) * ones(size(normalI,2),1);
   normalI(m,:) = normalI(m,:) / temp * origin;
end
imagesc(x,z,normalI);
colormap hot;
title('propagation1d');
xlabel('x (m)');
ylabel('z (m)');
```

propagation1d.m

```
function E = propagation1d(lambda, E0, s, z, x)
% PROPAGATION1D
% calculates the 2D intensity distribution with Kirchhoff's Diffraction theorem
% Input:
% lambda(double): wavelength (m)
% E0 (double[]): initalize source wave electric field distribution
% s (double[]): source area, size(s) == size(E0)
% z (double[]): height from the surface
% x (double[]): detection area
   % reshape input parameters, set them as row arrays
   E0 = reshape(E0, 1, length(E0));
   s = reshape(s, 1, length(s));
   z = reshape(z, 1, length(z));
   x = reshape(x, 1, length(x));
   % useful parameters
   k = 2 * pi / lambda;
   ds = s(2) - s(1);
   % calculation
   E = zeros(length(z),length(x));
   for m = 1 : length(z)   % for each height
```

```
        Mx = x' * ones(1,length(s));
        Ms = ones(length(x),1) * s;
        Mdist = sqrt((Mx - Ms).^2 + z(m)^2);
        % Ep = (z(m)/1i/lambda) * exp(1i*k*Mdist) ./ (Mdist.^2) * E0' * ds;
        Ep = (1i/2/lambda) * (exp(1i*k*Mdist) .* (1 - cos(Mdist./z(m))) ./ Mdist) * E0' * ds;
        E(m,:) = Ep';
    end
end
```

Optical Trapping Force Computation

The force optical tweezers on cells are computed with the Matlab toolbox downloaded from the home page of Timo A. Nieminen, PhD at Department of Physics, University of Queensland. The following main program should be placed with all the other supporting functions in the toolbox, and it will generate a 1D plot of computational trapping force.

example_my_gaussian.m

```
% Calculation of force in a Gaussian beam trap
% Change from the template "example_gaussian.m"
% PACKAGE INFO
clear;clc;clf;close all;

%% Computation Force
% Specify refractive indices
n_medium = 1.33;
n_particle = 1.37;
n_relative = n_particle/n_medium;

% If you want to give all measurements in wavelengths in the surrounding
% medium, then:
wavelength = 1.064;
% wavelength = wavelength0 / n_medium;
% else you can give it in any units you want. Only k times lengths matters
k = 2*pi/wavelength;

% START COMPUTATION
tic
radius = 5.5;
Nmax = ka2nmax(k*radius);
diam_microns = radius * 1.064 * 2 / n_medium;
```

```
% Specify the beam width. We can either start with the numerical
% aperture (NA) or the beam convergence angle. Either way, we convert
% to the equivalent paraxial beam waist, which is the w0 we put into the
% paraxial beam to obtain the desired (non-paraxial) far field.
% For a Gaussian beam: w0 = 2/(k*tan(theta))
NA = 0.55;
beam_angle = asin(NA/n_medium)*180/pi;
w0 = 1.5;

% Polarisation. [ 1 0 ] is plane-polarised along the x-axis, [ 0 1 ] is
% y-polarised, and [ 1 -i ] and [ 1 i ] are circularly polarised.
polarisation = [ 1 0 ];

% Location of the focal point relative to the particle. These are the
% [ x y z ] coordinates.
beam_offset = [ 0 0 0];

[n,m,a0,b0] = bsc_pointmatch_farfield(Nmax,1,[ 0 0 w0 1 polarisation 90 beam_offset ]);
[a,b,n,m] = make_beam_vector(a0,b0,n,m);

% Insert tmatrix here %
T = tmatrix_mie(Nmax,k,k*n_relative,radius);
% Force Calculation

z = linspace(-4,4,80);
r = linspace(-3-radius,0,80);

fz = zeros(size(z));
fr = zeros(size(r));

%root power for nomalization to a and b individually.
pwr = sqrt(sum( abs(a).^2 + abs(b).^2 ));

%normalize total momentum of wave sum to 1. Not good for SI EM field.
a=a/pwr;
b=b/pwr;

%calculate the force along z
for nz = 1:length(z)

   [A,B] = translate_z(Nmax,z(nz));
   a2 = ( A*a + B*b );
   b2 = ( A*b + B*a );

   pq = T * [ a2; b2 ];
   p = pq(1:length(pq)/2);
```

```
    q = pq(length(pq)/2+1:end);

    fz(nz) = force_z(n,m,a2,b2,p,q);

end

zeroindex=find(fz<0,1);

if length(zeroindex)~=0
    %fit to third order polynomial the local points. (only works when dz
    %sufficiently small)
    pz=polyfit(z(max([zeroindex-2,1]):min([zeroindex+2,length(z)])),fz(max([zeroindex-
2,1]):min([zeroindex+2,length(z)])),2);
    root_z=roots(pz); %find roots of 3rd order poly.
    dpz=[3*pz(1),2*pz(2),1*pz(3)]; %derivative of 3rd order poly.

    real_z=root_z(imag(root_z)==0); % finds real roots only.

    rootsofsign=polyval(dpz,real_z); %roots that are stable
    zeq=real_z(rootsofsign<0); %there is at most 1 stable root. critical roots give error.
    try
        zeq=zeq(abs(zeq-z(zeroindex))==min(abs(zeq-z(zeroindex))));
    end
else
    zeq=[];
end

if length(zeq)==0
    warning('No axial equilibrium in range!')
    zeq=0;
end

% equilibrium probably only correct to 1 part in 1000.
%now work out spherical coordinates along that axis:
[rt,theta,phi]=xyz2rtp(r,0,zeq);

%calculate the x-axis coefficients for force calculation.
Rx = z_rotation_matrix(pi/2,0);
Dx = wigner_rotation_matrix(Nmax,Rx);

for nr = 1:length(r)

    R = z_rotation_matrix(theta(nr),phi(nr)); %calculates an appropriate axis rotation off z.
    D = wigner_rotation_matrix(Nmax,R);

    [A,B] = translate_z(Nmax,rt(nr));
```

```
   a2 = D'*(  A * D*a +  B * D*b ); % Wigner matricies here are hermitian. Therefore in
MATLAB the D' operator is the inverse of D.
   b2 = D'*(  A * D*b +  B * D*a ); % In MATLAB operations on vectors are done first,
therefore less calculation is done on the matricies.

   pq = T * [ a2; b2 ];
   p = pq(1:length(pq)/2);
   q = pq(length(pq)/2+1:end);

   fr(nr) = force_z(n,m,Dx*a2,Dx*b2,Dx*p,Dx*q); %Dx makes the z-force calculation
the x-force calculation.

end
%     timetakes(ii)=toc;
% end
%
% plot(log([4:length(timetakes)])/log(10),log(timetakes(4:end)-timetakes(3:end-
1))/log(10))
% plot([1:length(timetakes)-1],timetakes(2:end)-timetakes(1:end-1))

% final useful results: r and fr
r = r + radius;

toc
% END COMPUTATION

% Plot Figure
figure;
plot(r, fr, 'r');
title('Trapping Force');
xlabel('Distance (um)');
ylabel('Force');
```

VITA

Peifeng Jing was born and grew up in Taiyuan, Shanxi Province in the north of China. He attended Zhejiang University in Hangzhou, China, where he received his bachelor degree at Department of Optical Engineering in 2012. He moved to Seattle and started his Ph.D. study in the Electrical Engineering program at the University of Washington.